

Determination and application of 3-D wavefront attributes

Dissertation
zur Erlangung des Doktorgrades
an der Fakultät für
Mathematik, Informatik und Naturwissenschaften
im Fachbereich Geowissenschaften
der Universität Hamburg

vorgelegt von
Yujiang Xie

Hamburg, 2017

Tag der Disputation: 07. Dec. 2017

Folgende Gutachter empfehlen die Annahme der Dissertation:

Prof. Dr. Dirk Gajewski

PD Dr. Claudia Vanelle

Abstract

Wavefront attributes are crucial in studying high-frequency seismic body waves propagating in complex 3-D inhomogeneous isotropic and anisotropic media. In practice, the wavefront attributes involve many useful applications in seismology and seismic exploration, such as pre-stack data enhancement, diffraction separation, and wavefront tomography. Conventionally, the 3-D wavefront attributes are determined by the 3-D common-reflection-surface (CRS) approach with a pragmatic search strategy in order to reduce the computational costs. However, theoretically, the wavefront attributes should be determined globally since the conventional pragmatic approach searching in sub-volumes of the data that may lead to a poor or insufficient fit of the full travel-time surface to the full data volume. Besides, modern global optimization algorithms allow to determine the 3-D CRS wavefront attributes in an economically competitive fashion. For a global determination of the 3-D CRS wavefront attributes and to demonstrate one application with the globally-determined wavefront attributes, this work is mainly composed of two parts.

In the first part, I devote to work on a global determination of the 3-D CRS wavefront attributes, where several global optimization algorithms are introduced for the simultaneous search purpose, e.g., the particle swarm optimisation (PSO), the genetic algorithm (GA), as well as the differential evolution (DE) algorithm. A comparison of these global optimization algorithms with the conventional pragmatic approach is given in this part. Results with the open 3-D SEG C3WA data indicate that the global determination of the 3-D CRS wavefront attributes by the DE algorithm is the most superior one in terms of image quality and computational efficiency when compared with the PSO, GA, and the conventional pragmatic approach.

In the second part, I present one application with the globally-determined wavefront attributes, which is called wavefront-attribute-based 5-D interpolation (5-D WABI). The 5-D WABI approach is an extension of the conventional 3-D partial CRS stacking. The only differences between them are that, for the 5-D WABI method, the wavefront attributes are determined globally with the DE algorithm and an azimuth-based trace regularization is utilized within each 3-D common-midpoint (CMP) gather, while for the conventional 3-D partial CRS approach, the wavefront attributes are searched by the pragmatic approach and the trace regularization is often performed along an azimuth-fixed direction. A comparison of the

5-D WABI approach with the conventional 3-D partial CRS method indicates that the 5-D WABI has its advantages to enhance the image quality for the reduced 3-D SEG data, in particular in finite-offset volume. In order to check the potential usage of the proposed 5-D WABI method with other mathematics-based 5-D seismic interpolation, a comparison of the 5-D WABI with the rank-reduction-based 5-D interpolation is presented. Results with a simple 3-D data of a diffractor and the open 3-D SEG C3WA data show that the proposed 5-D WABI method is efficient as the rank-reduction-based interpolation and can provide a powerful alternative to other 5-D interpolation methods with improved handling of diffractions and relaxed aliasing issues. Next to the interpolation capability itself the proposed 5-D WABI process also provides a data enhancement facility.

Zusammenfassung

Wellenfrontattribute sind entscheidend in der Untersuchung von hochfrequenten seismischen Wellen, die durch komplexe, inhomogene und anisotrope 3-D Medien laufen. Die Wellenfrontattribute haben viele nützliche Anwendungen in der Seismologie und seismischen Exploration, wie pre-stack Datenverbesserung, Diffraktionsseparation und Wellenfronttomography. Üblicherweise werden die 3-D Wellenfrontattribute mittels des 3-D common-reflection-surface (CRS) operators bestimmt. Dieser nutzt eine sogenannte pragmatische Suche um die Rechenzeit zu reduzieren. Allerdings sollten die Wellenfrontattribute idealerweise simultan und global bestimmt werden, da die herkömmliche pragmatische Suche nur Teile des Datenvolumen nutzt, was zu einer schlechten oder unzureichenden Anpassung der Laufzeitfläche im vollen Datenvolumen führen kann. Außerdem erlauben moderne globale Optimierungsalgorithmen die 3-D CRS Wellenfrontattribute rechenzeitlich effizient zu bestimmen. Diese Arbeit ist in zwei Teile unterteilt, die globale Bestimmung der 3-D CRS Wellenfrontattribute und eine Anwendung der zuvor bestimmten Wellenfrontattribute.

Im ersten Teil beschäftige ich mich mit der global Bestimmung der 3-D Wellenfrontattribute. Ich stelle mehrere globale Optimierungsmethoden für die simultane Suche vor: Particle Swarm Optimisation (PSO), Genetic Algorithm (GA) und Differential Evolution (DE). Ein Vergleich der globalen Optimierungsalgorithmen mit der konventionellen pragmatischen Suche wird anhand des 3-D SEG C3WA Datensatzes dargestellt. Die Ergebnisse zeigen, dass eine globale Bestimmung der 3-D CRS Wellenfrontattribute mittels des DE Algorithmus am besten ist. Die Qualität der Abbildung ist besser und die Rechenzeit geringer im Vergleich zu PSO, GA und dem konventionellen pragmatischen Ansatz.

Im zweiten Teil zeige ich eine Anwendung der global bestimmten Wellenfrontattribute, die sich 5-D Wellenfrontattribut-basierte Interpolation (5-D WABI) nennt. Der 5-D WABI Ansatz ist eine Erweiterung der konventionellen partiellen 3-D CRS Stapelmethode. Der einzige Unterschied besteht darin, dass für die 5-D WABI Methode die Wellenfrontattribute global mittels DE bestimmt werden und eine Azimuth-basierte Regularisierung der Spuren für jeden 3-D common-midpoint (CMP) gather genutzt wird. Die konventionelle partielle 3-D CRS Stapelung nutzt CRS Wellenfrontattribute die durch den pragmatischen Ansatz bestimmt wurden und einen

Azimuth, der für die Interpolation konstant ist. Ein Vergleich der 5-D WABI Methode mit dem konventionellen partiellen 3-D CRS Ansatz anhand des 3-D SEG C3WA Datensatzes zeigt, dass 5-D WABI Vorteile bei der Verbesserung der Abbildungsqualität für den reduzierten 3-D SEG Datensatz aufweist, insbesondere im finiten-offets Volumen. Um das Potential der 5-D WABI Methode gegenüber mathematisch-basierten 5-D seismischen Interpolationsmethoden zu evaluieren, wird ein Vergleich mit der rank-reduction-basierten 5-D Interpolation vorgestellt. Ergebnisse an einem simplen 3-D Datensatz eines Diffraktors und des öffentlichen 3-D SEG C3WA Datensatzes zeigen, dass die vorgeschlagene 5-D WABI Methode ähnlich effizient wie die rank-reduction-basierte 5-D Interpolation ist und eine mächtige Alternative zu anderen 5-D Interpolationen, mit verbesserter Auflösung von Diffraktionen und weniger Aliasing, darstellt. Neben der Möglichkeit zur Interpolation bietet die vorgeschlagene 5-D WABI Methode auch Möglichkeiten zur Datenverbesserung.

Contents

1. Introduction	5
2. 3-D CRS with global optimization	9
2.1. Two-point paraxial traveltimes approximations in 3-D seismic systems	9
2.2. 3-D zero-offset CRS traveltimes operator in terms of wavefront attributes	10
2.3. Wavefront attribute search methods	12
2.3.1. Pragmatic approach	12
2.3.2. Global optimization	14
2.4. 3-D SEG C3WA data	18
2.5. Parameter setting in global optimization	22
2.6. Semblance of pragmatic approach and global optimization	26
2.7. Wavefront attributes of pragmatic approach and global optimization	31
3. 5-D interpolation with wavefront attributes	35
3.1. 5-D WABI	37
3.2. 3-D partial CRS stacking and 5-D WABI	42
3.2.1. Usage of pragmatic approach and DE	42
3.2.2. Semblance difference between pragmatic approach and DE	42
3.2.3. Two CMP gathers	43
3.2.4. Two CO sections	43
3.3. 5-D WABI and rank-reduction-based 5-D interpolation	56
3.3.1. Applications to a simple 3-D synthetic data	56
3.3.2. Applications to the open 3-D SEG C3WA data	58
4. Conclusions	69
5. Outlook	71
Appendices	73
A. Midpoint and offset apertures	75
B. Pseudocode of several optimization algorithms	77
C. Model-driven wavefront attributes	81

D. Data-driven wavefront attributes	87
E. Software developed in this work	97
F. Publications	99
G. Acknowledgments	101

List of Figures

2.1. Sketches illustrating the crossover operator in genetic algorithm and the mutation operator in differential evolution.	16
2.2. Velocity model of the open 3-D SEG data.	18
2.3. Sketches illustrating the data acquisition geometry and the inline crossline sections presented in this work.	19
2.4. Sketches illustrating the offset and midpoint apertures used in this work.	21
2.5. Shapes of the semblance function at four zero-offset samples.	23
2.6. Iteration tests for differential evolution, genetic algorithm, and particle swarm optimization.	24
2.7. Parameter setting for differential evolution.	24
2.8. Parameter setting for genetic algorithm.	25
2.9. Parameter setting for particle swarm optimization.	25
2.10. Parameter setting for particle swarm optimization.	26
2.11. Computational costs of the four methods.	27
2.12. Inline 190 of the semblance volume.	28
2.13. Crossline 300 of the semblance volume	29
2.14. Time slice 1.2 s of the semblance volume	30
2.15. Inline 190 of the M_{11} volume.	32
2.16. Crossline 300 of the M_{11} volume.	33
2.17. Time slice 1.2 s of the M_{11} volume.	34
3.1. CRS and partial CRS apertures used in this work.	39
3.2. Calculating $t_{zo,p}$ and construct 3-D partial CRS stacking operator.	40
3.3. Different azimuth-based regularization strategies.	41
3.4. Semblance and semblance difference for time slice 1.2 s of the 3-D semblance volume.	44
3.5. Semblance and semblance difference for inline 190 and crossline 300 of the 3-D semblance volume.	45
3.6. Semblance of the four ZO samples mentioned in Chapter 2	46
3.7. A 3-D CMP gather (CMP 181903) picked from the 3-D SEG data.	47
3.8. A 3-D CMP gather (CMP 182113) picked from the 3-D SEG data.	48
3.9. Inline 190 of the first 3-D CO volume.	50
3.10. Crossline 300 of the first 3-D CO volume.	51
3.11. Time slice 1.2 s of the first 3-D CO volume.	52

3.12. Inline 190 of the second 3-D CO volume.	53
3.13. Crossline 300 of the second 3-D CO volume.	54
3.14. Time slice 1.2 s of the second 3-D CO volume.	55
3.15. Computational costs of 5-D WABI method and 5-D DRRM method.	57
3.16. Inline 10 of the 3-D CO volume.	60
3.17. Crossline 100 of the 3-D CO volume.	61
3.18. Time slice 1.66 s of the 3-D CO volume.	62
3.19. Time slice 2.4 s of the 3-D CO volume.	63
3.20. 5-D interpolation results with the diffraction-only data.	64
3.21. Inline 190 of the 3-D CO volume.	65
3.22. Crossline 300 of the 3-D CO volume.	66
3.23. Time slice 1.2 s of the 3-D CO volume.	67
D.1. M_{00} wavefront attribute.	88
D.2. M_{10} wavefront attribute.	89
D.3. M_{11} wavefront attribute.	90
D.4. Azimuth wavefront attribute.	91
D.5. Dip wavefront attribute.	92
D.6. N_{00} wavefront attribute.	93
D.7. N_{10} wavefront attribute.	94
D.8. N_{11} wavefront attribute.	95

Chapter 1.

Introduction

Seismic ray theory is useful in studying high-frequency seismic body waves propagating in complex 3-D inhomogeneous isotropic or anisotropic media (see e.g., Červený, 1972; Gajewski and Pšenčík, 1987, 1990; Červený and Moser, 2007; Moser and Červený, 2007; Červený et al., 2012). With ray theory, global laws of individual elementary waves can be established independently (Červený, 2001). In actual applications to seismology and seismic exploration, paraxial ray theory plays a fundamental role to derive the well-known two-point paraxial traveltime approximations (e.g., Červený, 2001; Červený and Moser, 2007; Moser and Červený, 2007). Červený et al. (2012) state that the expressions of two-point traveltime squared in homogeneous isotropic media yield exact results, and expected that using the traveltime expressions in weakly inhomogeneous, either isotropic or weakly anisotropic, may provide highly accurate results.

For a medium composed of homogeneous or inhomogeneous isotropic layers, the two-point paraxial traveltime approximations are closely linked to the theory of seismic systems (e.g., Bortfeld, 1989; Hubral et al., 1992; Schleicher et al., 1993b). Generally, the traveltime parameters used in the two-point paraxial traveltime approximations are computed by kinematic ray tracing and dynamic ray tracing in ray-centred coordinate system or in the general Cartesian coordinate system. Alternatively, Bortfeld (1989) indicated that the traveltime parameters could be determined by properly designed traveltime measurements, where the first and second derivatives of the traveltime account for the measurements (see Schleicher et al., 1993b). Theoretically, the first and second derivatives of the traveltime are related to the traveltime parameters used in the common-reflection-surface (CRS) method (e.g., Jäger, 1999; Jäger et al., 2001; Mann, 2002) in which they are called kinematic wavefield attributes or wavefront attributes, and can be determined by a data-driven fashion using the semblance (Neidell and Taner, 1971) as an objective function. The wavefront attributes involve many useful applications in seismology and seismic exploration, such as 2-D and 3-D pre-stack data enhancement (e.g., Baykulov and Gajewski, 2009, 2010; Xie and Gajewski, 2016b; Xie, 2017), 5-D interpolation (Xie and Gajewski, 2017), CRS

case studies (e.g., [Menyoli et al., 2004](#); [Mandal et al., 2013](#); [Ahmed et al., 2015](#)), migration velocity estimation (e.g., [Mann, 2002](#); [Gelius and Tygel, 2015](#); [Coimbra et al., 2016](#)), tomographic inversion (e.g., [Duvencak, 2004](#); [Bauer et al., 2016](#)), diffraction separation and imaging (e.g., [Dell and Gajewski, 2011a,b](#); [Rad et al., 2015](#); [Schwarz and Gajewski, 2017](#)), and passive seismic source localization ([Schwarz et al., 2016](#)), just to name a few.

In 3-D seismic systems for the case of a normal incidence ray, e.g., the 3-D zero-offset CRS (see e.g., [Müller, 2003](#); [Bergler, 2004](#)), six or eight wavefront attributes need to be determined. For an efficient searching these wavefront attributes, the historical pragmatic approach (see [Mann et al., 1999](#)) was introduced into 3-D CRS by [Müller \(2003\)](#), where the six or eight wavefront attributes are determined in sequence from sub-volumes of the whole 3-D data. Then the obtained wavefront attributes are refined by a modified simulated annealing (SA) optimization algorithm. In [Bonomi et al. \(2009\)](#), a simultaneous search for the 3-D CRS traveltime parameters was proposed. In their work, a modification of the Powell-conjugate-direction (PCD) method ([Powell, 1964](#)) was applied to perform the simultaneous search. A comparison of the modified PCD method with the historical pragmatic approach was not given yet. For an effective determining the 3-D CRS wavefront attributes simultaneously, the metaheuristic-based particle swarm optimization (PSO) (e.g., [Kennedy and Eberhart, 1995](#); [Shi and Eberhart, 1998](#)) was tested by [Xie and Gajewski \(2016a\)](#). They showed that smoother wavefront attributes and a higher semblance could be obtained when compared to the initial search results of the pragmatic approach. Later on, an evolutionary-based Nelder-Mead algorithm was presented by [Xie and Gajewski \(2016c\)](#), where the wavefront attributes are globally searched by the genetic algorithm (GA) ([Holland, 1975](#)), then the Nelder-Mead method ([Nelder and Mead, 1965](#)) was applied to refine the wavefront attributes. However, based on our previous results, I found that a global search of the 3-D CRS wavefront attributes is still not satisfied when compared with the well-known pragmatic approach. Recently, one algorithm gets more interested, which is the differential evolution (DE) ([Storn and Price, 1997](#)). The DE algorithm was investigated by [Barros et al. \(2015\)](#) in the 2-D CRS case, in which the effectiveness of the DE performing in the 2-D CRS global search task was demonstrated and showed lower average computational costs when compared with the very fast simulated annealing (VFSA) ([Ingber, 1989](#)). A comparison of the simulated annealing (SA) family in the 2-D CRS case was given by [Garabito et al. \(2012\)](#), where the VFSA could be considered as the best one among the SA family.

In this work, I devote to work on a global determination of the 3-D CRS wavefront attributes, where the PSO, GA, and the DE algorithm are introduced for the simultaneous search purpose. A comparison of these global optimization algorithms themselves (e.g., using the semblance as an objective function) as well as comparing these global optimization algorithms with the conventional pragmatic approach are

given in **Chapter 2**. To show one application with the globally-determined wavefront attributes, in **Chapter 3**, I present a 5-D seismic interpolation technique, which is called wavefront-attribute-based 5-D interpolation (5-D WABI). The 5-D WABI is an extension of the conventional 3-D partial CRS approach with the improvement of the wavefront attributes as well as applies an azimuth-based regularization process in each 3-D CMP gather to better account for the potential of wide-, rich- and full-azimuth data. To check the potential usage of the proposed 5-D WABI method in actual applications, a comparison of the 5-D WABI with a rank-reduction-based 5-D seismic interpolation is given in **Chapter 3**. **Chapter 4** concludes this work and **Chapter 5** provides an outlook to future possibilities, in particular in diffraction imaging and wavefront tomography. In this work, vectors (lowercase) and matrices (uppercase) are denoted with boldface symbols in the text correspondingly. As opposed to 2-D vectors, 3-D vectors are marked with a hat. The 2×2 matrices are denoted as bold capitals, while the 4×4 matrices are characterized by bold underlined capitals. I use component notation in the work, where the uppercase (I, J, K) indices the values 1 and 2, and the lowercase (i, j, k) takes the values 1, 2 or 3.

Chapter 2.

3-D CRS with global optimization

2.1. Two-point paraxial traveltimes approximations in 3-D seismic systems

In a 3-D seismic system composed of smooth, laterally inhomogeneous isotropic layers, the wavefront attributes can be determined by the well-known paraxial ray approximations (e.g., [Bortfeld, 1989](#)), where the concept of surface-to-surface formalism is applied, and relevant shot and receiver points are situated on the anterior and posterior surface, respectively (see e.g., [Bortfeld, 1989](#); [Hubral et al., 1992](#); [Schleicher et al., 1993b](#)). With Bortfeld's theory, the paraxial ray approximation is

$$\begin{pmatrix} \mathbf{x}_g \\ \bar{\mathbf{p}}_g - \mathbf{p}_g \end{pmatrix} = \begin{pmatrix} \mathbf{A} & \mathbf{B} \\ \mathbf{C} & \mathbf{D} \end{pmatrix} \begin{pmatrix} \mathbf{x}_s \\ \bar{\mathbf{p}}_s - \mathbf{p}_s \end{pmatrix}, \quad (2.1)$$

where the four 2×2 matrices \mathbf{A} , \mathbf{B} , \mathbf{C} and \mathbf{D} are elements of the well-known 4×4 surface-to-surface propagator matrix \mathbf{T} , which relates to the second derivatives of the traveltimes. The 2-D slowness vector \mathbf{p}_s ($\bar{\mathbf{p}}_s$) involved to the first derivatives of the traveltimes, is a projection of the 3-D slowness vector $\hat{\mathbf{p}}_s$ ($\hat{\hat{\mathbf{p}}}_s$) of the reference ray onto the plane tangent to the anterior surface. Similarly, the \mathbf{p}_g ($\bar{\mathbf{p}}_g$) is situated on the plane tangent to the posterior surface. The 2-D vector \mathbf{x}_s (\mathbf{x}_g) is a projection of the displacement vector between $\hat{\mathbf{s}}$ and $\hat{\hat{\mathbf{s}}}$ ($\hat{\mathbf{g}}$ and $\hat{\hat{\mathbf{g}}}$) onto the plane tangent to the anterior (posterior) surface (see e.g., [Bortfeld, 1989](#); [Hubral et al., 1992](#); [Schleicher et al., 1993b](#)). With the Hamilton's equation ([Buchdahl, 1970](#)), the two-point paraxial traveltimes t_p , up to the quadratic terms, is expressed as:

$$t_p = t_{co} - \mathbf{p}_s \cdot \mathbf{x}_s + \mathbf{p}_g \cdot \mathbf{x}_g - \mathbf{x}_s^T \mathbf{B}^{-1} \mathbf{x}_g + \frac{1}{2} \mathbf{x}_s^T \mathbf{B}^{-1} \mathbf{A} \mathbf{x}_s + \frac{1}{2} \mathbf{x}_g^T \mathbf{D} \mathbf{B}^{-1} \mathbf{x}_g, \quad (2.2)$$

where t_{co} is the reference traveltimes between $\hat{\mathbf{s}}$ and $\hat{\mathbf{g}}$, superscript T denotes the transpose, and \mathbf{B}^{-1} is the inverse matrix of \mathbf{B} . Squaring both sides of the Equation (2.2), and retaining terms up to second order, the hyperbolic traveltimes t_{hyp} is

obtained:

$$t_{hyp}^2 = (t_{co} - \mathbf{p}_s \cdot \mathbf{x}_s + \mathbf{p}_g \cdot \mathbf{x}_g)^2 + t_{co}(\mathbf{x}_s^T \mathbf{B}^{-1} \mathbf{A} \mathbf{x}_s - 2\mathbf{x}_s^T \mathbf{B}^{-1} \mathbf{x}_g + \mathbf{x}_g^T \mathbf{D} \mathbf{B}^{-1} \mathbf{x}_g). \quad (2.3)$$

Equation (2.3) is expressed in terms of source and receiver coordinates (see e.g., Ursin, 1982; Schleicher et al., 1993b). If we consider the anterior surface coincides with the posterior surface, i.e., the sources and receivers are located on the same surface, e.g., the sea level, Equation (2.3) can be expressed in midpoint and half-offset coordinates by

$$t_{hyp}^2 = (t_{co} + \frac{\partial t}{\partial \mathbf{m}_\zeta} \cdot \mathbf{m}_\zeta + \frac{\partial t}{\partial \mathbf{h}_\zeta} \cdot \mathbf{h}_\zeta)^2 + t_{co}(\mathbf{m}_\zeta^T \mathbf{M}_{mm} \mathbf{m}_\zeta + 2\mathbf{m}_\zeta^T \mathbf{M}_{mh} \mathbf{h}_\zeta + \mathbf{h}_\zeta^T \mathbf{M}_{hh} \mathbf{h}_\zeta), \quad (2.4)$$

where $\mathbf{m}_\zeta = \frac{1}{2}(\mathbf{x}_g + \mathbf{x}_s)$, and $\mathbf{h}_\zeta = \frac{1}{2}(\mathbf{x}_g - \mathbf{x}_s)$. The three 2×2 matrices of Equation (2.4) are given by

$$\begin{aligned} \mathbf{M}_{mm} &= \mathbf{B}^{-1} \mathbf{A} + \mathbf{D} \mathbf{B}^{-1} - \mathbf{B}^{-1} - \mathbf{B}^{-T}, \\ \mathbf{M}_{mh} &= -\mathbf{B}^{-1} \mathbf{A} + \mathbf{D} \mathbf{B}^{-1} + \mathbf{B}^{-1} - \mathbf{B}^{-T}, \\ \mathbf{M}_{hh} &= \mathbf{B}^{-1} \mathbf{A} + \mathbf{D} \mathbf{B}^{-1} + \mathbf{B}^{-1} + \mathbf{B}^{-T}. \end{aligned} \quad (2.5)$$

2.2. 3-D zero-offset CRS traveltine operator in terms of wavefront attributes

In case of the reference ray coincides with the normal ray, e.g., $\hat{\mathbf{s}} = \hat{\mathbf{g}}$, we have $t_{co} = t_{zo}$, $\frac{\partial t}{\partial \mathbf{h}_\zeta} = \mathbf{0}$, and $\frac{\partial t}{\partial \mathbf{m}_\zeta} = 2\mathbf{p}_g$. Then Equation (2.4) can be simplified as

$$t_{hyp}^2 = (t_{zo} + 2\mathbf{p}_g \cdot \mathbf{m}_\zeta)^2 + 2t_{zo}(\mathbf{m}_\zeta^T \mathbf{M}_{mm}^{zo} \mathbf{m}_\zeta + \mathbf{h}^T \mathbf{M}_{hh}^{zo} \mathbf{h}), \quad (2.6)$$

where t_{zo} and \mathbf{p}_g are the zero-offset (ZO) traveltine and slowness vector of the normal emergence ray. The matrices \mathbf{M}_{mm}^{zo} , \mathbf{M}_{mh}^{zo} , and \mathbf{M}_{hh}^{zo} satisfy:

$$\begin{aligned} \mathbf{M}_{mm}^{zo} &= \mathbf{D} \mathbf{B}^{-1} - \mathbf{B}^{-1}, \\ \mathbf{M}_{mh}^{zo} &= \mathbf{Z}, \\ \mathbf{M}_{hh}^{zo} &= \mathbf{D} \mathbf{B}^{-1} + \mathbf{B}^{-1}. \end{aligned} \quad (2.7)$$

The matrix \mathbf{Z} is a 2×2 zero matrix. Alternatively, Equation (2.6) can be expressed in terms of wavefront attributes pertaining to the normal emergence ray (see e.g., Jäger, 1999; Müller, 2003; Bergler, 2004):

$$t_{hyp}^2 = [t_{zo} + \frac{2}{v_0} \begin{pmatrix} \cos \phi \sin \theta \\ \sin \phi \sin \theta \end{pmatrix} \cdot \mathbf{m}_\zeta]^2 + \frac{2t_{zo}}{v_0} \mathbf{m}_\zeta^T \mathbf{G} \mathbf{K}_N \mathbf{G}^T \mathbf{m}_\zeta + \frac{2t_{zo}}{v_0} \mathbf{h}^T \mathbf{G} \mathbf{K}_{NIP} \mathbf{G}^T \mathbf{h}, \quad (2.8)$$

where v_0 is the near-surface velocity, θ and ϕ are the two emergence angles, namely dip and azimuth of the normal emergence ray. The midpoint displacement $\mathbf{m}_\zeta = \mathbf{m} - \mathbf{m}_{zo}$, where \mathbf{m}_{zo} is the target common-midpoint (CMP) location and \mathbf{m} is a neighboring CMP location around the target CMP. Half offset is denoted by \mathbf{h} , and \mathbf{K}_N and \mathbf{K}_{NIP} are the wavefront curvature matrices of the normal (N) wave and the normal-incidence-point (NIP) wave. Finally, a transformation from ray-centered coordinates to the general Cartesian coordinates is given by the 2×2 matrix \mathbf{G} (see e.g., Jäger, 1999; Müller, 2003; Bergler, 2004). For an efficient implementation, I rewrite Equation (2.8) to

$$t_{hyp}^2 = [t_{zo} + 2\mathbf{p} \cdot \mathbf{m}_\zeta]^2 + \mathbf{m}_\zeta^T \mathbf{N} \mathbf{m}_\zeta + \mathbf{h}^T \mathbf{M} \mathbf{h}, \quad (2.9)$$

where

$$\frac{1}{v_0} \begin{pmatrix} \cos\phi \sin\theta \\ \sin\phi \sin\theta \end{pmatrix} = \mathbf{p}_g = \mathbf{p} = (p_x, p_y)^T, \quad (2.9a)$$

$$\frac{2t_{zo}}{v_0} \mathbf{G} \mathbf{K}_N \mathbf{G}^T = 2t_{zo} \mathbf{M}_{mm}^{zo} = \mathbf{N} = \begin{pmatrix} N_{00} & N_{10} \\ N_{10} & N_{11} \end{pmatrix}, \quad (2.9b)$$

$$\frac{2t_{zo}}{v_0} \mathbf{G} \mathbf{K}_{NIP} \mathbf{G}^T = 2t_{zo} \mathbf{M}_{hh}^{zo} = \mathbf{M} = \begin{pmatrix} M_{00} & M_{10} \\ M_{10} & M_{11} \end{pmatrix}, \quad (2.9c)$$

$$\mathbf{G} = \begin{pmatrix} \cos\theta \cos\phi & -\cos\theta \sin\phi \\ \sin\phi & \cos\phi \end{pmatrix}. \quad (2.9d)$$

The eight traveltime parameters: θ , ϕ , M_{00} , M_{10} , M_{11} , N_{00} , N_{10} and N_{11} , are related to the eight wavefront attributes to be determined in this work. For each zero-offset sample t_{zo} , the wavefront curvature matrices \mathbf{K}_{NIP} and \mathbf{K}_N can be gotten directly if the matrices \mathbf{M} and \mathbf{N} are available. In the following sections, I call the eight traveltime parameters as wavefront attributes that can be determined by Equation (2.9) while taking the semblance S as an objective function. The semblance function I used in this work is defined as

$$S = \frac{\sum_{j=i-w}^{i+w} \left(\sum_{k=0}^{n-1} q_{j,k} \right)^2}{n \sum_{j=i-w}^{i+w} \sum_{k=0}^{n-1} q_{j,k}^2}, \quad (2.10)$$

where the summation is performed along the attribute-steered traveltime surface (indicated by index i) cutting through the target zero-offset trace. The traveltime at this point is t_{zo} . The subscript j represents samples around i within the semblance bandwidth defined by $2w+1$, where w denotes half coherence bandwidth which usually corresponds to the prevailing wave period of the observed events. In this work, I use $w = 4$ for the 3D SEG data discussed below. The parameter $q_{j,k}$ is the amplitude of a sample j of trace k , and n accounts for the maximum number of traces

used in the semblance analysis. An example of the half semblance bandwidth w or called half coherence bandwidth is given in Figure 2.4a. The travelttime surface used to fit with the observed event is steered by the eight wavefront attributes. Hence if the maximum semblance is found during the fitting process, the corresponding wavefront attributes used in the travelttime formula are obtained. In practice, the challenge in the semblance analysis is to find the maximum value. With different search strategies or algorithms, the efficiency and accuracy may be different. A discussion related to find the maximum of the semblance will be discussed later.

Alternatively, the wavefront attributes could be computed from a smooth, laterally inhomogeneous background velocity model, where the kinematic and dynamic ray tracing systems are utilized. A relation between the 3-D CRS wavefront attribute and the slowness vector and ray propagator matrix computed by the kinematic and dynamic ray tracing is provided in the **Appendix C**. The forwarded wavefront attributes are out of my discussion in this work and I will investigate them in the future with smooth velocity model. One may note that even with the kinematic and dynamic ray tracing, the computed wavefront attributes are also an approximation to the true wavefront attributes. The paraxial ray theory might be only valid within a defined vicinity of the reference ray. With complex velocity models, I have not found any analytical solution to compute the true wavefront attributes in order to check the accuracy of the wavefront attributes provided by the 3-D CRS approach. I often use the semblance to check the accuracy of the data-driven wavefront attributes, which has been reported well in the literature.

2.3. Wavefront attribute search methods

In this section, I first simply summarize the pragmatic approach that has been reported by Müller (2003). Then I introduce three global optimization algorithms to simultaneously search the 3-D CRS wavefront attributes.

2.3.1. Pragmatic approach

The pragmatic approach represents one way to determine the 3-D CRS wavefront attributes (e.g., Müller, 2003, 2007; Dell and Gajewski, 2011a,b; Ahmed et al., 2015; Rad et al., 2015), which is composed of an initial search and a local optimization.

Initial search

The initial search of the pragmatic approach usually includes three steps:

Step 1: 3-D CMP experiment. In this step, a 3-D stacked volume together with three wavefront attributes, i.e., M_{00} , M_{10} and M_{11} , are obtained. If we assume $\mathbf{m}_\zeta = 0$, Equation (2.9) simplifies as

$$t_{hyp}^2 = t_{zo}^2 + \mathbf{h}^T \mathbf{M} \mathbf{h}. \quad (2.11)$$

The search space for each element of \mathbf{M} can be constrained by a velocity guide or limited between $4/v_{max}^2$ to $4/v_{min}^2$ if no any velocity guides are available, where v_{min} and v_{max} are the possible minimum and maximum stacking velocity estimated from the observed data. Equation (2.11) can be simplified in case of a narrow-azimuth acquisition (see Cardone et al., 2003). The 3-D stacked volume gotten here is used in the following steps.

Step 2: Angle search or slowness search. In this step, the azimuth (ϕ) and dip (θ) are determined from the 3-D stacked volume by a plane wave assumption. Its search operator is given by

$$t_{hyp} = t_{zo} + 2\mathbf{p}^T \mathbf{m}_\zeta. \quad (2.12)$$

Equation (2.12) is a special case of Equation (2.9) with $\mathbf{h} = 0$ and $\mathbf{N} = 0$. For each zero-offset time t_{zo} , an effective search space for ϕ is set between 0 to 2π if no priori azimuth acquisition is provided. Similarly, the search space for θ is set between $-\pi/2$ to $\pi/2$ if no any dip information is available.

Step 3: Normal wavefront curvature search. The search operator is

$$t_{hyp}^2 = [t_{zo} + 2\mathbf{p}^T \mathbf{m}_\zeta]^2 + \mathbf{m}_\zeta^T \mathbf{N} \mathbf{m}_\zeta. \quad (2.13)$$

Equation (2.13) is also a special case of Equation 2.9 with $\mathbf{h} = 0$. The slowness vector \mathbf{p} used in Equation (2.13) is determined from Step 2. An effective search space for each element of \mathbf{N} is constrained by each element of \mathbf{M} (see e.g., Jäger, 1999; Müller, 2003), and a negative \mathbf{N} occurs for concave reflectors. If the slowness vector \mathbf{p} and the matrix \mathbf{N} are provided, the matrix \mathbf{M} can be searched again from the entire 3-D prestack data by using Equation (2.9) with the \mathbf{p} and \mathbf{N} determined above.

Local optimization

In order to refine the wavefront attributes, a local optimization algorithm could be used, such as the simulated annealing (SA) family (see Kirkpatrick et al., 1983;

Corana et al., 1987; Ingber, 1989), or the Nelder-Mead method (Nelder and Mead, 1965). The two algorithms incorporated into the 3-D CRS approach are provided in Algorithm: 5 of **Appendix B**, which is a combination of the SA algorithm with the Nelder-Mead method. The pseudocode of the classic PCD algorithm with respect to the 3-D CRS approach is also given there (see Algorithm: 6 of **Appendix B**). I take the classic PCD as a local optimization tool here because I have not found an effective global search strategy by the classic PCD algorithm in the 3-D CRS case, i.e., a valid search space in each conjugate direction is not found. Without a valid search space, the minimum of the objective function (i.e., the negative maximum semblance) in each direction may come from an infinity where there is no any physical meaning for each of the wavefront attributes. Introducing more local optimization algorithms are out of my discussion since a local optimization may fail if the initial search values are located far away from the global best.

2.3.2. Global optimization

In this section, three global optimization algorithms are introduced for the global determination of the 3-D CRS wavefront attributes.

Particle swarm optimization

The particle swarm optimization (PSO) is originally attributed to Kennedy and Eberhart (1995) and Shi and Eberhart (1998). In each iteration, I use the PSO to generate new sets of wavefront attributes, then the semblance is computed for the newly-generated wavefront attributes until the set of wavefront attributes with the highest semblance is found. The maximum number of iterations is specified by the user and may require some tests. Various forms of PSO are documented in the literature. The one used is

$$v_{i,j}^{(k+1)} = \omega v_{i,j}^{(k)} + c_1 r_1^{(k)} (p_{i,j}^{(k)} - x_{i,j}^{(k)}) + c_2 r_2^{(k)} (g_j^{(k)} - x_{i,j}^{(k)}), \quad (2.14)$$

$$x_{i,j}^{(k+1)} = x_{i,j}^{(k)} + v_{i,j}^{(k+1)}. \quad (2.15)$$

where $v_{i,j}$ denotes position variation for each particle in the search space. Subscript i is the particle's index and j is the dimensionality of a particle. The superscript k indicates the iteration number. The coefficient ω is an inertia weight often set to 1 in the classic PSO. The parameter $p_{i,j}$ represents the previous best position of each particle, and $x_{i,j}$ denotes each particle's position. The global best position among all particles is given by g_j . The coefficients c_1 and c_2 are two positive constants set to 2 according to previous studies (see Kennedy and Eberhart, 1995; Shi and Eberhart,

1998). The parameters r_1 and r_2 are two random values generated between $[0,1]$ in each iteration. The position variation vector $v_{i,j}$ and the position vector $x_{i,j}$ of each particle itself are constrained in the user-defined search space during each iteration. The search space for each component of $x_{i,j}$ and $v_{i,j}$ is the same for each attribute. When incorporating the PSO into the 3-D CRS approach, each particle represents a set of wavefront attributes and the dimensionality j satisfies: $j=1,2,3,\dots,8$, e.g., for the full azimuth case. Next to the classical PSO algorithm with constant values for ω , c_1 and c_2 , alternative ω , c_1 and c_2 may require to be estimated from the data, which will be discussed later. The pseudo-codes of the PSO algorithm used in the 3-D CRS approach is given in Algorithm: 1 of **Appendix B**.

Genetic algorithm

The genetic algorithm (GA) is an adaptive, heuristic-based search method based on the evolutionary ideas of natural selection (Holland, 1975). I do not repeat the GA here but states how the GA is connected with the 3-D CRS approach to simultaneously search the 3-D CRS wavefront attributes. Similarly to the PSO algorithm, I use GA to generate new sets of wavefront attributes. Then the set of wavefront attributes with the maximum semblance is outputted. The GA is steered by three operators including selection, crossover, and mutation. They are combined to produce new individuals. Each set of wavefront attributes (e.g., the eight wavefront attributes) represents one individual, and each one of the eight wavefront attributes denotes one gene of an individual. The crossover operator used in this work is

$$X_{i,j} = \begin{cases} P_{i,j} & 0 \leq j < l, \\ P_{i+1,j} & l \leq j < 8, \end{cases} \quad (2.16)$$

where $X_{i,j}$ represents newly-generated individual computed from two neighbouring individuals $P_{i,j}$ and $P_{i+1,j}$ (see Figure 2.1), where $i = 1, 2, \dots, NP - 1$, and NP is the population size. In each generation or iteration, the global best individual (e.g., with the highest semblance) is stored by the last individual ($X_{NP-1,j}$). The parameter l is a random integer generated between $[0, 8]$, and j is the gene index in one individual. In the 3-D CRS approach with a wide-azimuth acquisition, each individual comprises eight genes (i.e., $j = 1, 2, \dots, 8$), which is called dimensionality. The mutation is done by arbitrary updating parts of genes in the individual $X_{i,j}$ within a predefined search space. The search space for each gene of an individual is the same for each attribute. Next generation is selected from the newly-generated individuals $X_{i,j}$ by the roulette wheel selection (see Algorithm: 3 of **Appendix B**).

In the first iteration, the used individuals are selected from the initial individuals that are randomly set in the search space. The roulette wheel selection is often done before the crossover and mutation. In each generation or iteration, the semblance

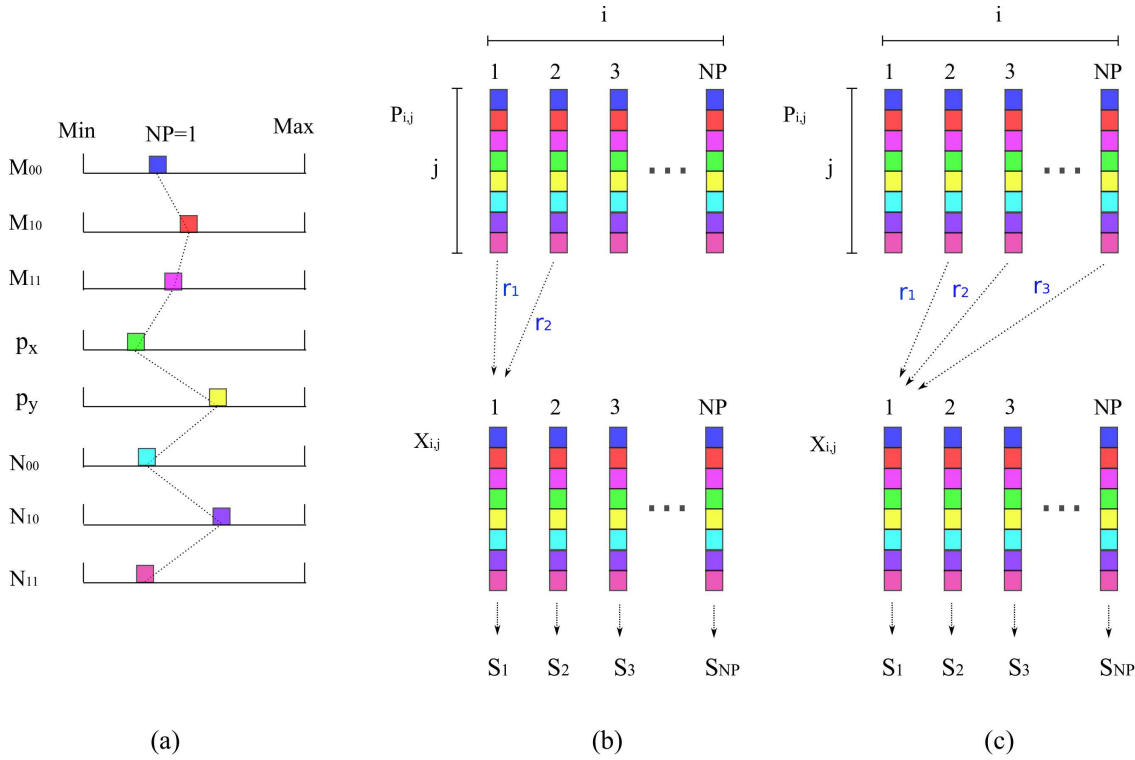


Figure 2.1.: Sketches illustrating the crossover operator in genetic algorithm (GA) and the mutation operator in differential evolution (DE). (a) Randomly generating an initial set of wavefront attributes in the search space. For the sake of simplicity, I only show one individual (agent), i.e., $NP = 1$. (b) Crossover operator used in GA, where two neighboring individuals are picked to produce a new individual, and the fitness (S_i) of each new individual is computed by the semblance. (c) The mutation operator used in DE, where three distinct agents (also distinct from the considered agent) are randomly picked to produce the new agents.

S_i of each individual is computed. Based on the tests on the 3-D SEG data, I found that 50 iterations may be required to find a maximum semblance for the 3-D CRS approach. The semblance function start to converge while the number of iterations reaches to 50. The implementation steps of the GA algorithm incorporated into the 3-D CRS approach is given in Algorithm: 2 of **Appendix B**, where the maximum iteration IT and the population size NP are tested from data. The crossover probability p_c and mutation probability p_m are set between $[0\ 1]$. Both need to be tested from the data. The parameter setting for the GA with the semblance will be discussed later.

Differential evolution

Differential evolution (DE) is originally due to [Storn and Price \(1997\)](#), where the agents are produced by three random agents picked from the generation (see [Figure 2.1](#)). The picked agents must be distinct from each other as well as distinct from the considered agent. When connected the DE with the 3-D CRS approach, each agent represents a set of wavefront attributes. The agent is similar to the individual in the GA. In the DE algorithm, the mutation operator I used is given by

$$X_{i,j} = P_{r1,j} + F(P_{r2,j} - P_{r3,j}), \quad (2.17)$$

where $r1$, $r2$ and $r3$ are the three numbers picked randomly between $[0\ NP]$. The differential weight F is generally set between $[0\ 2]$ (see [Storn and Price, 1997](#)). The DE pseudocode with respect to the 3-D CRS approach is given in Algorithm: 4 of **Appendix B**, where the crossover operator and the selection operator are given there. The parameter CR is the crossover probability, generally set between $[0\ 1]$ (see [Storn and Price, 1997](#)). [Pedersen \(2010\)](#) gave a list of good choices of DE parameters for various optimization problems, but we may note that the parameters suggested from different objective functions may be slightly different. The parameter setting for the DE algorithm with the semblance will be discussed later.

One should note that the maximum semblance discussed here is not the absolute global semblance. It is an assumed maximum semblance during the calculation with wavefront attributes generated by the global optimization algorithms. In principle, it is impossible to try all possible sets of wavefront attributes to find the absolute global semblance. The wavefront attributes produced by, e.g., the GA or DE algorithm, could be already enough to find a maximum semblance that may be close to the absolute global semblance. I will investigate this further. With complex velocity models, I have not found any analytic solutions to compute the absolute global semblance or its associated true wavefront attributes. An alternative numerical solution to compute the wavefront attributes is the well-known kinematic and dynamic ray tracing, but ray tracing also only represents one way to approximately compute the

wavefront attributes from the velocity model based on the paraxial ray theory. A comparison of two sets of approximated wavefront attributes to check whether the determined wavefront attributes accurate or not seems to make no sense.

2.4. 3-D SEG C3WA data

To test these algorithms for the determination of the 3-D CRS wavefront attributes, I use the 3-D SEG C3WA data as an example, which is an open pre-stack seismic data built by the SEG research committee (see [Aminzadeh et al., 1997](#)). The velocity model contains a tetrahedron-like salt body below a sedimentary overburden (see [Figure 2.2](#)).

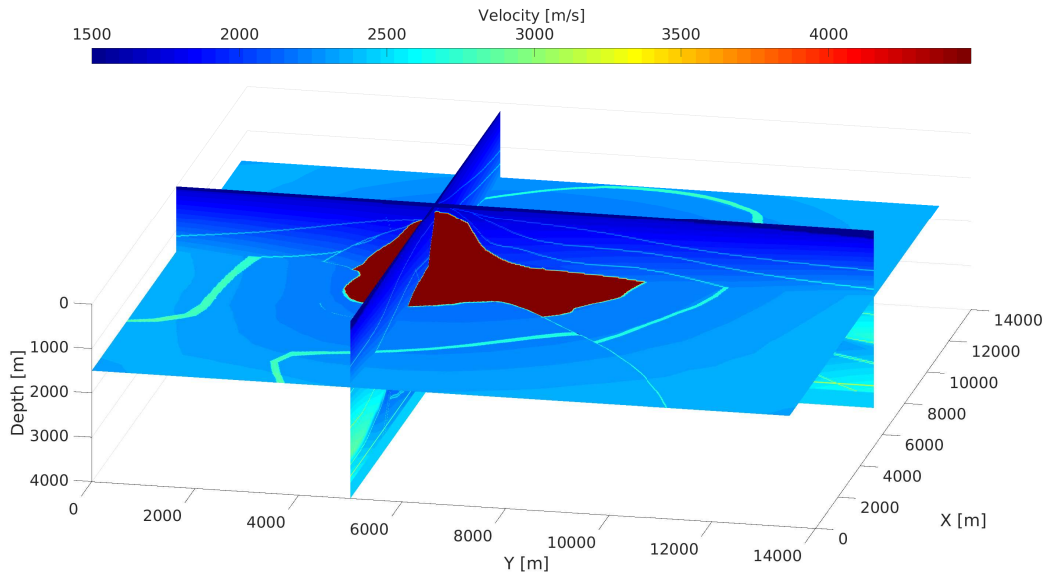


Figure 2.2.: Velocity model of the open 3-D SEG data.

Figure 2.3 (a) shows the data acquisition geometry. Its maximum CMP fold is 17, and an effective offset is ranged between 40 m to 2695 m. The midpoint distance between CMP gathers is 40 m and 20 m in x and y direction. Each trace of the data has 625 samples with a sampling interval of 8 msec. Preprocessing of the data is made accordingly, such as automatic gain control, removal of first arrivals, correct source to zero time, and bandpass filter. Finally, a random Gaussian noise with a signal-to-noise ratio (S/N) of 10 was added to the seismograms, i.e., the RMS magnitude of the signal amplitude is 10 times than the RMS magnitude of the random noise. An example of processing the open SEG/EAGE data is given by [Xu et al. \(2004\)](#). Inline and crossline configurations to be presented in this work are

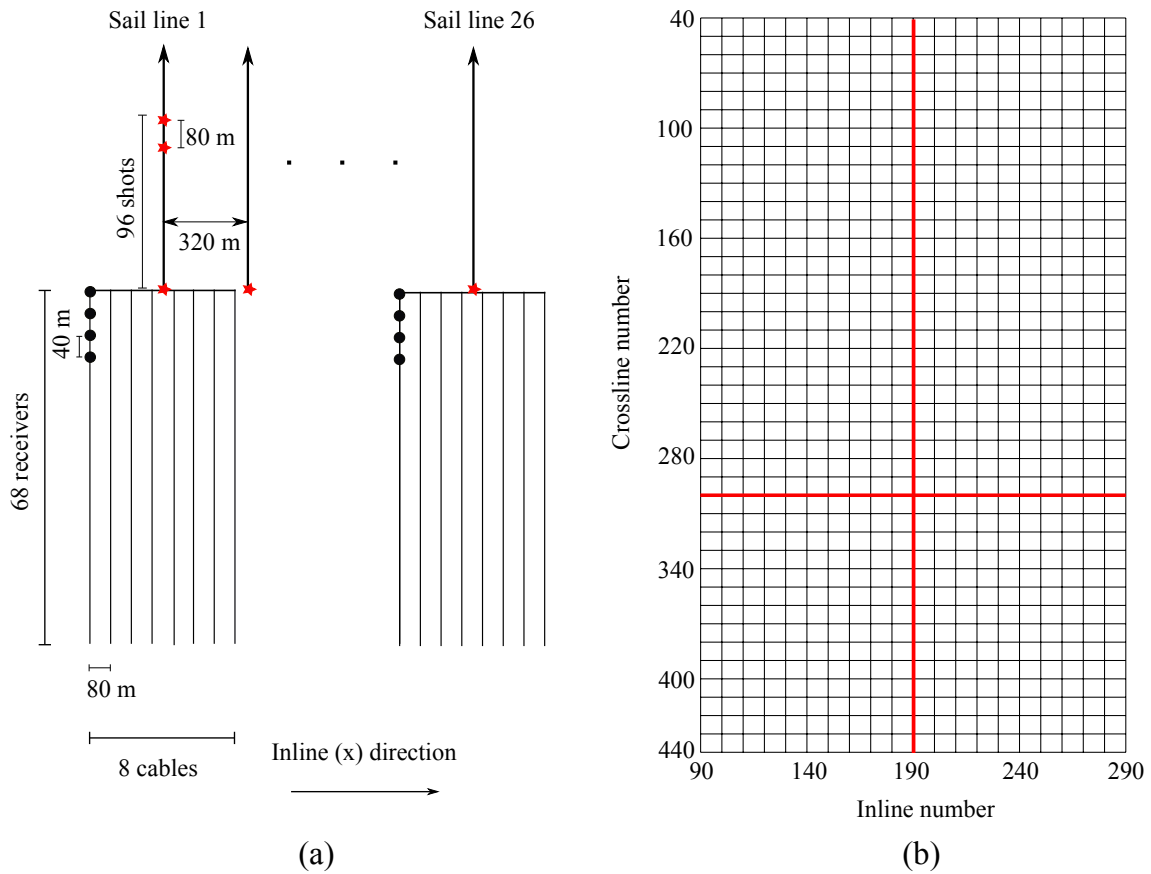


Figure 2.3.: Sketches illustrating the data acquisition geometry and the inline crossline sections presented in this work. (a) A rectangle acquisition with 8560 m width (x direction) and 10280 m long (y direction). (b) Subsets of the data with inline 93 to 285 and crossline 38 to 435 are utilized since they cover the salt body well. Two sections, inline 190 and crossline 300 (the red lines), are the target sections to be presented. For the sake of simplicity, only each tenth of them (i.e., the black lines) are shown.

illustrated in Figure 2.3 (b), where the distance between crosslines is 20 m and the distance between inlines is set to 40 m. For a better revealing the salt body in x , y , and z direction, results with inline 190, crossline 300, and a time slice of $t_{zo} = 1.2$ s are shown.

Figure 2.4 shows the offset and midpoint apertures used in this work. For an effective search at the first time, a full offset range between 40 m to 2695 m is utilized in each CMP gather (pragmatic approach) or in each CRS gather (global optimization). A full-offset search means that the half-offset \mathbf{h} given in Equation (2.9) or in Equation (2.11) is constrained between 20 m to 1347.5 m. The offset apertures are estimated from the data, for example all the observed seismic events in each CMP gather (pragmatic approach) or in each CRS gather (global optimization) would be better constrained within the full-offset apertures at the first round search. Then they are slightly adjusted in the next round search. I often use several candidates for the offset aperture until good results are achieved.

In principle, a CRS gather is comprised of several CMP gathers, depending on the midpoint apertures set by the user (see an example in Figure 2.4c). In this work, the midpoint aperture is set to 200 m in both x and y direction (see Figure 2.4c). Choosing the initial midpoint aperture mainly depends on the data. Worse results will be produced if a larger midpoint aperture is used around the considered CMP location, especially in data from a complex geological structure, e.g., with strong lateral velocity variations. After the first round search, the midpoint aperture in the next round search could be estimated by the Fresnel zone (see e.g., Hubral et al., 1993a) or tested by the user. Similar to the offset aperture estimation, I often use several candidates for the midpoint aperture until good results are achieved.

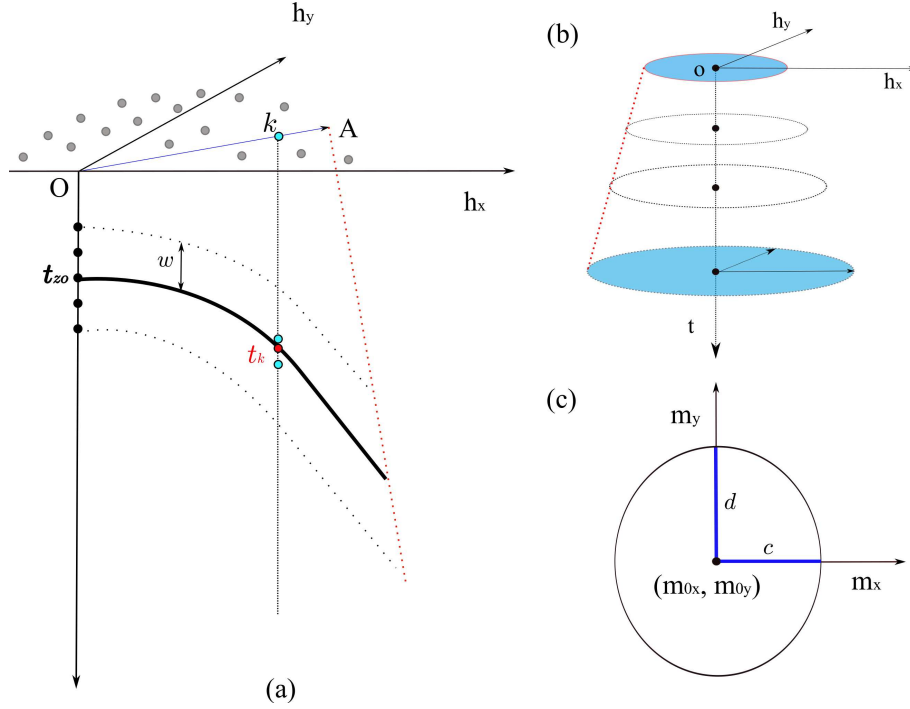


Figure 2.4.: Sketches illustrating the offset and midpoint apertures used in this work. (a) Calculating the traveltimes t_k for each trace k within a selected offset aperture. The w is the half-coherence bandwidth, which is generally evaluated by the prevailing wave period of the observed events and the sampling interval for these events or estimated by the wavelength of the observed seismograms. In this work, I use $w = 4$ for the open 3-D SEG data. The traveltime curve (bold black line) is the intersection of the traveltime surface with the vertical \overrightarrow{OA} plane passing through trace k . A linear interpolation is used in case of the calculated traveltime t_k (middle red point) does not coincide with the discrete sampling time (cyan points), i.e., the amplitude at the red point can be read to calculate the semblance. The inclined red dashed line is the aperture boundary in \overrightarrow{OA} direction that is constrained by the initial offset aperture (ellipse) shown in (b), where the semi-major and semi-minor axes of the top and bottom ellipses are predefined based on the data used. I keep the same apertures when a time sample is over (under) the top (bottom) ellipse. The vertical location of the two ellipses used for a zero-offset trace is set by the user, e.g., the observed seismic events from the top to the bottom would be better constrained within the offset aperture initially. Similar to the offset aperture, the designed midpoint aperture is given in (c), where the c and d are semi-minor and semi-major axes of an ellipse in m_x and m_y direction. In this work, the programming is executed for each CMP gather (pragmatic approach) or for each CRS gather (global optimization) one-by-one over the whole 3-D data. The m_{0x} and m_{0y} are the considered CMP location or the considered CRS location that can be calculated from the SEG data with the shot and receiver locations.

2.5. Parameter setting in global optimization

Parameter setting is crucial for a considered global optimization algorithm used in this work. For these tests, I use the 3-D SEG C3WA data. For the sake of simplicity, I pick four zero-offset samples to present, where two samples are chosen from strong seismic events and the other two samples are picked from weak events. Figure 2.5 shows the semblance function calculated by the GA, where 2000 sets of wavefront attributes are produced for each zero-offset sample. Figure 2.5 displays the non-smoothness characteristics of the semblance function, which implies that a derivative-based algorithm may fail to find the maxima of the semblance. The number of iterations IT and the population size NP used for a global optimization algorithm is estimated from the data. In my tests, I found the NP would be better greater than 40 for the 3-D SEG C3WA data. Results could be poor if one uses a less NP , e.g., $NP = 30$, and the results would be kept almost the same even the NP is increased to 50 or 80. In the work, I use $NP = 40$. The number of iteration IT is also important. Figure 2.6 shows a IT test, where I suggest to set $IT \geq 50$, and use $IT = 50$ in this work. Figure 2.7 shows the parameter testing for the DE algorithm, which shows that the maximum semblance calculated by the DE algorithm can be obtained if $F \geq 1$. I suggest to set $1 \leq F < 2$, and use $F = 1.2$ in this work. The CR is not so sensitive to the semblance, and I set it to 0.9. The choice of p_c and p_m in the GA should be careful since using a large p_m may fail to get the maximum semblance (see Figure 2.8). Considering a higher p_c may have more chance to produce new individuals, I suggest to set $0.5 \leq p_c < 1$. The mutant possibility p_m should be less than 0.4 based on this test. In this work, I set $p_c = 0.8$ and $p_m = 0.2$. The PSO parameters, w , $C1$ and $C2$, are not so sensitive to the semblance as compared to the GA, but there are still some local minima (black areas) mixed with the maximum (gray areas) (see Figure 2.9 and Figure 2.10), which indicates that choosing the PSO parameters from the black areas will fail to get the maximum semblance. Based on these tests, I suggest to set $0.6 \leq w < 1.4$, $2 \leq C1 < 3$, and $1 \leq C2 < 3$ for the 3-D SEG data. Theoretically, using a wider range of w can be considered, but for most zero-offset samples, setting the w between 0.6 to 1.4 may be already enough for the PSO algorithm for the 3-D SEG data. In this work, I use $w = 1$, $C1 = C2 = 2$, the same as previous works (see e.g., Kennedy and Eberhart, 1995; Shi and Eberhart, 1998). Only two zero-offset samples are shown here for the PSO parameter setting since the parameters suggested from the other two zero-offset samples are almost the same. Based on my tests not only the discussion above, I found that the DE could be the most stable algorithm when compared with the GA or the PSO in case of using the semblance as the objective function.

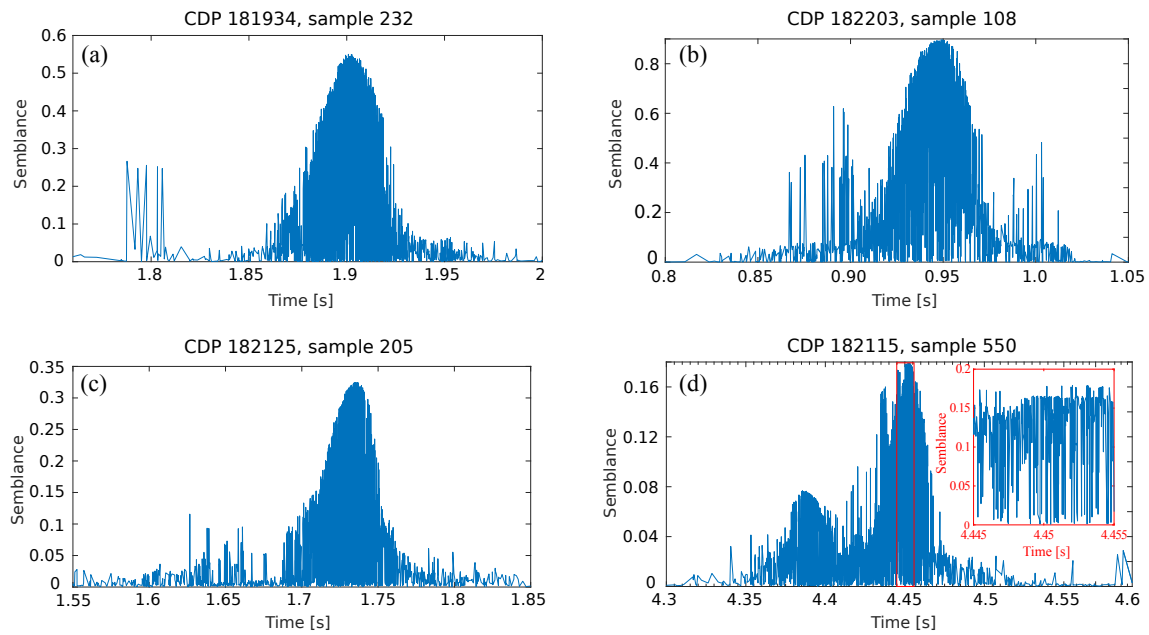


Figure 2.5.: Shapes of the semblance function at four zero-offset samples. In this figure, I use genetic algorithm (GA) to generate 2000 sets of wavefront attributes to compute the semblance, i.e., 2000 different traveltimes are calculated by the 2000 sets of wavefront attributes, and each traveltime corresponds to a semblance. In the GA, I set $IT = 50$, $NP = 40$, $p_c = 0.8$ and $p_m = 0.2$. A close-up look is given in (d) to explore the detailed shape of the semblance function. The CDP is the common data point used in the SU format data.

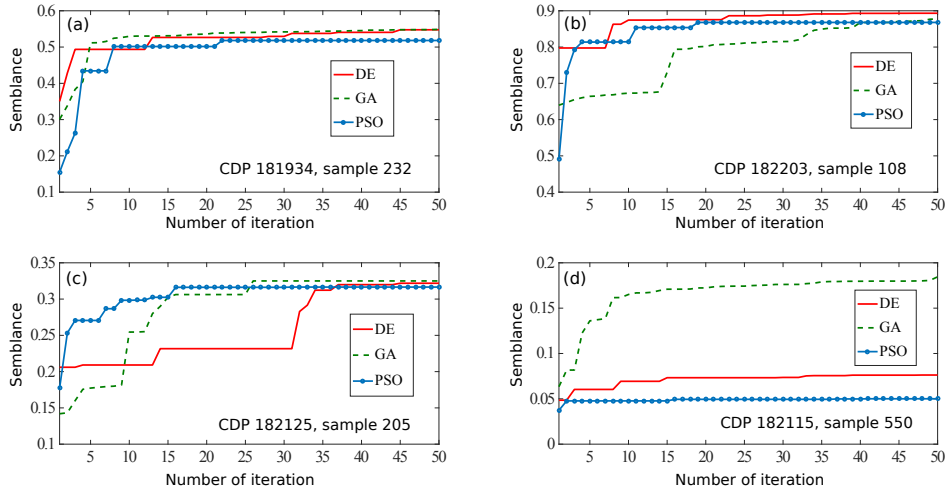


Figure 2.6.: Iteration tests for differential evolution (DE), genetic algorithm (GA), and particle swarm optimization (PSO). In these tests, I set $NP = 40$, other parameters except the IT are obtained from the parameter setting discussed below.

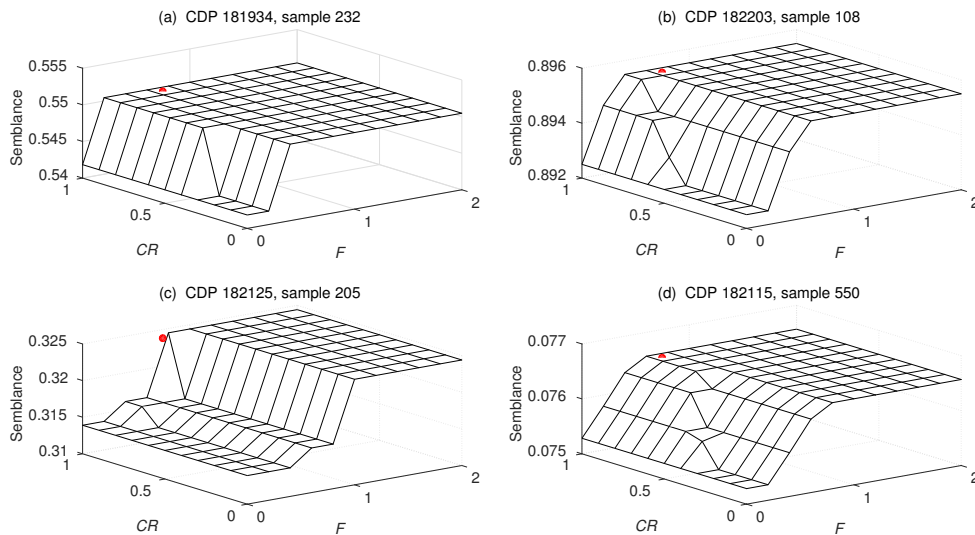


Figure 2.7.: Parameter setting for differential evolution (DE). The red points shown in the Figure are the parameters referenced by [Pedersen \(2010\)](#).

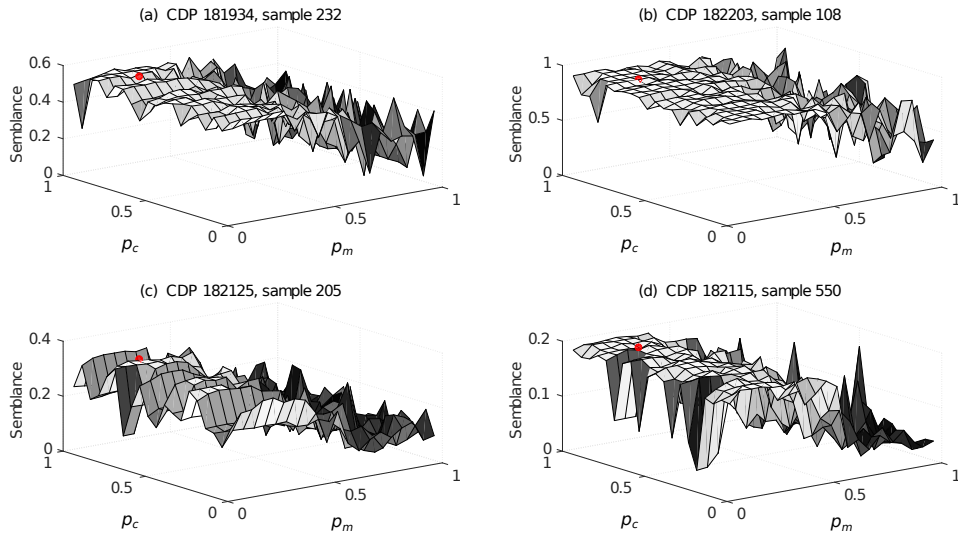


Figure 2.8.: Parameter setting for genetic algorithm (GA). The red points are the parameters suggested in this work, where I set $p_c = 0.8$ and $p_m = 0.2$.

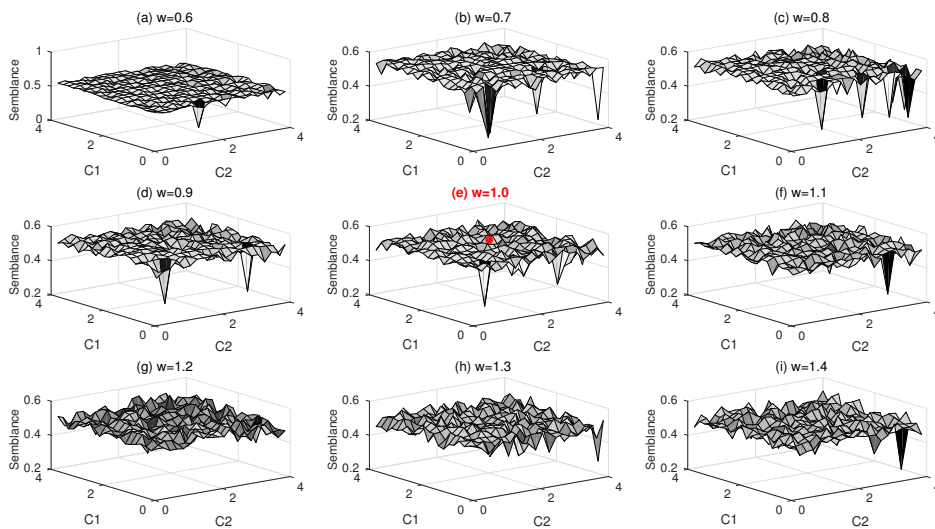


Figure 2.9.: Parameter setting for particle swarm optimization (PSO) at CDP 181934 and sample 232 of the 3-D SEG C3WA data. The red point denotes the parameters suggested in this work, where I set $w = 1$ and $C1 = C2 = 2$.

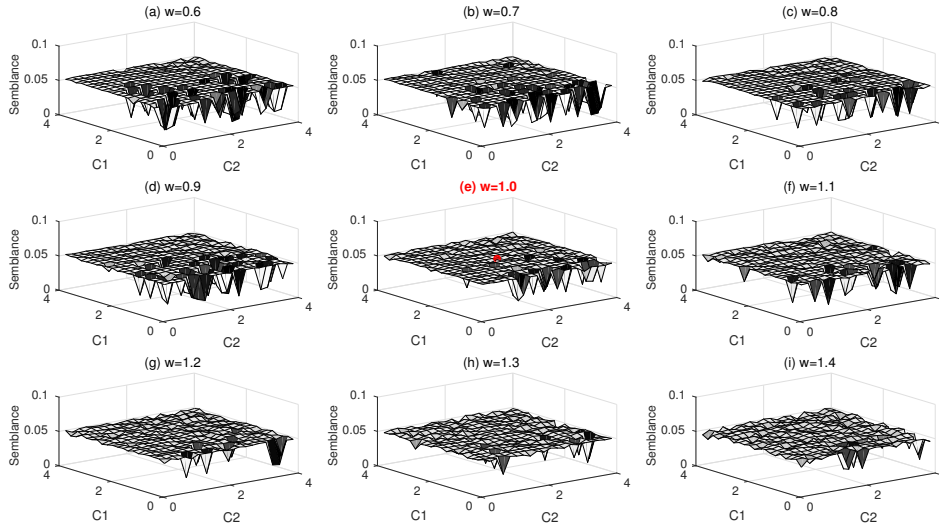


Figure 2.10.: Parameter setting for particle swarm optimization (PSO) at CDP 182115 and sample 550 of the 3-D SEG C3WA data. The red point denotes the parameters suggested in this work, where I set $w = 1$ and $C1 = C2 = 2$.

2.6. Semblance of pragmatic approach and global optimization

For a complete determination of the eight wavefront attributes from the 3-D SEG C3WA data, I found that the GA or DE algorithm is cheaper than the traditional pragmatic approach, and also cheaper than the PSO algorithm (see Figure 2.11). In the comparison, all global algorithms are tested under the same computational setting, such as the same CPUs, the same search apertures, the same population size NP , and the same number of iteration IT . The number of CPUs and the search apertures used in the pragmatic approach are set as the same as the global optimization. In the pragmatic approach, I set 100 search intervals for each element of \mathbf{M} , 80 intervals for the dip angle, 40 intervals for the azimuth angle, and 30 intervals for each element of \mathbf{N} . The search intervals used in the pragmatic approach are tested from the data. Alternative search intervals require to be tested for different datasets.

Figure 2.12 shows inline 190 of the semblance volume, which demonstrates that both the GA and DE algorithm can provide higher semblance when compared with the PSO and the pragmatic approach, especially under the salt body where the semblance provided by the GA or DE is significantly improved (see the white arrows). The PSO algorithm, sometimes, may not be stable when constant parameters (i.e.,

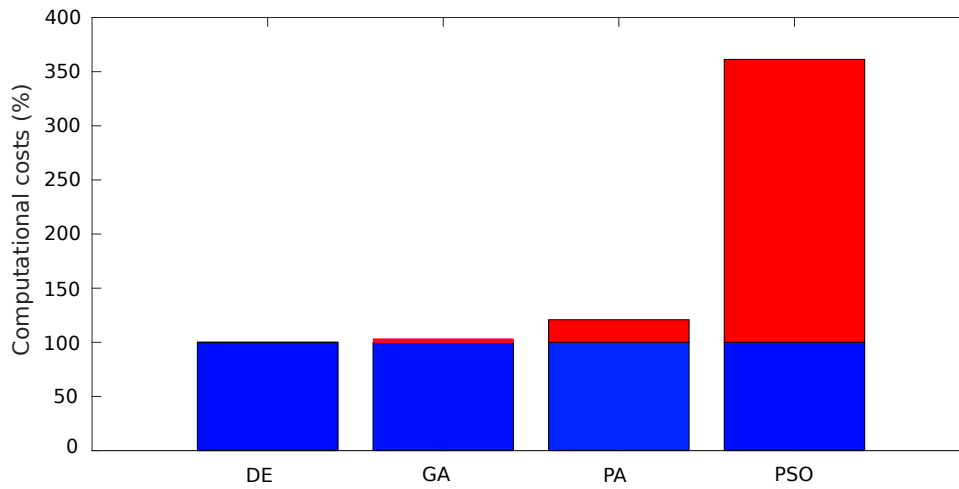


Figure 2.11.: Computational costs of the four methods. (a) differential evolution (DE) referenced as 100%, (b) genetic algorithm (GA), (c) pragmatic approach (PA), (d) particle swarm optimization (PSO).

$w = 1$, $C1 = 2$ and $C2 = 2$) are used for all zero-offset samples. A strong semblance event is disappeared in the PSO section (See Figure 2.12 b).

Figure 2.13 demonstrates crossline 300 of the semblance volume, which indicates that a higher semblance can be obtained by the global search when compared to the semblance provided by the pragmatic approach. The time slice $t_{zo} = 1.2$ s of the semblance volume is shown in Figure 2.14, where the DE demonstrates a great potential to attenuate the horizontal artifacts/footprints observed in the pragmatic approach. These horizontal artifacts are caused by the data acquisition system used.

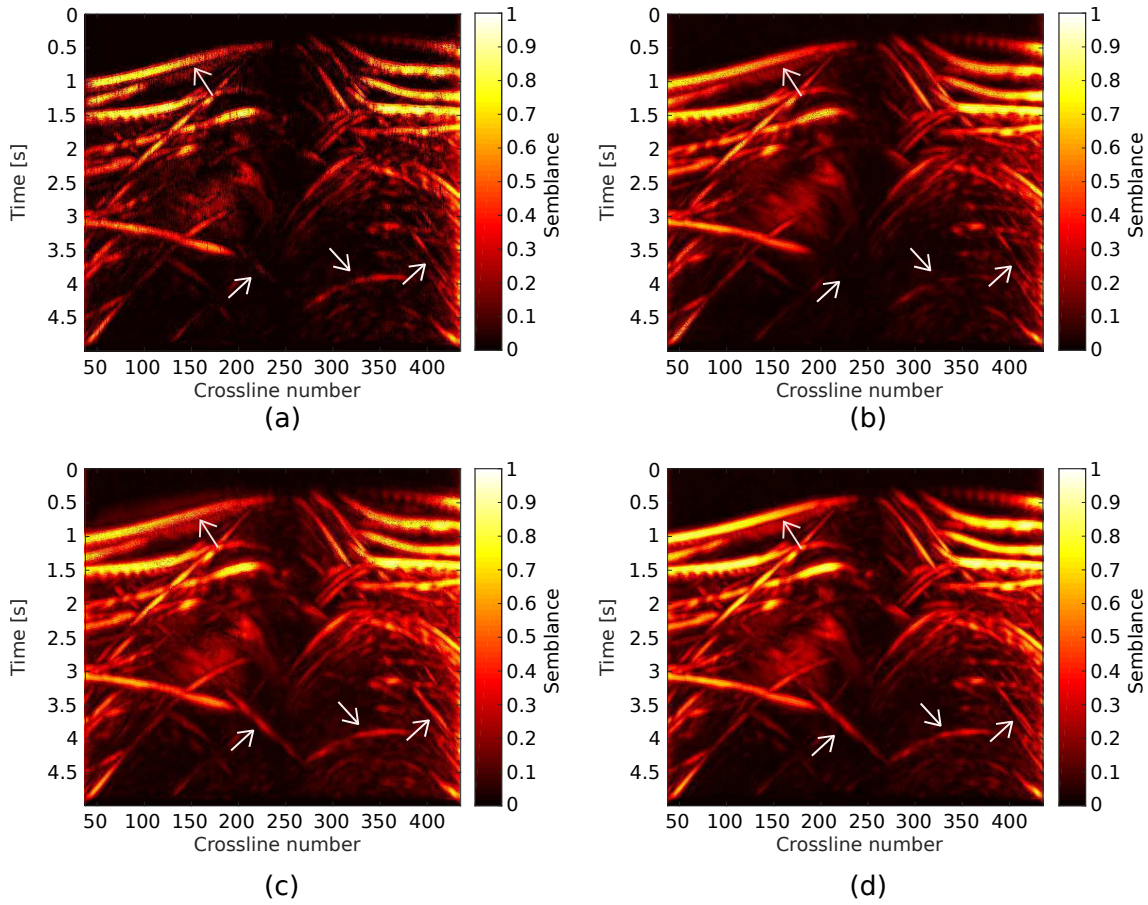


Figure 2.12.: Inline 190 of the semblance volume obtained by (a) pragmatic approach, (b) particle swarm optimization (PSO), (c) genetic algorithm (GA), and (d) differential evolution (DE). The main differences are denoted by white arrows.

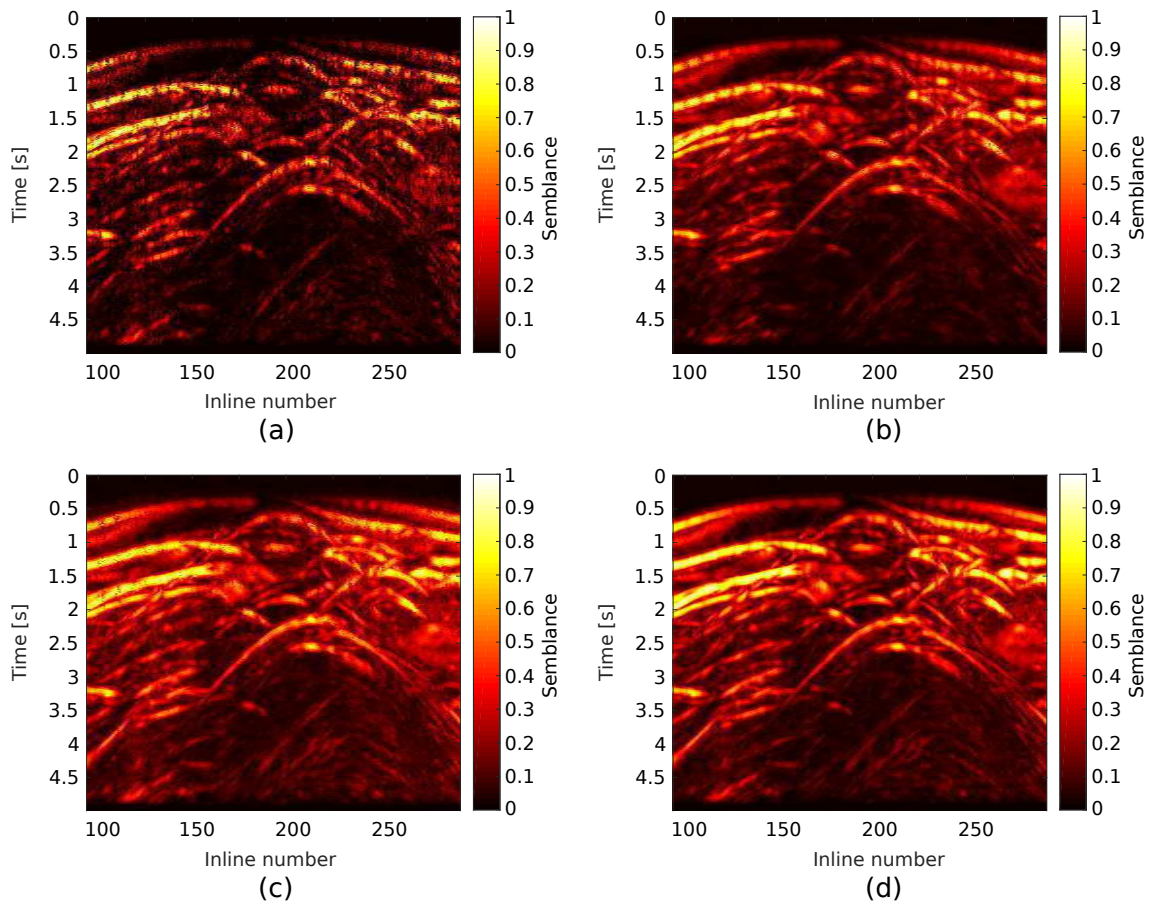


Figure 2.13.: Crossline 300 of the semblance volume obtained by (a) pragmatic approach, (b) particle swarm optimization (PSO), (c) genetic algorithm (GA), and (d) differential evolution (DE).

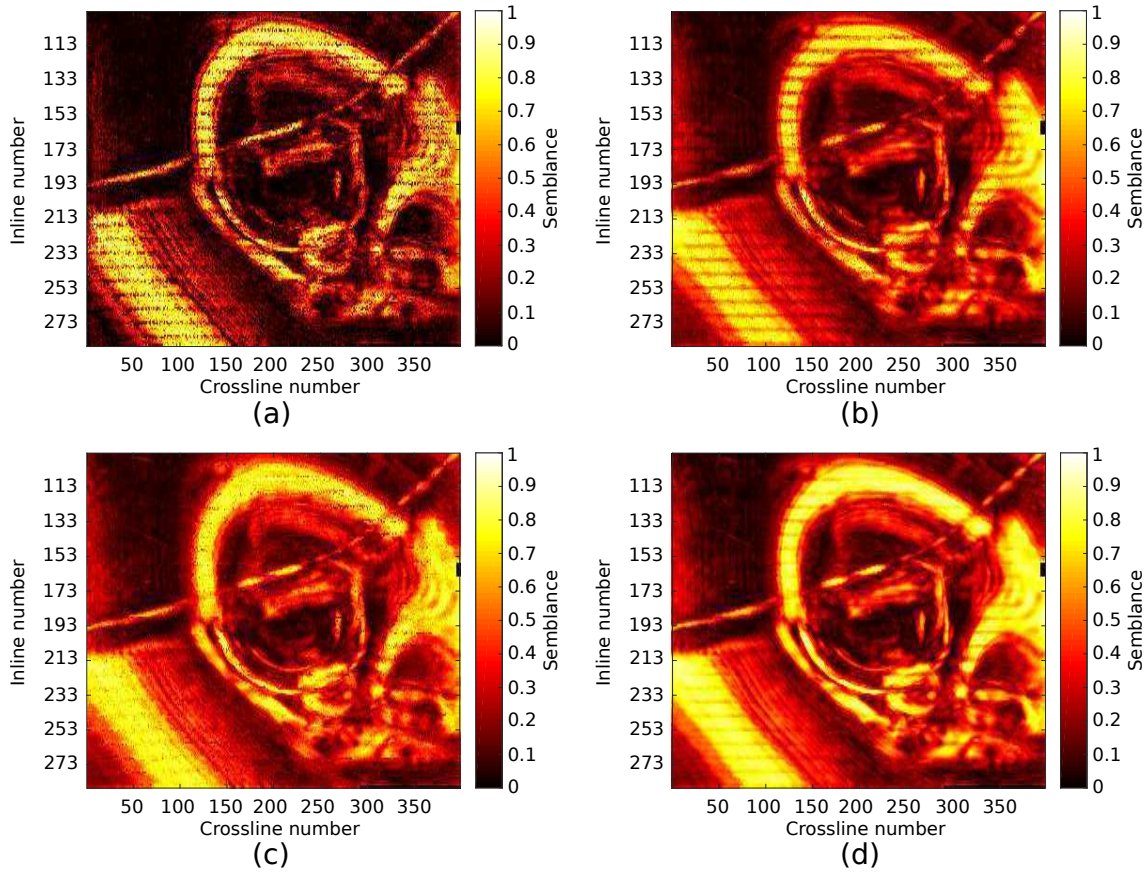


Figure 2.14.: Time slice 1.2 s of the semblance volume obtained by (a) pragmatic approach, (b) particle swarm optimization (PSO), (c) genetic algorithm (GA), and (d) differential evolution (DE). For approximate 90% zero-offset samples, the DE can provide a higher semblance than the pragmatic approach.

2.7. Wavefront attributes of pragmatic approach and global optimization

A higher semblance usually means that the simulated traveltime surface is fitted well with the observed event, and its associated wavefront attributes are accurate than those wavefront attributes searched from a lower semblance. For the sake of simplicity, only the M_{11} is shown. Other wavefront attributes are provided in **Appendix D**. Figure 2.15 and Figure 2.16 show inline 190 and crossline 300 sections of the M_{11} volume, where the M_{11} is smoother with less noise if the global search is applied. In the time slice shown in Figure 2.17, the M_{11} provided by different algorithms are different (see different colors). The color difference provided by these methods will be smaller if we clip these pictures with exactly the same color bar. In practice, the set of wavefront attributes with the best semblance is applied.

From the above investigations, I found that the DE could be the best algorithm among PSO, GA, as well as the pragmatic approach to determine the 3-D CRS wavefront attributes while using the semblance as the objective function. In **Chapter 3**, I will use the DE to represent the global optimization algorithm against with the conventional pragmatic approach to determine the 3-D CRS wavefront attributes. With the determined wavefront attributes, I will present one 5-D seismic interpolation technique called 5-D WABI, where I will state how the 5-D WABI works. To check the potential usage of the proposed 5-D WABI method, a comparison of the 5-D WABI with a mathematics-based, rank-reduction 5-D seismic interpolation is given there.

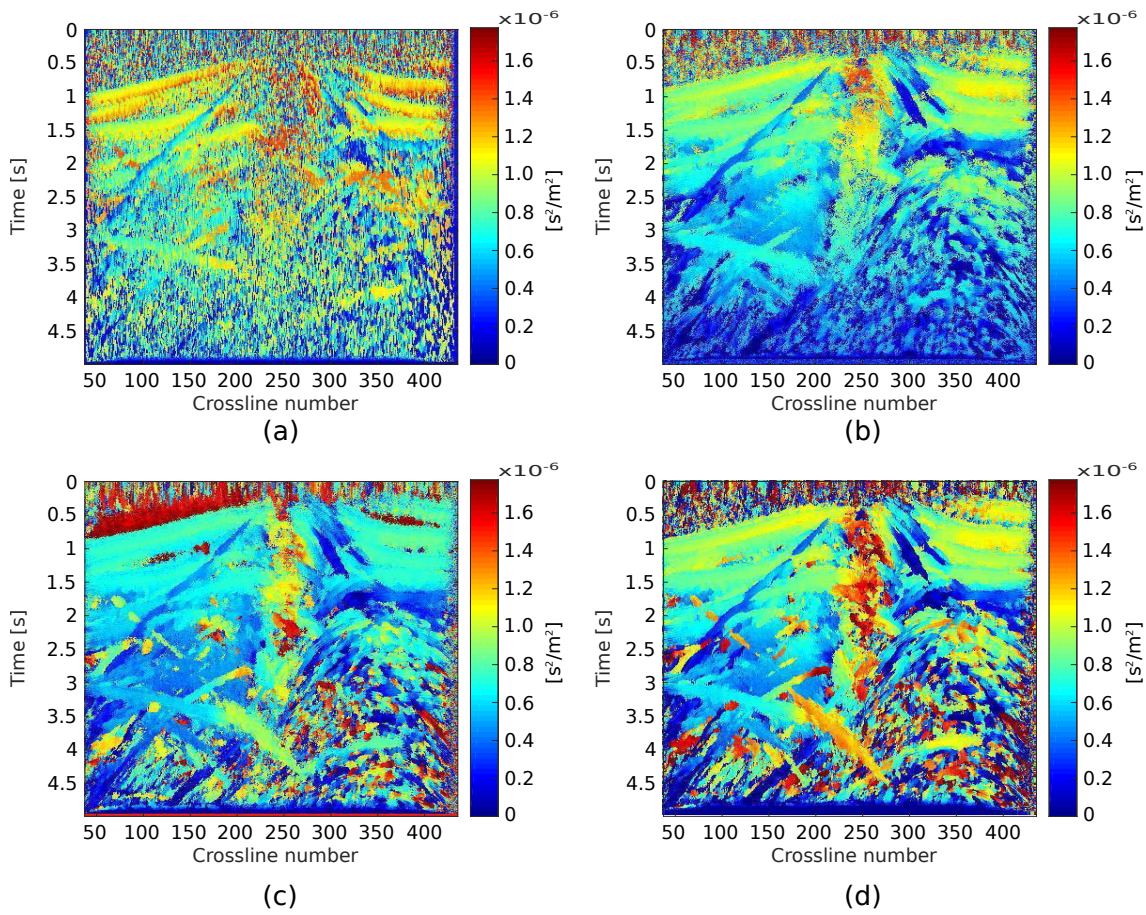


Figure 2.15.: Inline 190 of M_{11} volume obtained by (a) pragmatic approach, (b) particle swarm optimization (PSO), (c) genetic algorithm (GA), and (d) differential evolution (DE).

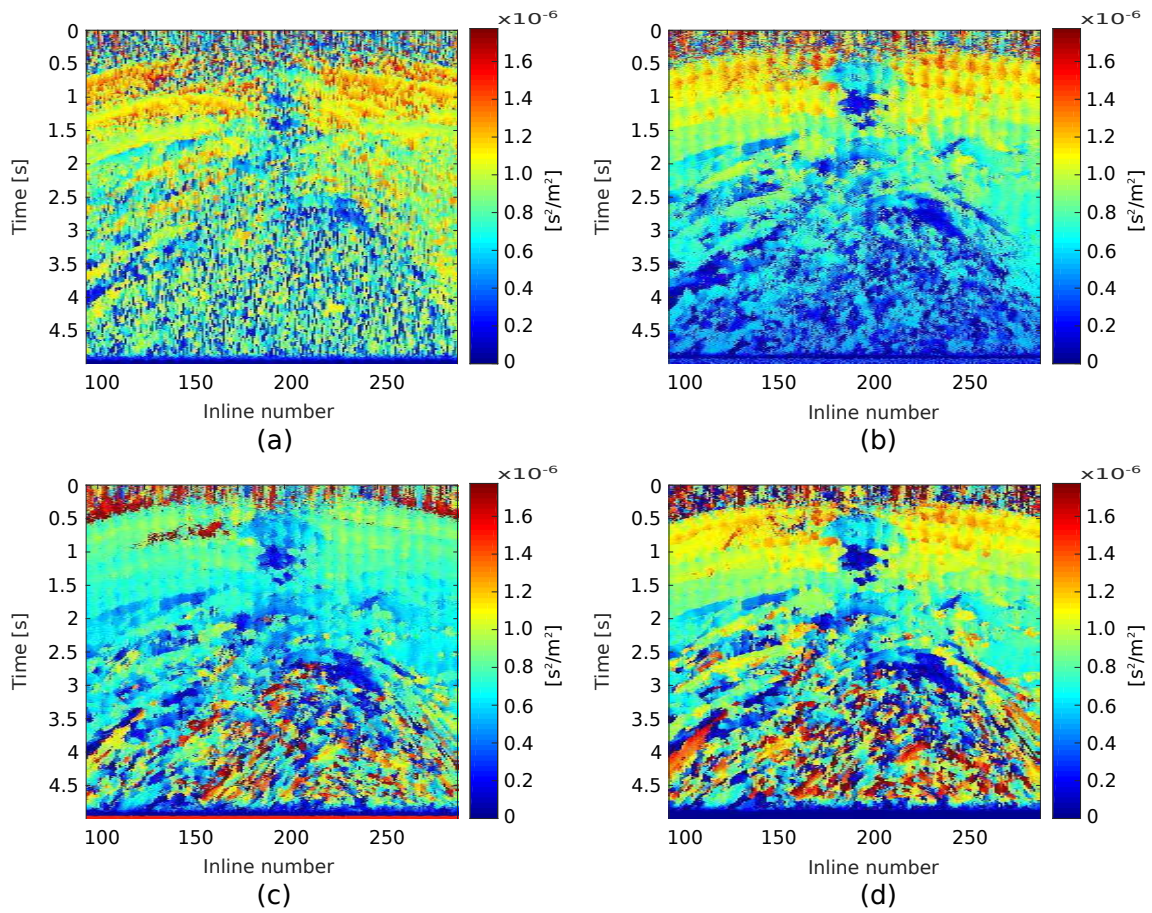


Figure 2.16.: Crossline 300 of M_{11} volume obtained by (a) pragmatic approach, (b) particle swarm optimization (PSO), (c) genetic algorithm (GA), and (d) differential evolution (DE).

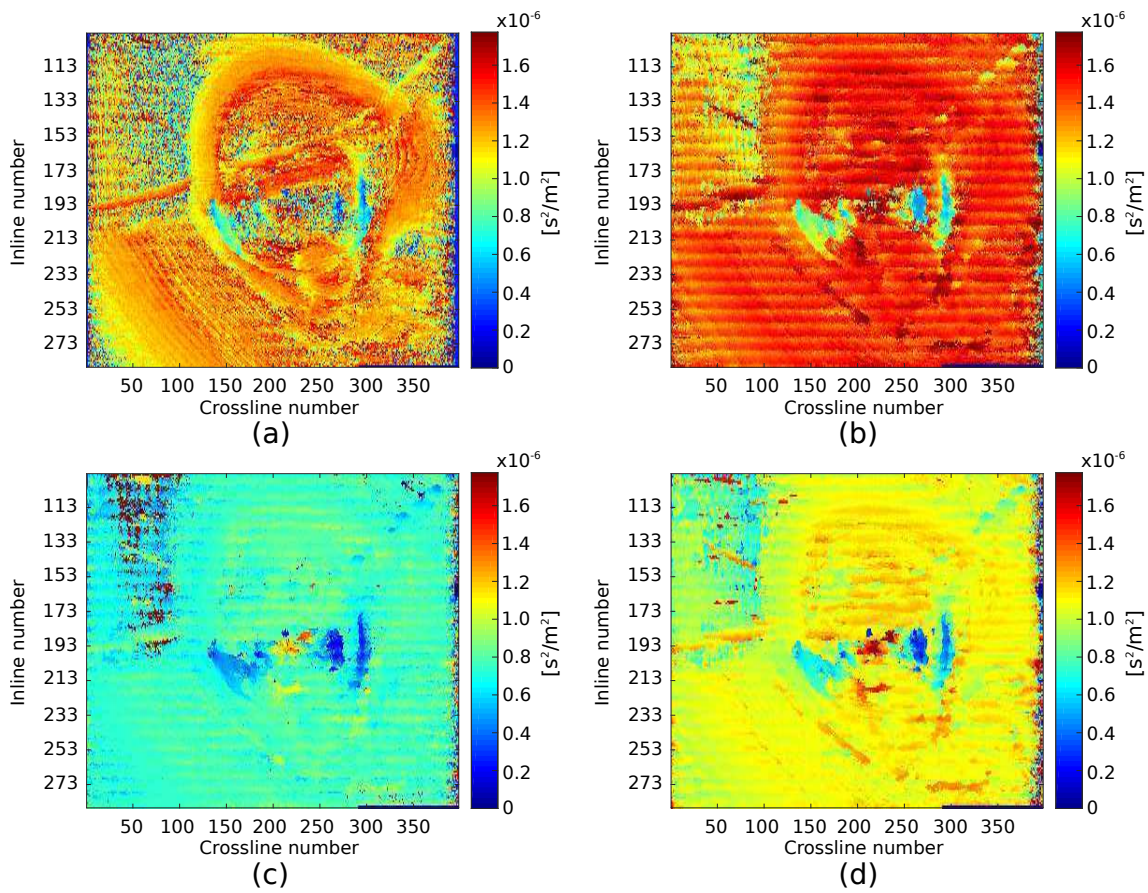


Figure 2.17.: Time slice 1.2 s of the M_{11} volume obtained by (a) pragmatic approach, (b) particle swarm optimization (PSO), (c) genetic algorithm (GA), and (d) differential evolution (DE).

Chapter 3.

5-D interpolation with wavefront attributes

Three-dimensional (3-D) prestack seismic data are often recorded in the five-dimensional (5-D) data space: four spatial dimensions and one temporal dimension (e.g., common-midpoint (CMP) coordinates in x and y , azimuth, offset, and time). As some natural and anthropogenic factors, e.g., field obstacles, dead traces, and budgetary constraints, 3-D prestack seismic data may be irregularly and sparsely sampled during data acquisition, which would affect the image quality of further applications. In order to resolve this problem, a simple and straightforward strategy is to introduce interpolated traces into these data gaps. In the literature, there are about five categories of interpolation methods reported. The first category is based on sparse transforms, such as Radon transform (e.g., [Kabir and Verschuur, 1995](#); [Trad et al., 2002](#); [Zhang and Lu, 2014](#)), Fourier transform (e.g., [Liu and Sacchi, 2004](#); [Zwartjes and Sacchi, 2007](#); [Trad, 2009](#); [Curry, 2010](#); [Naghizadeh and Innanen, 2011](#)), and Curvelet transform (e.g., [Naghizadeh and Sacchi, 2010](#)). With the sparse transforms, one can gradually attenuate the artifacts and recover the missing data information in the sparse domain by iteratively thresholding the transformed domain of the incomplete seismic data ([Chen et al., 2016b](#)). The second category of seismic interpolation methods is the prediction-filtering based interpolation methods (e.g., [Spitz, 1991](#); [Naghizadeh and Sacchi, 2009](#); [Liu and Fomel, 2011](#)), which interpolate high-frequency aliased data using prediction-error filters derived from low-frequency non-aliased data. This method works well with regularly sampled data. The third category of methods includes the Cadzow rank-reduction method (e.g., [Trickett, 2008](#); [Trickett et al., 2010](#); [Chen et al., 2016a,b](#)), or called the multichannel singular spectrum analysis (MSSA) method (e.g., [Oropeza and Sacchi, 2011](#); [Huang et al., 2015](#)). The rank-reduction-based interpolation methods assume that missing traces and random noise increase the rank of the constructed Hankel/Toeplitz matrices, and one can intuitively reduce the negative effects caused by the missing traces and random noise by applying rank-reduction operators (e.g., [Chen et al., 2016a,b](#)). They intuitively satisfy the local plane-wave assumption. The fourth seismic interpolation

methods is the wave-equation based methods (e.g., Ronen, 1987; Stolt, 2002; Fomel, 2003; Kaplan et al., 2010). They generally assume that the subsurface velocity is known and are computationally expensive solving the wave equation. The last kind of interpolation methods is the wavefront-attribute based interpolation (WABI, e.g., Höcht et al., 2009; Baykulov and Gajewski, 2009, 2010; Xie and Gajewski, 2016b; Xie, 2017), which is a data-driven, velocity independent interpolation technique extended from e.g., the Common-Reflection-Surface (CRS) method (e.g., Jäger et al., 2001; Mann, 2002; Höcht, 2002; Müller, 2003). This kind of interpolation methods utilizes wavefront attributes derived from moveout of events for several neighboring CMP gathers. The missing traces are predicted by the so-called partial stack. Examples are the partial CRS stacking (e.g., Baykulov and Gajewski, 2009, 2010), which can significantly increase the signal-to-noise ratio (S/N) of every trace and fill the data gaps after the interpolation. In this fashion a regularized 3-D data volume with improved S/N is generated. Since the wavefront attributes are derived from moveout which contains information on reflector dip, strike, and curvature, I consider this kind of interpolation techniques as physics-based interpolation methods to distinguish them from pure mathematics-based interpolation approaches. The WABI method is performed within the first Fresnel zone and therefore it uses traces in the interpolation process, which resolve the same structural details. Since the wavefront attributes are determined by kinematic features of the wave field, i.e., moveout, aliasing issues are relaxed. Next to the CRS operator any other operator utilizing wavefront attributes like i-CRS (Schwarz and Kashtan, 2014), non-hyperbolic CRS (Fomel and Kazinnik, 2013) or multi-focusing (Gelchinsky et al., 1999) can be used. These operators determine wavefront attributes from pre-stack data equally well (Walda and Gajewski, 2017). The 3-D partial CRS method (Baykulov and Gajewski, 2010) was successfully applied to denoise and reconstruct 3-D prestack seismic data with low S/N. However, two potential problems need to be addressed in this method and are considered in this work:

- i) To obtain high-quality 3-D wavefront attributes their determination should be performed with global optimization. The above-mentioned publication adopted a pragmatic search strategy in sub-volumes of the data which may lead to a poor or insufficient fit of the adapted traveltimes surface to the full data volume. As any other processing step using wavefield attributes also the 3-D partial CRS benefits of high-quality attributes.
- ii) To regularize traces within each 3-D CMP gather, an azimuth-based regularization process would be better to be developed to account for the wide-, rich- or full-azimuth acquisition. In previous works the regularization was performed along a specific azimuth which does not exploit the potential of different azimuth acquisition.

An effective solution to resolve the first problem in the conventional 3-D partial

CRS method is to develop a global search strategy which determines the wavefront attributes globally from the entire 5-D data space by assuming that the wave kinematics are properly described by the 3-D CRS traveltime formula. The wavefront attributes with global determination have presented in **Chapter 2**, where I found that the DE is the most stable algorithm to globally determine the 3-D CRS wavefront attributes when compared with the PSO, GA, and the conventional pragmatic approach. Hence, in this chapter, the DE algorithm is utilized for the global determination of the 3-D wavefront attributes. To address the trace regularization problem, an azimuth-based regularized strategy is presented in this chapter for the trace regularization in each 3-D CMP gather.

In this chapter, I first describe the basic concept of the WABI method for the 5-D interpolation purpose, e.g., based on the 3-D partial CRS method, where I call this interpolation method as 5-D WABI since it works in the 5-D data space. Then I compare the 5-D WABI method with the conventional 3-D partial CRS method using the 3-D SEG data as an example. Finally, to check the potential usage of the proposed 5-D WABI method, a comparison of the 5-D WABI with a mathematics-based 5-D seismic interpolation, e.g., based on the damped rank-reduction method (see [Chen et al., 2016b](#)), is presented, using a simple 3-D synthetic data of a diffraction event and the complex 3-D SEG data.

3.1. 5-D WABI

As a 5-D interpolation technique aside from nowadays mathematics-based 5-D seismic interpolation, the 5-D WABI applies the wavefront attributes that has specific physical meaning in actual applications. The wavefront attributes thereby can be determined by the 3-D CRS approach while taking the semblance as an objective function. I call the 5-D WABI method as a physics-based interpolation distinguishing it to the other mathematics-based 5-D interpolation. Practically, there are several steps need to be pointed out when the 5-D WABI method is utilized:

Firstly, I compute the midpoint locations $\mathbf{m} = (m_x, m_y)$ for each 3-D CMP gather of the 3-D data. In each 3-D CMP gather, I get $\mathbf{m} = (\sum_{i=1}^n \mathbf{m}_i)/n$, where \mathbf{m}_i is the midpoint location of a shot \mathbf{s} and a receiver \mathbf{g} , i indicates the shot-receiver pair, and n is the number of pairs in this 3-D CMP gather. For each receiver trace in this 3-D CMP gather, I have $\mathbf{m}_i = (\mathbf{g} + \mathbf{s})/2$ and $\mathbf{h}_i = (\mathbf{g} - \mathbf{s})/2$, where $\mathbf{s} = (s_x, s_y)$, $\mathbf{g} = (g_x, g_y)$, $\mathbf{m}_i = (m_{i,x}, m_{i,y})$, and $\mathbf{h}_i = (h_{i,x}, h_{i,y})$.

Secondly, the location of a given 3-D CRS gather is determined by a 3-D CMP gather located at $\mathbf{m}_{zo} = (m_{zo,x}, m_{zo,y})$. I often apply two steps to read traces into a given 3-D CRS gather:

(i) reading traces into the given 3-D CRS gather if all traces in the 3-D data satisfy: $(m_x - m_{z_o,x})^2/am_x^2 + (m_y - m_{z_o,y})^2/am_y^2 \leq 1$, where the denominator am_x and am_y are the midpoint aperture (see Figure 3.1 a), and m_x and m_y indicate any 3-D CMP position located within the red ellipse centred at the given 3-D CMP location of $\mathbf{m}_{z_o} = (m_{z_o,x}, m_{z_o,y})$. The number of 3-D CMP gathers used in the given 3-D CRS gather depends on the midpoint aperture that can be estimated by the Fresnel zone (e.g., Hubral et al., 1993a) or tested by the user.

(ii) selecting traces into the offset dimension if all traces obtained in step (i) satisfy: $h_{i,x}^2/h_{x,i}^2 + h_{i,y}^2/h_{y,i}^2 \leq 1$, where the denominator $h_{x,i}$, $h_{y,i}$ are the offset aperture centred at t_{z_o} (see Figure 3.1 b). The offset aperture at each ZO traveltime can be computed from the pre-determined offset aperture: $h_{x,0}$, $h_{y,0}$, $h_{x,n}$, and $h_{y,n}$ (see **Appendix A**). The elliptical aperture used in this work is not the only way to select traces into a given 3-D CRS gather, but it is a good solution preferable to a rectangular surface, based on my tests on the open 3-D SEG C3WA data.

In the next step I determine the traces which contribute to a given 3-D partial CRS gather. The given 3-D CRS gather is already loaded into the computer memory. If traces within the given 3-D CRS gather satisfy the relation $(h_{i,x} - offx)^2/p_{x,i}^2 + (h_{i,y} - offy)^2/p_{y,i}^2 \leq 1$, they are selected into the given 3-D partial CRS gather centred at $(offx, offy)$, where $p_{x,i}$ and $p_{y,i}$ are the semi-major and semi-minor axes of the horizontal ellipse (blue) (see Figure 3.1 b). Both the $p_{x,i}$ and $p_{y,i}$ are estimated by the pre-determined apertures: a , b , c , and d (see **Appendix A**).

After this step I compute the ZO traveltime $t_{z_o,p}$ for the 3-D partial CRS operator. For a sample A on trace k with $\mathbf{h} = (offx, offy)$, the $t_{z_o,p}$ can be obtained with the following traveltime operator in each 3-D CMP gather.

$$t_{22}^2(offx, offy) = t_{11}^2 + \mathbf{h}^T \mathbf{M} \mathbf{h}. \quad (3.1)$$

I assume the ZO traveltime $t_{z_o,p} = t_{11}$ if the calculated t_{22} satisfy: $(t - t_{22})^2 \leq fmin^2$, where t_{11} is the trial ZO traveltime, and t_{22} is the calculated hyperbolic traveltime (see Figure 3.2 a). A refinement of the $t_{z_o,p}$ using Equation 3.1 at the sample A may be considered after the wavefront attributes of $t_{z_o,p}$ are obtained. The eight wavefront attributes of $t_{z_o,p}$ are read from the attribute files (a byproduct of the DE algorithm), which will be used in the following 3-D partial CRS operator for the 5-D interpolation purpose.

$$t_{hypp,p}^2 = (t_{z_o,p} + 2\mathbf{p} \cdot \mathbf{m}_c)^2 + \mathbf{m}_c^T \mathbf{N} \mathbf{m}_d + \mathbf{h}^T \mathbf{M} \mathbf{h}. \quad (3.2)$$

Equation 3.2 is a 5-D interpolation operator in the time domain. With this operator, the sample A is interpolated at t on trace k located at $(m_{0,x}, m_{0,y}, offx, offy)$. The same process is performed for each sample on trace k , and other traces in the 3-D CMP gather, as well as other 3-D CMP gathers in the whole 3-D data.

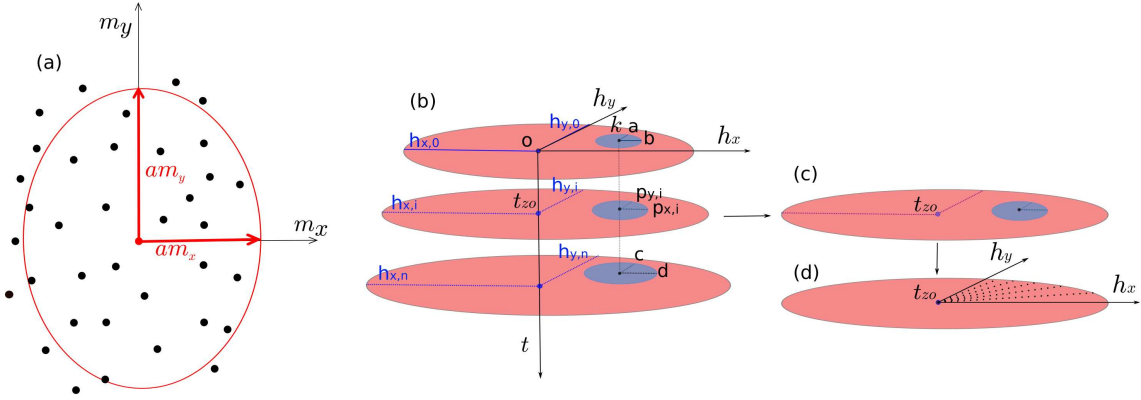


Figure 3.1.: CRS and partial CRS apertures used in this work. (a) A given 3-D CRS gather consisting of several 3-D CMP gathers, where the black dots denote locations of the 3-D CMP gathers. (b) A considered 3-D CMP gather and its corresponding 3-D partial CRS offset aperture (blue) in this 3-D CMP gather. Note: the blue ellipse here is only a subset of whole 3-D partial CRS aperture in the offset direction. (c) The considered time slice at t_{zo} . (d) An azimuth-based regularization performed at t_{zo} , where the black grid points are the trace location regularized along different azimuth directions. Here only the positive offsets are shown, and the constant azimuthal angle between the dashed lines is the azimuthal interval. More details see Figure 3.3.

In each 3-D CMP gather of the 3-D data, each trace's location is regularized by an azimuth-based regularization in the offset dimension (see Figure 3.1 d and Figure 3.3), where different azimuthal directions are considered. In practice, the 3-D partial CRS apertures and the azimuthal intervals are tested from the 3-D data. I often perform a series of tests to find the optimized 3-D partial CRS apertures and azimuthal intervals. Amplitude variation in the midpoint dimension can be estimated by the modulus of geometrical spreading factor (e.g., Hubral et al., 1993b; Schleicher et al., 1993a). Shuey's approximation (Shuey, 1985) can be applied to analyze the amplitude versus offset (AVO) in the offset dimension in each 3-D CMP gather. The amplitude of the sample A is a summation of all amplitudes along the 3-D partial CRS traveltime surface within the 3-D partial CRS aperture, i.e., an improvement of the S/N ratio is obtained. Considering the AVO may be omitted since I stack locally along the offset direction. However, the AVO analysis is necessary while dealing with data of larger gaps since in such case a large offset aperture for the 3-D partial CRS stacking is applied to ensure more traces included.

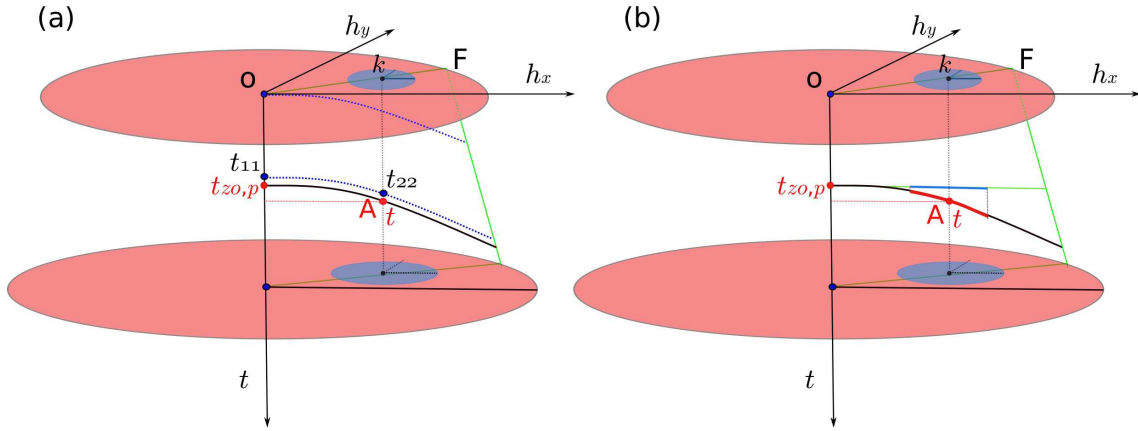


Figure 3.2.: Calculating $t_{zo,p}$ and construct 3-D partial CRS stacking operator for a sample A on trace k located at $(m_{zo,x}, m_{zo,y}, offx, offy)$. (a) Calculating the $t_{zo,p}$ by a traveltime fitting process. For the sake of simplicity, only one direction (OF) is shown. The black curve is an observed seismic event at this direction. In order to find $t_{zo,p}$, the traveltime operator (Equation 3.1) is used. I start from the first ZO sample (see the top blue dashed curve), then the traveltime surface (Equation 3.1) is moved downward until the condition satisfies: $(t - t_{22})^2 \leq fmin^2$, where I assume $t_{zo,p} = t_{11}$. To better understand, the traveltime difference between $t_{zo,p}$ and t_{11} shown in this figure is exaggerated. In practice, the difference between $t_{zo,p}$ and t_{11} is very small. Usually, I will refine $t_{zo,p}$ using the simulated sample A if the wavefront attributes around $t_{zo,p}$ are smooth. The coefficient $fmin$ can be automatically calculated by the wavefront attributes of two neighboring ZO samples around $t_{zo,p}$. The right green line is a boundary of the offset aperture in the OF direction. (b) An intersection (red curve) of the 3-D partial CRS traveltime surface with the vertical OF plane, where its top horizontal short (blue) line is the partial CRS aperture for sample A in OF direction. Aside from the red curve, other parts of the 3-D partial CRS traveltime surface at current CMP gather as well as at its neighbouring CMPs are not shown here. The whole 3-D partial CRS traveltime surface is expressed as Equation 3.2.

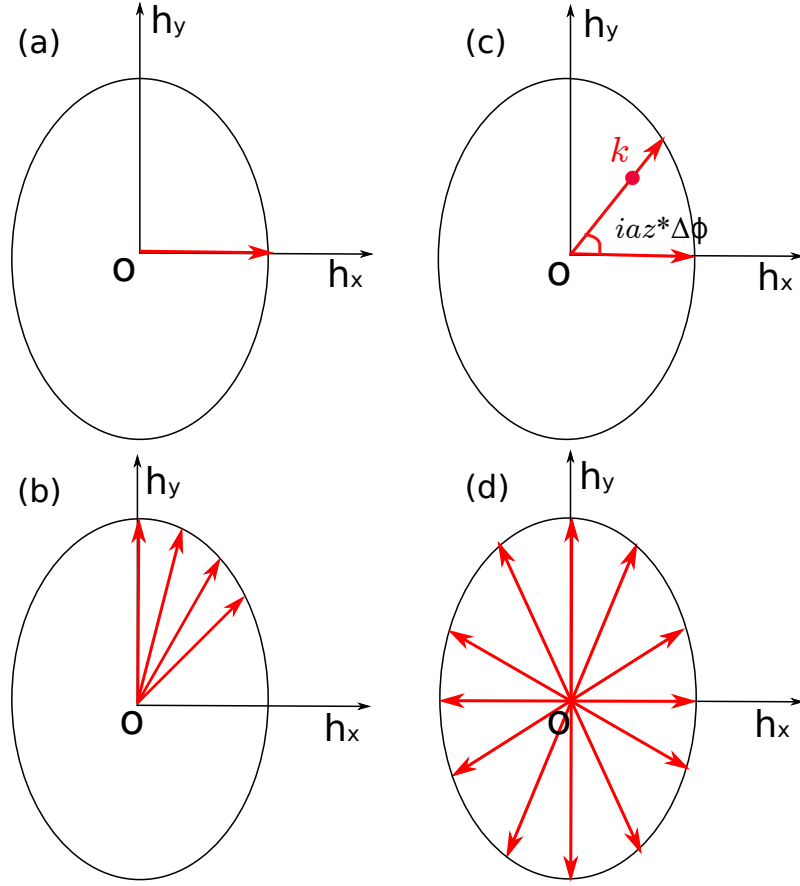


Figure 3.3.: Different azimuth-based regularization strategies. (a) An azimuth-fixed regularization (e.g., $\phi = 0$). (b) Narrow azimuth regularization. (c) Regularization of one trace k ($offx$, $offy$) on the azimuth direction of $iaz * \Delta\phi$, where $\Delta\phi$ is the azimuth interval, the sign $*$ denotes a multiplication, and iaz indicates the number of azimuth intervals starting (counter-clockwise) from $\phi = 0$. (d) A wide- or full- azimuth regularization. For each azimuth direction $iaz * \Delta\phi$ in the 3-D CMP gather, I set $h_x = h_y / \tan(0 + iaz * \Delta\phi)$ and $h_y = j * \Delta h_y$, where $j = 0, 1, 2, \dots, Intmax(h_y) / \Delta h_y$. The function $Intmax()$ returns the maximum integer value of h_y and Δh_y is the offset increment in the h_y direction. The azimuth interval $\Delta\phi$ and offset increment Δh_y should be set by the user in different data. In the 3-D SEG case, I use $\Delta\phi = 6 * \pi / 180$ and $\Delta h_y = 30$ m, which need to be tested from the data, e.g., several $\Delta\phi$ and Δh_y are tried until the one with the best result is gotten. For the 3-D SEG data, the azimuth range can be set between $[-\pi, 0]$ or $[\pi, 2\pi]$, seeing the data acquisition geometry. For the azimuth-based regularization, I do the same calculation for the 3-D simple data discussed in **Chapter 3.3** where the offset interval is set in the x direction, i.e., $\Delta h_x = 30$ m.

3.2. 3-D partial CRS stacking and 5-D WABI

The 3-D SEG C3WA data is used here for the interpolation purpose. To see the performance of the conventional 3-D partial CRS stacking and the 5-D WABI method in this work, 50% traces in the 3-D SEG data were randomly killed. The midpoint and offset apertures designed for the 3-D SEG data utilized in this work are given in **Appendix A**.

3.2.1. Usage of pragmatic approach and DE

Before I present a comparison of the conventional 3-D partial CRS stacking with the 5-D WABI method, the wavefront attributes require to be determined from the gapped 3-D SEG data by the pragmatic approach (3-D partial CRS) and by the DE algorithm (5-D WABI). Related to the pragmatic approach, the reader can reference Müller's work (see Müller, 2003). Additionally to **Chapter 2**, I briefly summarize how to use the DE algorithm in the 3-D CRS case for the 5-D interpolation purpose. Four parameters need to be determined in the DE algorithm. The first two are the differential weight F and the crossover probability CR , a priori suggested values are given by Pedersen (2010). However, I found that the F and CR may be slightly different with different objective functions. In this work, I use $F = 1.2$ and $CR = 0.9$ for maximizing the semblance. The last two parameters are the population size NP and the number of iterations IT , which also need to be tested from the data. In my tests to the 3-D SEG data, I found that a safe suggestion of the NP should be larger than 40, and the IT would be better larger than 50 (see **Chapter 2**). In order to determine the F and CR in the above, a very large IT and NP needs to be trialled at the beginning to make sure the DE results only sensitive to F and CR , then the IT and NP are estimated with the obtained F and CR .

3.2.2. Semblance difference between pragmatic approach and DE

To see the semblance difference between the pragmatic approach and the DE algorithm, three sections of the 3-D semblance volume are shown. These are a time slice of 1.2 s, inline 190, and crossline 300 (see Figure 3.4 and Figure 3.5). The semblance difference of the three sections indicates that, for close to 90% of the zero-offset (ZO) samples, the semblance provided by the DE algorithm is higher than the one provided by the pragmatic approach. A detailed semblance comparison of four ZO samples taken from the 3-D semblance volume is shown in Figure 3.6, where the

semblance provided by the DE algorithm turns out to be higher. The computational efficiency between the traditional pragmatic approach and the DE algorithm is shown in **Chapter 2**, where the DE is more efficient.

3.2.3. Two CMP gathers

To see the differences between the 3-D partial CRS stacking and the 5-D WABI method on individual 3-D CMP gather, two 3-D CMPs are shown in this work. Both are randomly selected without any preference.

The first one is CMP 181903 (see Figure 3.7, displayed in a 2-D section, i.e., all traces are sorted with increasing offsets). In this gather, seismic events on the raw data are visible but unclear. Figure 3.7b shows the same data but some traces were deleted to simulate data gaps. After determination of the 3-D CRS wavefront attributes obtained from the reduced 3-D data, the conventional 3-D partial CRS stacking and the 5-D WABI method are applied separately. Figure 3.7c displays this 3-D CMP gather processed by the conventional 3-D partial CRS stacking, where the reflection events are clearly visible and continuous with less noise, compared to the raw and gapped 3-D CMP gather (Figure 3.7 b). Figure 3.7d shows the same 3-D CMP gather but processed by the 5-D WABI method, which also displays improved results compared to the raw and gapped 3-D CMP gather. In this 3-D CMP gather with CMP 181903, I do not see a big different result between the conventional 3-D partial CRS stacking and the 5-D WABI method.

The second example shows data for CMP 182113 of the 3-D SEG data, which is noisier and the seismic events are difficult to identify. After processing with the conventional 3-D partial CRS stacking and the 5-D WABI method the gaps are filled and the reflection events are clearly visible (see Figure 3.8c and d). However, the result of 5-D WABI displays an improved result. The semblance is used to confirm this visual observation.

3.2.4. Two CO sections

In order to see the interpolation results on more 3-D CMP gathers simultaneously, two 3-D common-offset (CO) volumes are shown. In each 3-D CO volume, a 3-D CMP gather contains only one trace, and all traces in the 3-D CO volume have the same half offset. The first 3-D CO volume is chosen from a constant half offset of $\mathbf{h} = (0 \text{ m}, 100 \text{ m})$. The second 3-D CO volume is taken from a far constant half offset with $\mathbf{h} = (0 \text{ m}, 1000 \text{ m})$. In each of the two 3-D CO volumes, three sections comprising the salt body are considered. These are inline 190, crossline 300, and a

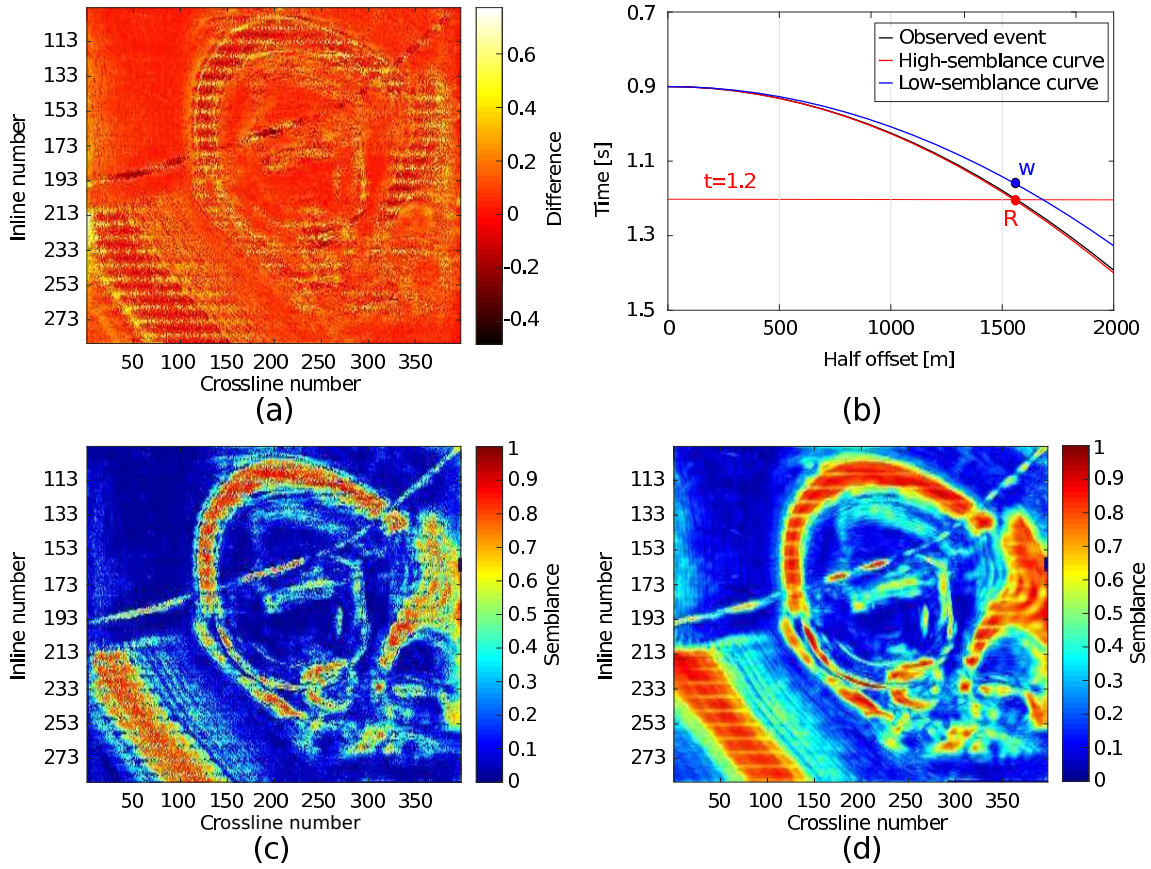


Figure 3.4.: Semblance and semblance difference for time slice 1.2 s of the 3-D semblance volume. (a) Semblance difference between (d) and (c), where about 89.7% ZO samples have a positive semblance. (b) Interpolation operators with low and high semblance. (c) Semblance of time slice 1.2 s with pragmatic approach. (d) Semblance of time slice 1.2 s with DE global optimization. The semblance difference is computed by using the semblance of DE minus the semblance of pragmatic approach.

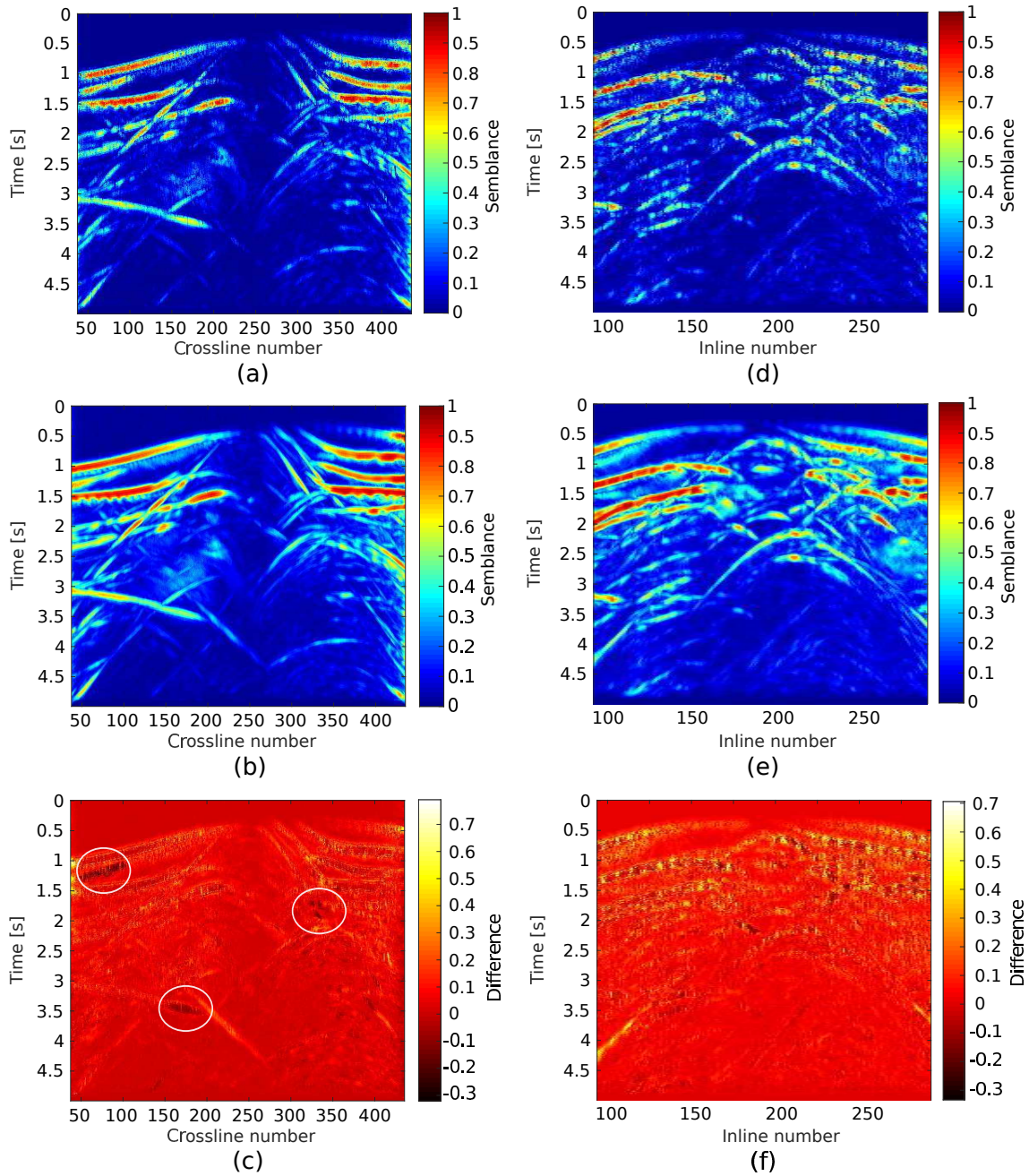


Figure 3.5.: Semblance and semblance difference for inline 190 and crossline 300 of the 3-D semblance volume. (a) Semblance of inline 190 with pragmatic approach. (b) Semblance of inline 190 with DE global optimization. (c) Semblance difference between (b) and (a), where about 88.7% ZO samples have a positive semblance. (d) Semblance of crossline 300 with pragmatic approach. (e) Semblance of crossline 300 with DE global optimization. (f) Semblance difference between (e) and (d), where about 88.1% ZO samples have a positive semblance. The semblance difference is computed by using the semblance of DE minus the semblance of pragmatic approach.

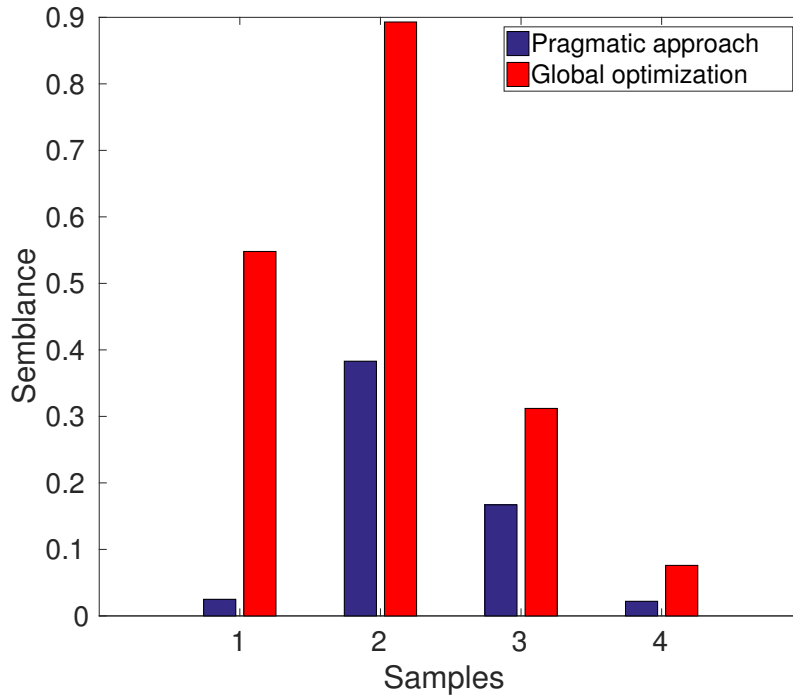


Figure 3.6.: Semblance of the four ZO samples mentioned in **Chapter 2**. The global optimization algorithm here is the DE algorithm.

time slice at 1.2 s. In these interpolation sections, all figures have the same color bar with a minimum (blue) and a maximum (red) amplitude ranged from -0.6 to 0.6.

Figure 3.9 shows inline 190 of the first 3-D CO volume, where the image quality of the raw data is poor, and many deep reflection events and diffraction patterns are almost invisible (see Figure 3.9a). Figure 3.9b displays the section with removed traces. A better continuity of horizons at different time levels can be seen and the S/N is increased significantly after the 3-D partial CRS stacking and the 5-D WABI method are applied. Some differences between the 3-D partial CRS stacking and the 5-D WABI method are marked by red arrows (see Figure 3.9c and d). Figure 3.10 shows crossline 300 of the first 3-D CO volume, where most of the seismic events shown on the raw data are difficult to identify except the top horizontal layers (Figure 3.10a). However, many reflection events and diffraction patterns are observed after the 3-D partial CRS stacking is applied. It can provide continuous seismic events at all time levels with a better S/N (see Figure 3.10c). Even improved results are obtained when the 5-D WABI method is applied (see Figure 3.10d), which displays more continuous events than the conventional 3-D partial CRS stacking. I note that the resolution of the crossline section is worse than that of the inline section. This is due to a sparse data acquisition along the inline direction. Figure 3.11 shows the

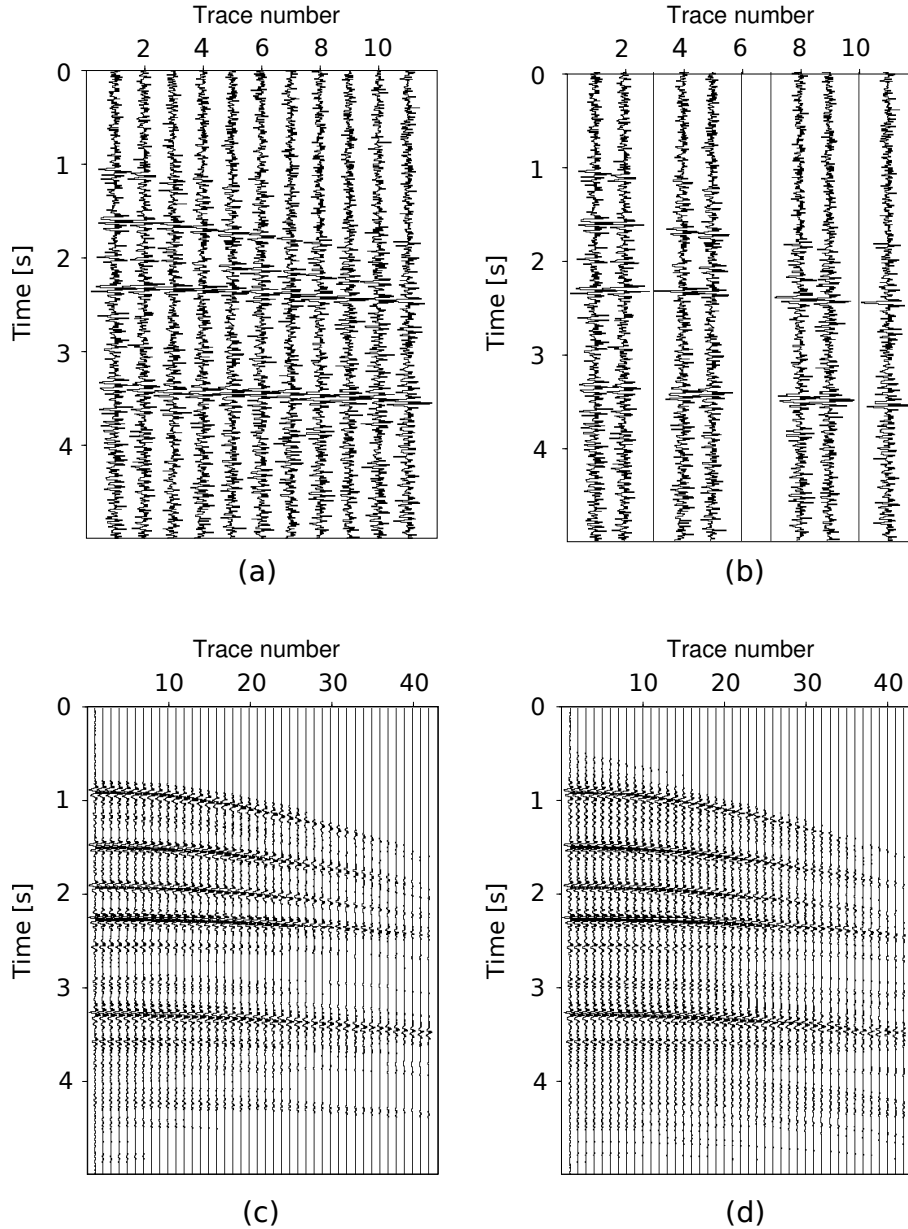


Figure 3.7.: A 3-D CMP gather (CMP 181903) picked from the 3-D SEG data. (a) Raw 3-D CMP gather with low S/N. (b) Raw 3-D CMP gather with gaps. (c) Interpolation with conventional 3-D partial CRS stacking. (d) Interpolation with 5-D WABI method. For the sake of simplicity, only the azimuth $\phi = \pi/2$ is shown in this 3-D CMP gather after the 5-D interpolation and regularization.

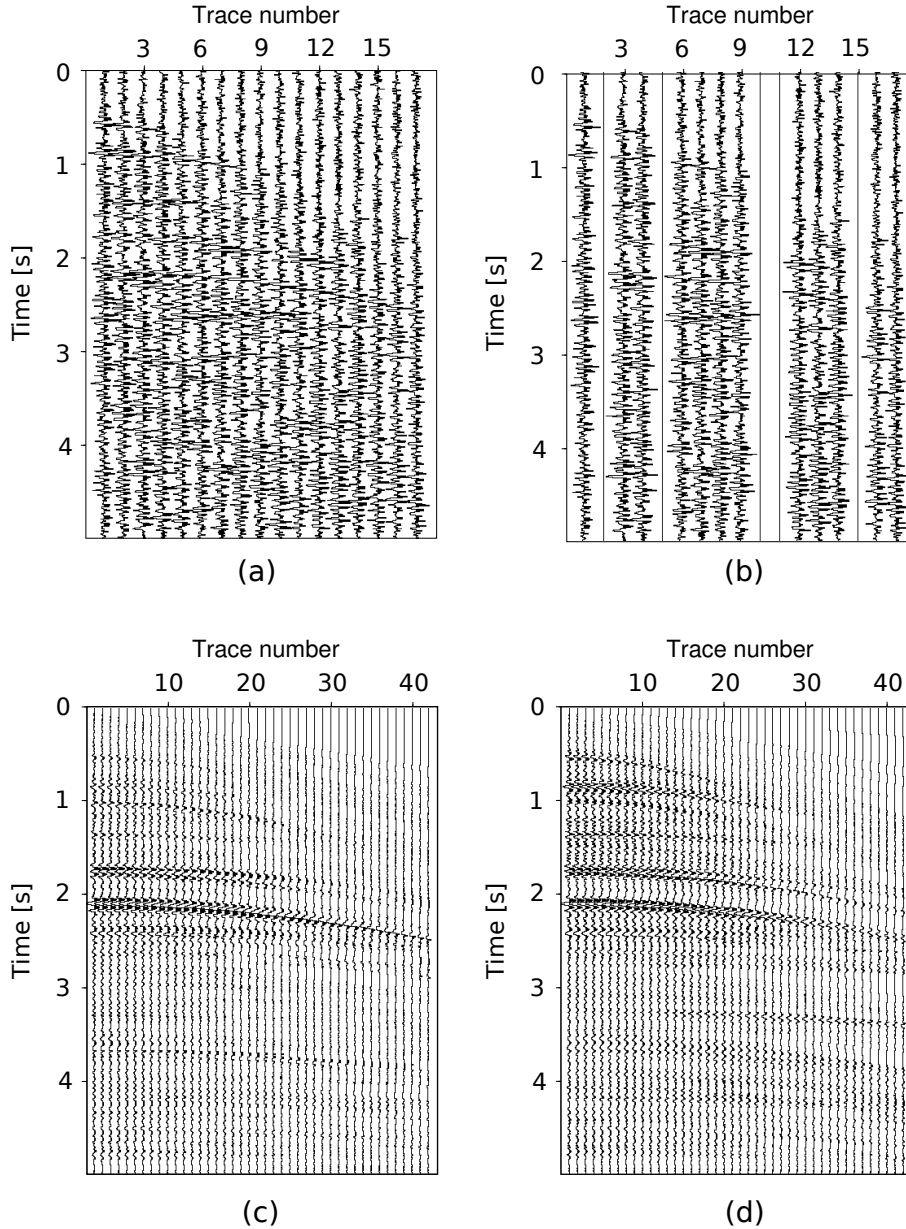


Figure 3.8.: A 3-D CMP gather (CMP 182113) picked from the 3-D SEG data. (a) Raw 3-D CMP gather with low S/N. (b) Raw 3-D CMP gather with gaps. (c) Interpolation with conventional 3-D partial CRS stacking. (d) Interpolation with 5-D WABI method. For the sake of simplicity, only the azimuth $\phi = \pi/2$ is shown in this 3-D CMP gather after the 5-D interpolation and regularization.

time slice 1.2 s of the first 3-D CO volume, where the structure of the salt body is hardly visible both on the raw time slice and the reduced time slice. However, a significantly improved result is obtained either by the 3-D partial CRS stacking or by the 5-D WABI method (see Figure 3.11c,d). Again, the latter performs better leading to smoother images than the conventional 3-D partial CRS for most of the ZO sample locations.

Results obtained from the second (far-offset) 3-D CO volume are significantly improved with the 5-D WABI method compared to the 5-D WABI method applied to the first (near-offset) 3-D CO volume. See the corresponding inline 190 and crossline 300 of the second 3-D CO volume (Figure 3.12, Figure 3.13). Figure 3.14 shows the time slice at 1.2 s, where the 5-D WABI method provides a smoother image with less noise, compared to the conventional 3-D partial CRS stacking. In the central part of the slice, the structure of the salt body imaged by the 5-D WABI method is better visible than the one obtained for the conventional 3-D partial CRS. For about 90% of the ZO samples, the results obtained for the 5-D WABI method are better than for the conventional 3-D partial CRS (as an example where this is not the case, see the right top corner of Figure 3.14c and Figure 3.14d). For these cases these areas, the semblance calculated from the DE-based wavefront attributes is lower than the semblance for the conventional 3-D partial CRS stacking (see Figure 3.4c,d). With low-semblance traveltime interpolation operator, the data sample may be interpolated at a wrong (W) position, instead of the right (R) position (see Figure 3.4b). Usually, one can use a local optimization algorithm to refine the DE-based wavefront attributes in these low-semblance areas. However, this option failed in my tests, where two local optimization algorithms, namely a modified simulated annealing (MSA) and the Nelder-Mead method were tested. I think that a local optimization may not guarantee to find or move forward to the global best if the initial guess is too far away from the global best. I conclude, that for most ZO samples, nearly 90% in this case, the results obtained from the 5-D WABI are obtained in better quality using less computational time.

Using the 5-D WABI method and considering several events for the same ZO sample (conflicting dips) may be cumbersome in the interpolation process if the data is complex with larger gaps. This conclusion, however, is applicable to trace interpolation in general since the projected Fresnel zone set physical limits with respect to size of handleable data gaps. For some ZO samples, the number of seismic events pertaining to a ZO sample can be counted and searched by the algorithm. In such case, a well-interpolated result can be obtained. However, at some ZO samples with sparse data comprising large data gaps, the 3-D hyperbolic or non-hyperbolic CRS traveltime operator may fail in the process of determining wavefront attributes which belong to different events of a ZO sample. Here, I consider only the dominant event at each ZO sample. Obviously, events not considered are not interpolated and therefore missing after the interpolation process. The conventional 3-D par-

tial CRS stacking has already demonstrated good performance for reflection data (see Baykulov and Gajewski, 2009, 2010). This work indicated that the 5-D WABI method provides reliable results for reflections and diffractions.

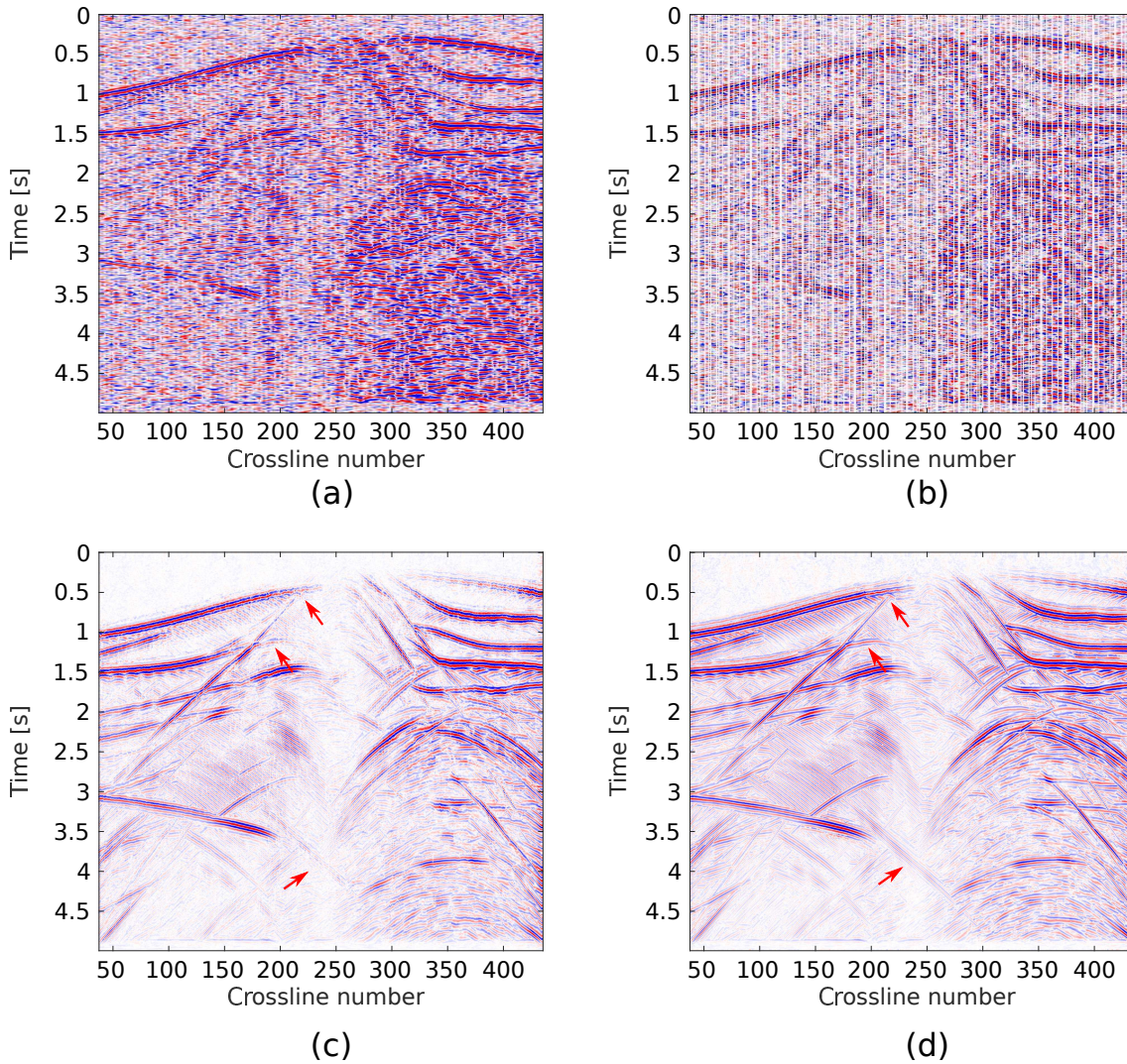


Figure 3.9.: Inline 190 of the first 3-D CO volume. (a) Raw CO section. (b) Raw CO section with gaps. (c) Interpolation with conventional 3-D partial CRS stacking. (d) Interpolation with the 5-D WABI method.

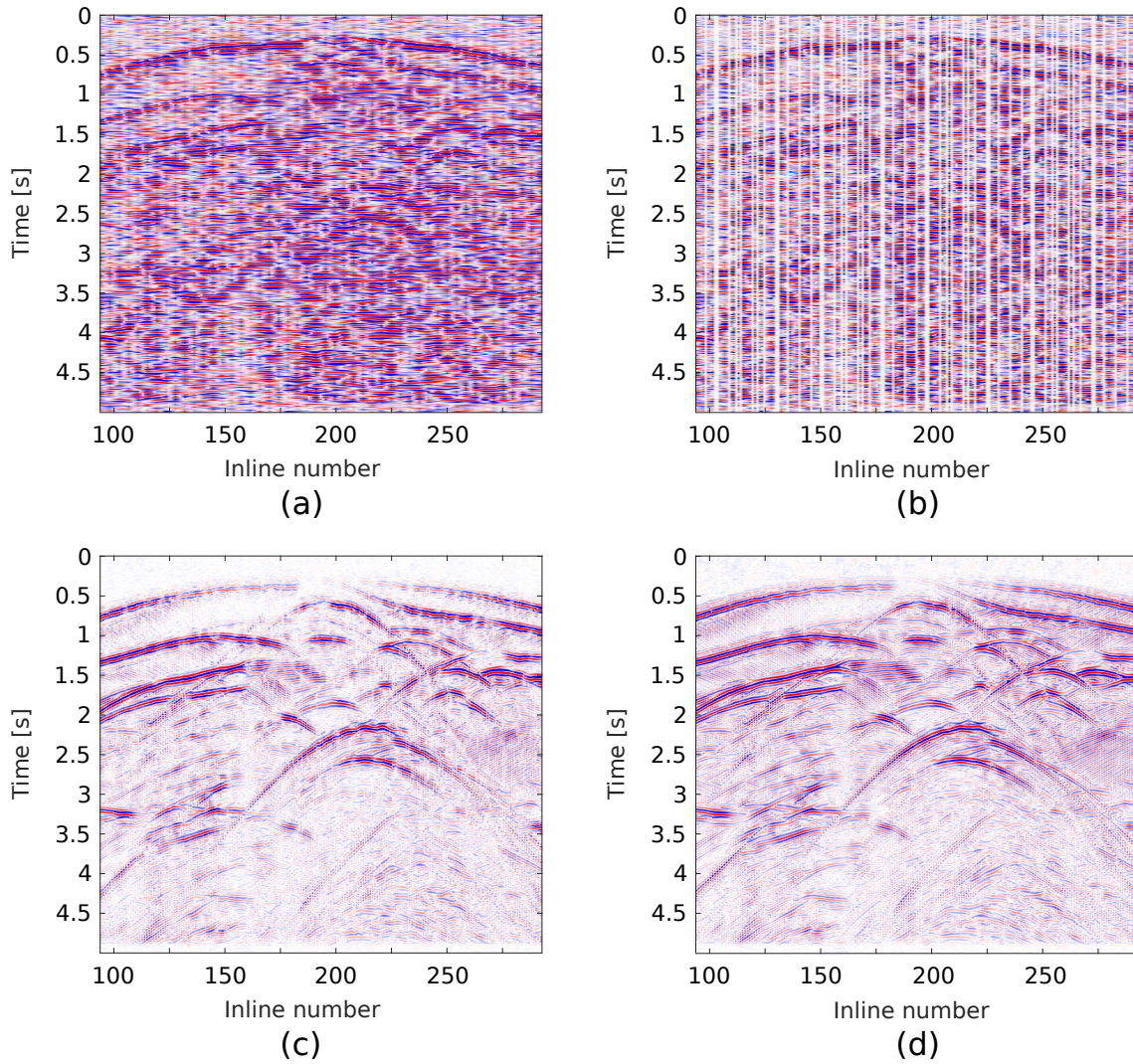


Figure 3.10.: Crossline 300 of the first 3-D CO volume. (a) Raw CO section. (b) Raw CO section with gaps. (c) Interpolation with conventional 3-D partial CRS stacking. (d) Interpolation with the 5-D WABI method.

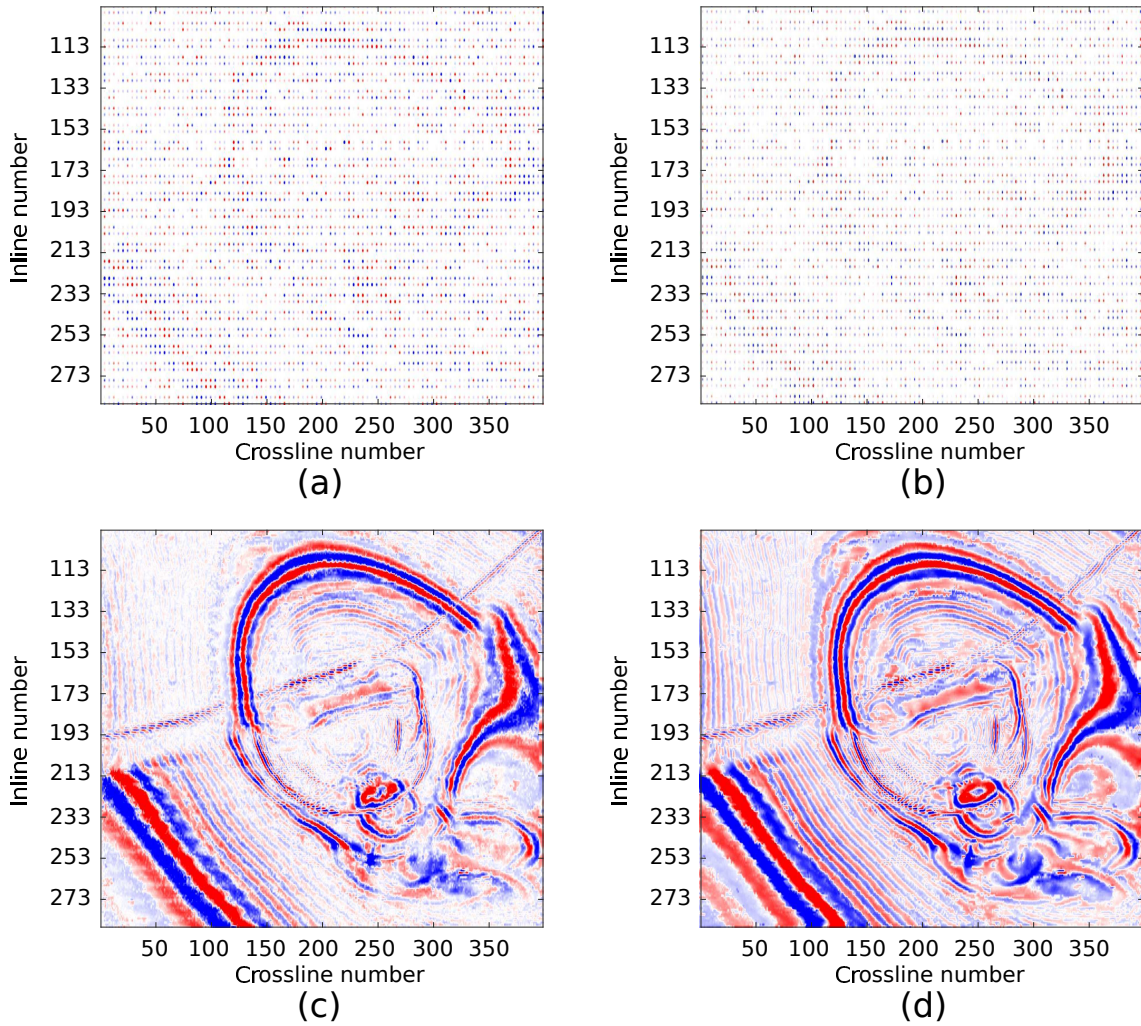


Figure 3.11.: Time slice 1.2 s of the first 3-D CO volume. (a) Raw data. (b) Raw data with gaps. (c) Interpolation with conventional 3-D partial CRS stacking. (d) Interpolation with the 5-D WABI method.

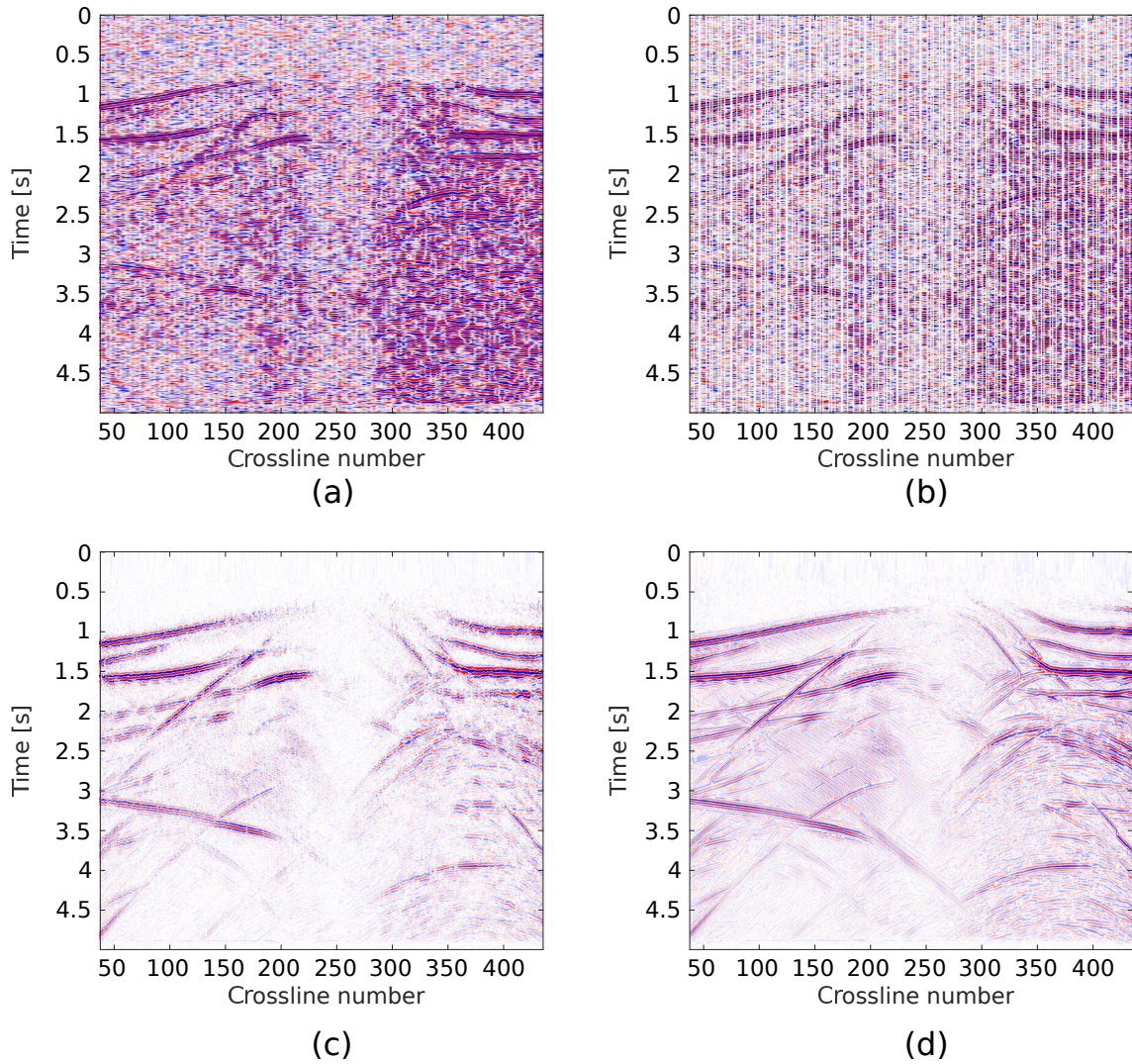


Figure 3.12.: Inline 190 of the second 3-D CO volume. (a) Raw CO section. (b) Raw CO section with gaps. (c) Interpolation with conventional 3-D partial CRS stacking. (d) Interpolation with the 5-D WABI method.

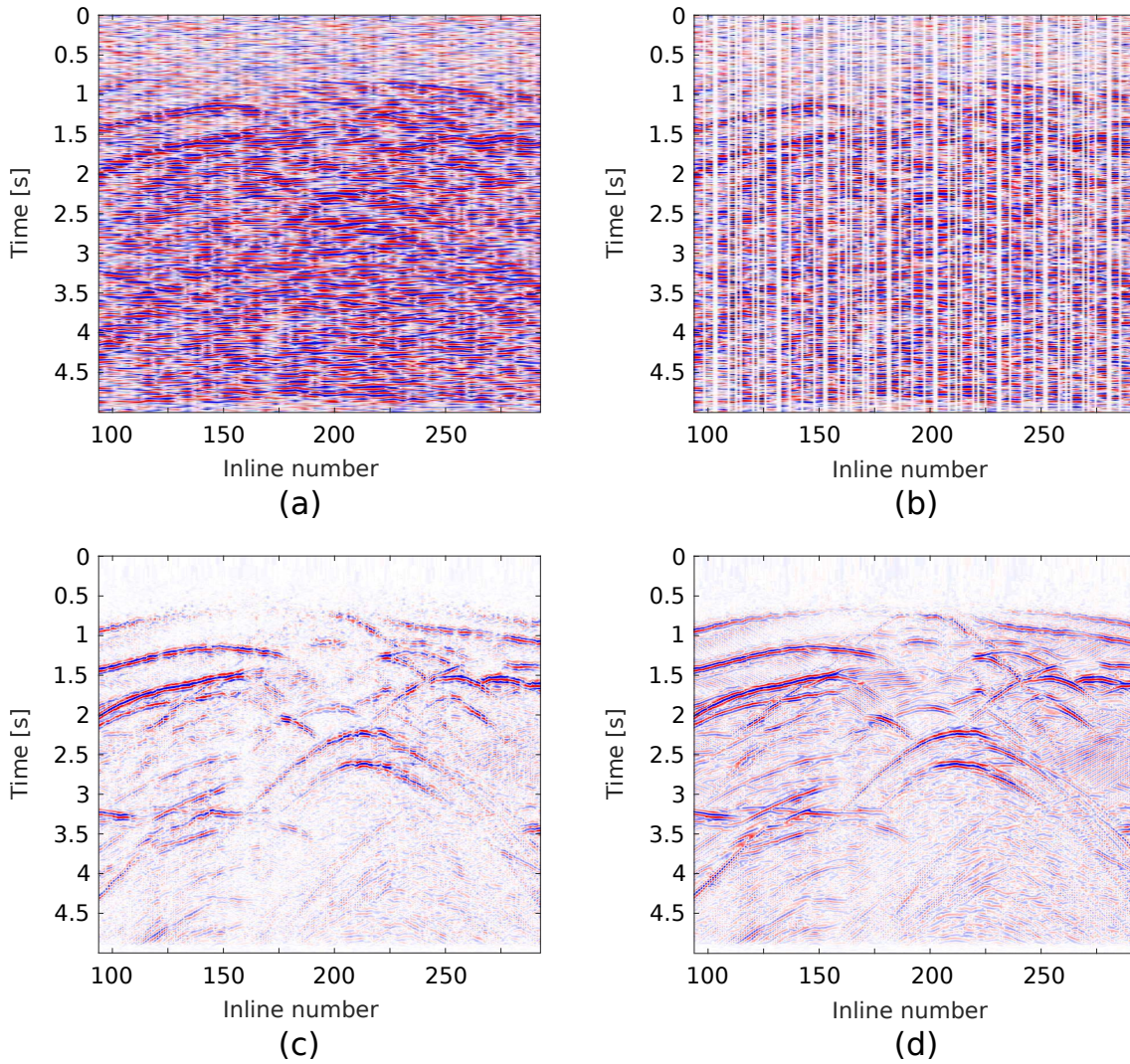


Figure 3.13.: Crossline 300 of the second 3-D CO volume. (a) Raw CO section. (b) Raw CO section with gaps. (c) Interpolation with conventional 3-D partial CRS stacking. (d) Interpolation with the 5-D WABI method.

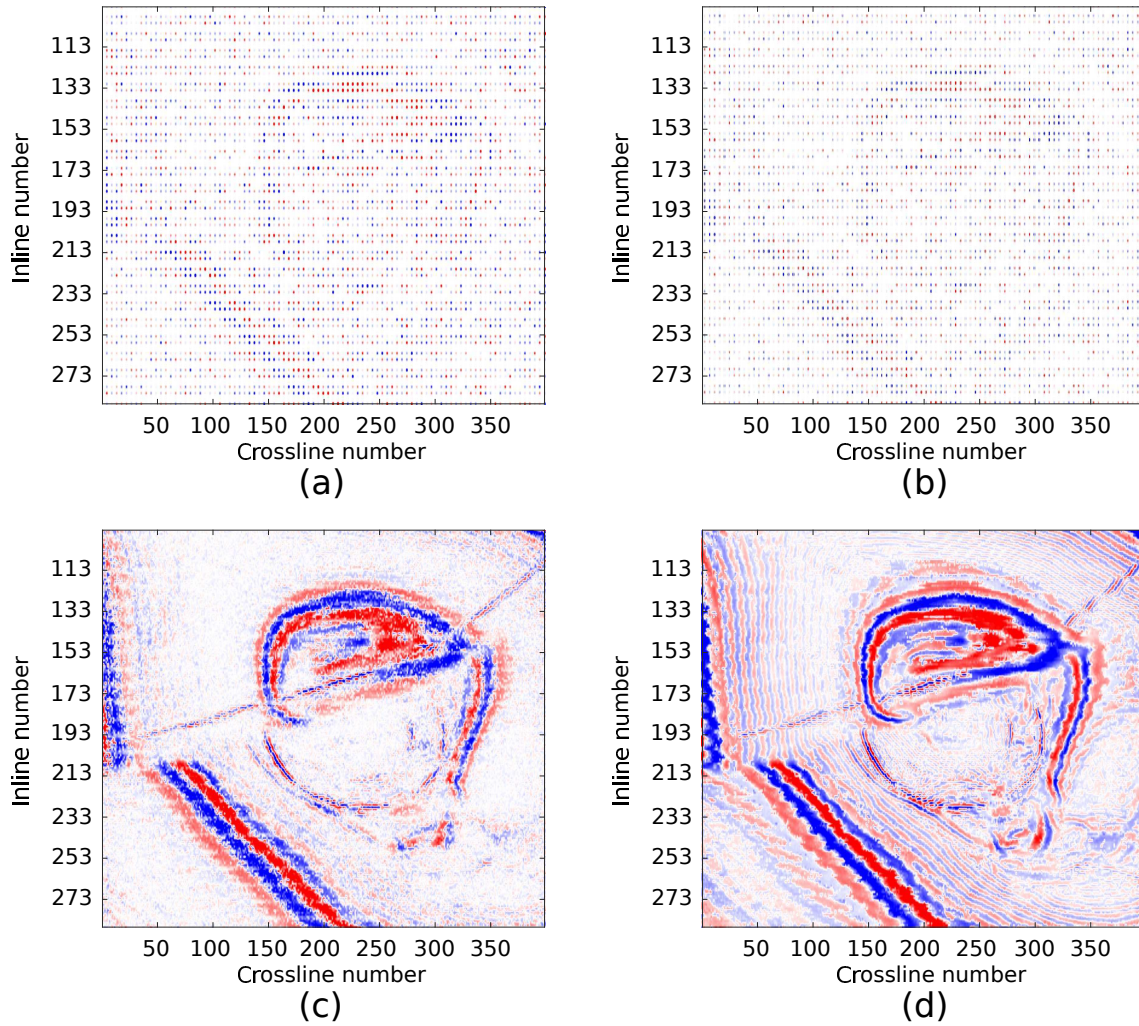


Figure 3.14.: Time slice 1.2 s of the second 3-D CO volume. (a) Raw data. (b) Raw data with gaps. (c) Interpolation with conventional 3-D partial CRS stacking. (d) Interpolation with the 5-D WABI method.

3.3. 5-D WABI and rank-reduction-based 5-D interpolation

The proposed 5-D WABI method, as an extension of the conventional 3-D partial CRS approach, has shown its potential to reconstruct reflection and diffraction data. However, related to the 5-D interpolation, there are several other types of 5-D seismic interpolation approaches proposed recently. In order to check the potential usage of the proposed 5-D WABI, I also compare it with the rank-reduction-based 5-D interpolation, e.g., the damped rank-reduction method (Chen et al., 2016b), which performs quite well for reflection data. The rank-reduction codes used in this work are modified from the open-source Matlab code package (Chen et al., 2016a). The compared results are given in two 3-D datasets discussed below.

3.3.1. Applications to a simple 3-D synthetic data

I first use a simple 3-D model to generate prestack synthetic seismic data which are close to the benchmark 3-D data used in many published interpolation works (e.g., Trad, 2009; Oropeza and Sacchi, 2011; Chen et al., 2016a,b). In addition I consider a spherical diffractor in the model since most recently published 5-D interpolation results mainly focus on data dominated by reflections (e.g., Trad, 2009; Chopra and Marfurt, 2013; Kreimer et al., 2013; Gao et al., 2015; Ely et al., 2015; Chen et al., 2016b). Diffraction is more and more gaining interest in both academic and industry applications since it images small-scale heterogeneities and structures, e.g. fractures, pinch-outs, thin lenses etc. (e.g., Dell and Gajewski, 2011a,b; Rad et al., 2015). Preserving diffractions (i.e fractures) in 5-D interpolation is a discussed topic and leaves space for discussions and investigations (Trad, 2014).

The simple 3-D model is separated by three layers with the velocity of 1500 m/s, 1800 m/s and 2000 m/s, respectively. A spherical diffractor with a velocity of 4000 m/s and with a lateral extension of 100 m is buried in the bottom layer. In the forward modeling, a zero-phase Ricker-wavelet with a prevailing frequency of 20 Hz is applied. The 3-D synthetic prestack seismic data has a CMP spacing of 12.5 m in the x direction, and 25 m in the y direction. The maximum CMP fold is 20, and the sampling interval is 4 ms. I add 20% random noise to the data, i.e., the maximum RMS amplitude of the signal is 5 times than that of the random noise. In the reduced data set, 50% traces is randomly removed. In the 3-D CRS wavefront attribute search, the midpoint aperture is set to 75 m in the x direction and 50 m in the y direction. The 3-D CRS offset aperture and 3-D partial CRS offset aperture are estimated by the user given in **Appendix A**.

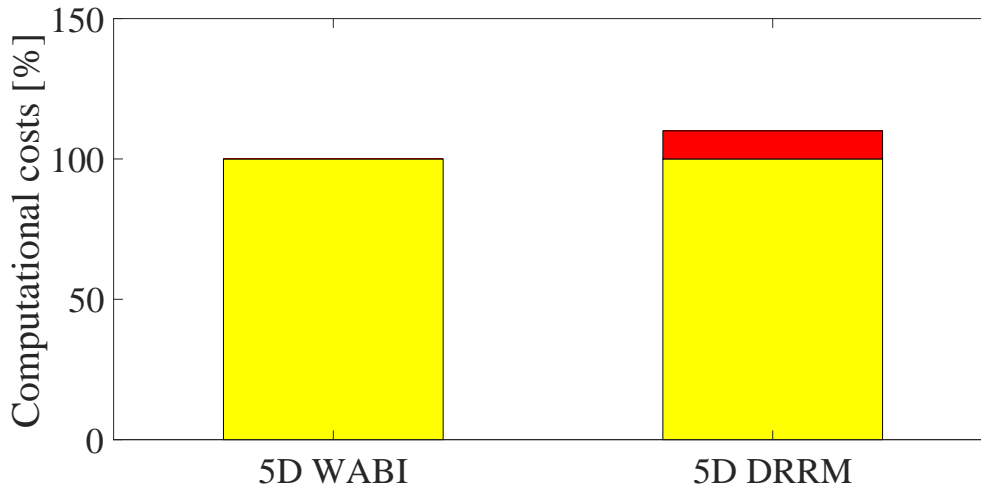


Figure 3.15.: Computational costs of the 5-D WABI method and the 5-D DRRM method, where the 5-D WABI is referenced as 100%. I mention that the computational costs of the 5-D WABI tested here include a global determination of the wavefront attributes by the DE algorithm.

In the following, I will compare the two interpolation methods with respect to computational efficiency and image quality for reflections and diffractions. Figure 3.15 shows the computational costs between the two 5-D interpolation methods tested from the simple 3-D data, which indicates that the damped rank-reduction method has the same magnitude of computational costs compared with the 5-D WABI method when the same computational setting is used, e.g., the same number of CPUs. The comparison may be slightly different with different implementations or different parameter setting, but it indicates that both methods could be comparable in the computational costs. The parameter setting is crucial in the damped rank-reduction method which needs some testing for the data under consideration. I use rank $K = 3$, which is a parameter accounting for the reconstructed events. The damping factor N is set to 2. The greater the N , the weaker is the damping, i.e., a higher S/N data output corresponds to a smaller N . The number of iterations for each frequency slice is set to 10. The minimum and maximum frequency to reconstruct are between 0 Hz and 200 Hz. These parameters are tested from the data. For these tests, the Hankel matrix and the three block Hankel matrices are set close to square matrices. For a detailed discussion on parameters one can refer to the paper (Chen et al., 2016b). In order to show the 5-D interpolation results in 2-D planes, I first extract a 3-D CO volume, e.g., setting the constant half offset $\mathbf{h} = (25 \text{ m}, 0 \text{ m})$, from the 5-D interpolated results, then the 3-D CO volume is cut into two sections (inline 10 and crossline 100) and two time slices (1.66 s and 2.4 s). The two time slices are used to show the reflection (1.66 s) and the bottom diffraction (2.4 s). The color bar of all figures shown below is the amplitude after

the interpolation.

Figure 3.16 shows inline 10 of the 3-D CO volume. I note that the damped rank-reduction method displays reflections slightly stronger, while the 5-D WABI method is superior for diffractions. In the top part with reflection-only data, the damped rank-reduction method reconstructs the reflection to the boundary even if the reflection terminates prior to the boundary (see the left-hand white arrows). In the bottom part of the data, the diffraction pattern is recovered quite well with the 5-D WABI method. The damped rank-reduction method preserves only parts of the diffraction. Figure 3.17 is the crossline 100 of the 3-D CO volume, where both interpolation methods are comparable when the crossline is cut at the center of the salt body, i.e., closer to the spherical diffractor. Figure 3.18 displays the time slice at 1.66 s cutting through the second reflector. Here the damped rank-reduction method shows a better performance than the 5-D WABI to reconstruct the reflection. In the bottom part at time slice 2.4 s which cuts through the diffraction pattern, the 5-D WABI is considerably better in preserving the diffraction when compared with the damped rank-reduction method (see Figure 3.19).

For a more detailed investigation of the damped rank-reduction method on diffraction-only data, the bottom part of the whole 3-D data is used. The comparison is shown in Figure 3.20. In this comparison I see that the damped rank-reduction method can recover parts of the diffraction but still fail to preserve the diffraction tails. If the frequency component of the random noise is close to that of the weak diffraction tails, we may have a challenge to predict or reconstruct the diffraction tails in the frequency domain without a data enhancement facility which is included in the 5-D WABI procedure. Perhaps I need to design adaptive sizes for the Hankel matrix and for the three block Hankel matrices to account for the diffraction in the future.

3.3.2. Applications to the open 3-D SEG C3WA data

In this section, I apply the two 5-D interpolation methods to the open 3-D SEG data, with $S/N = 5$, and 50% traces randomly removed in the data. I use $K = 15$, $N = 6$, and 10 iterations in the damped rank-reduction method. The minimum and maximum reconstructed frequencies are set between 0 Hz to 250 Hz. These parameters are also tested from the 3-D SEG data, in which I get almost the same result if the maximum reconstructed frequency is set larger than 50 Hz. The 3-D CRS apertures and the 3-D partial CRS apertures used here are set as the same as in Chapter 3.2.

Figure 3.21 shows inline 190 of a 3-D volume that is extracted from the 5-D interpolated result with a constant half offset of (0 m, 20 m). I note that the damped

rank-reduction method is strong to reconstruct the reflection events, but weak to preserve the diffraction events by the salt body in the middle of the model. The 5-D WABI is strong in preserving the diffraction patterns including the weak multiple diffractions, compared to the damped rank-reduction method. Similar conclusions are obtained for crossline 300 shown in Figure 3.22. In the time slice at 1.2 s shown in Figure 3.23, the damped rank-reduction method performs well to reconstruct the strong reflections, but fails to preserve the diffraction events caused by edgy structures, while the 5-D WABI keeps both, the reflection and the diffraction, which are recovered very well when compared with the original data.

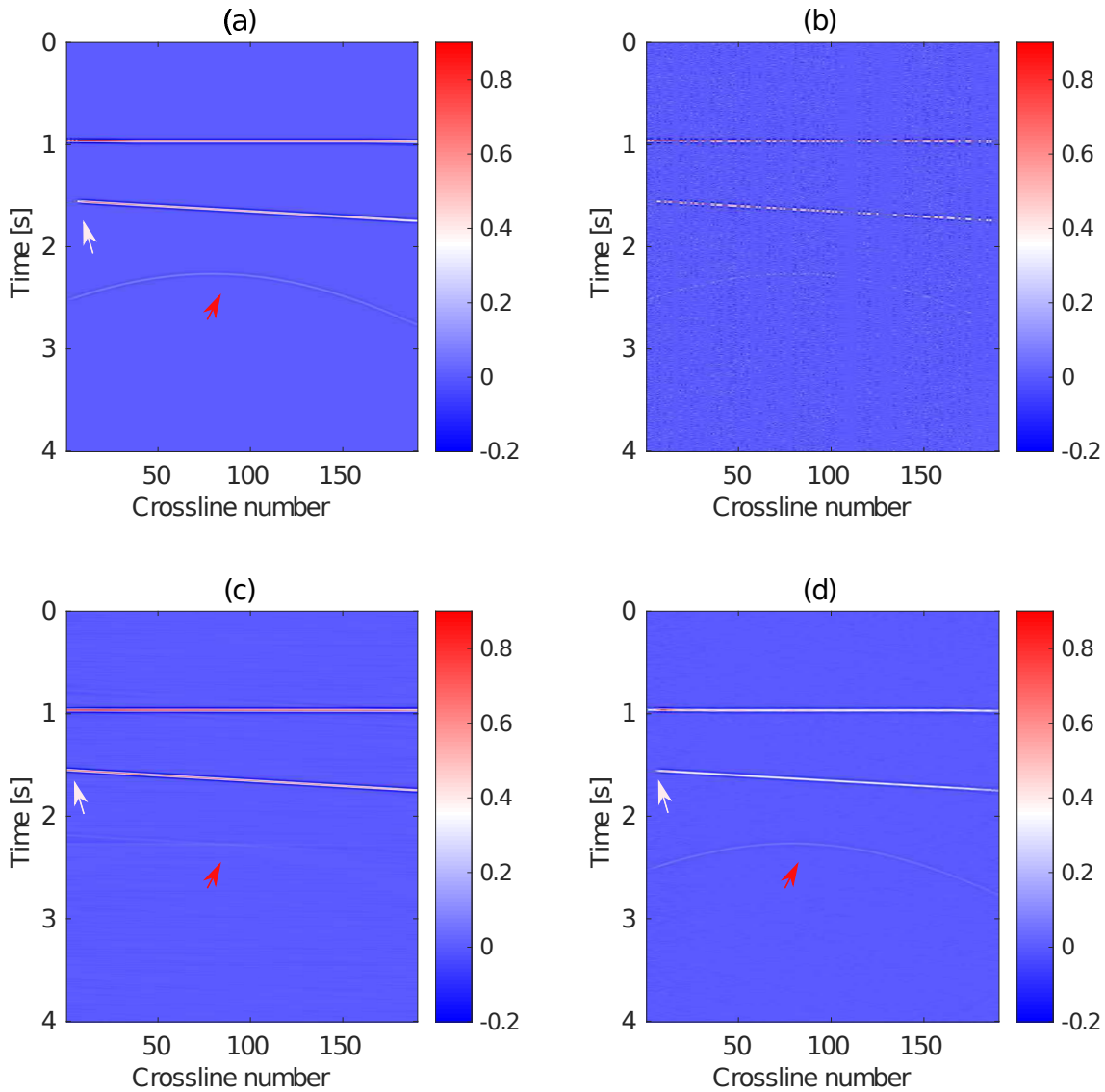


Figure 3.16.: Inline 10 of the 3-D CO volume ($h_x = 25$ m, $h_y = 0$ m). (a) Original data section. (b) Reduced section after adding 20% random noise and killing 50% traces randomly. (c) Denoising and data reconstruction with the damped rank-reduction method. (d) Denoising and data reconstruction with the 5-D WABI method.

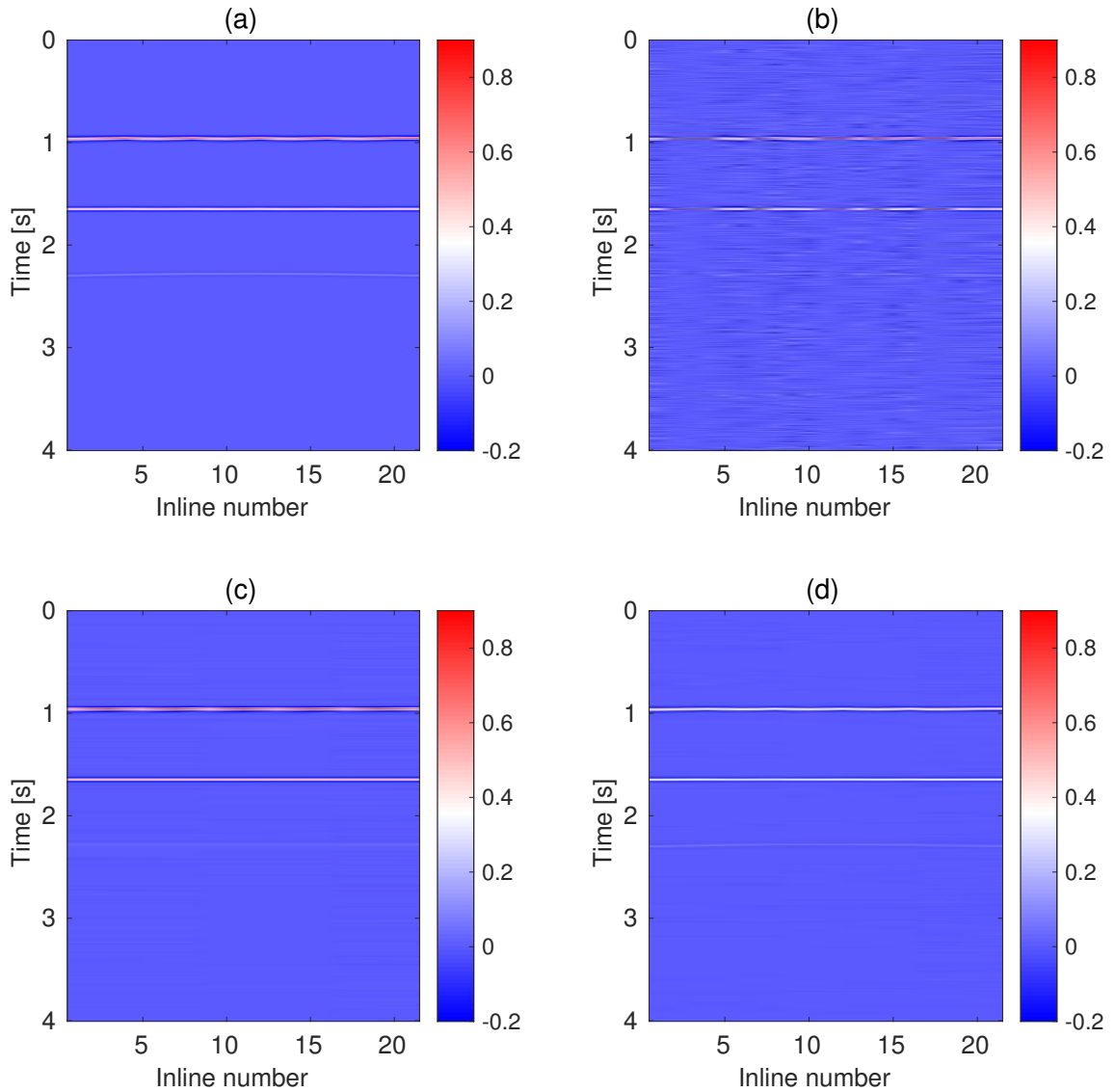


Figure 3.17.: Crossline 100 of the 3-D CO volume ($h_x = 25$ m, $h_y = 0$ m). (a) Original data. (b) Reduced section after adding 20% random noise and killing 50% traces randomly. (c) Denoising and data reconstruction with the damped rank-reduction method. (d) Denoising and data reconstruction with the 5-D WABI method.

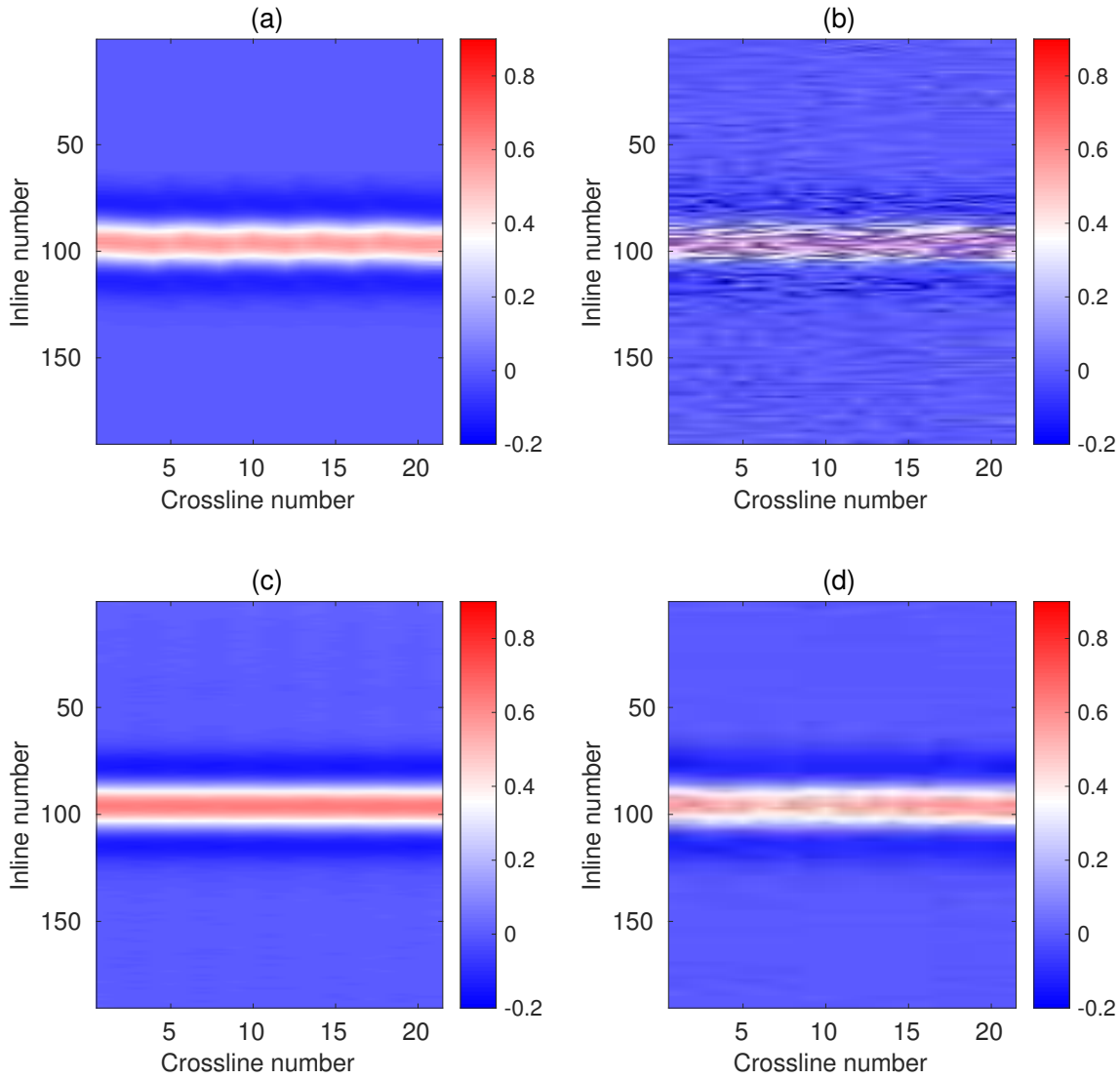


Figure 3.18.: Time slice 1.66 s of the 3-D CO volume ($h_x = 25$ m, $h_y = 0$ m). (a) Original data section. (b) Reduced section after adding 20% random noise and killing 50% traces randomly. (c) Denoising and data reconstruction with the damped rank-reduction method. (d) Denoising and data reconstruction with the 5-D WABI method.

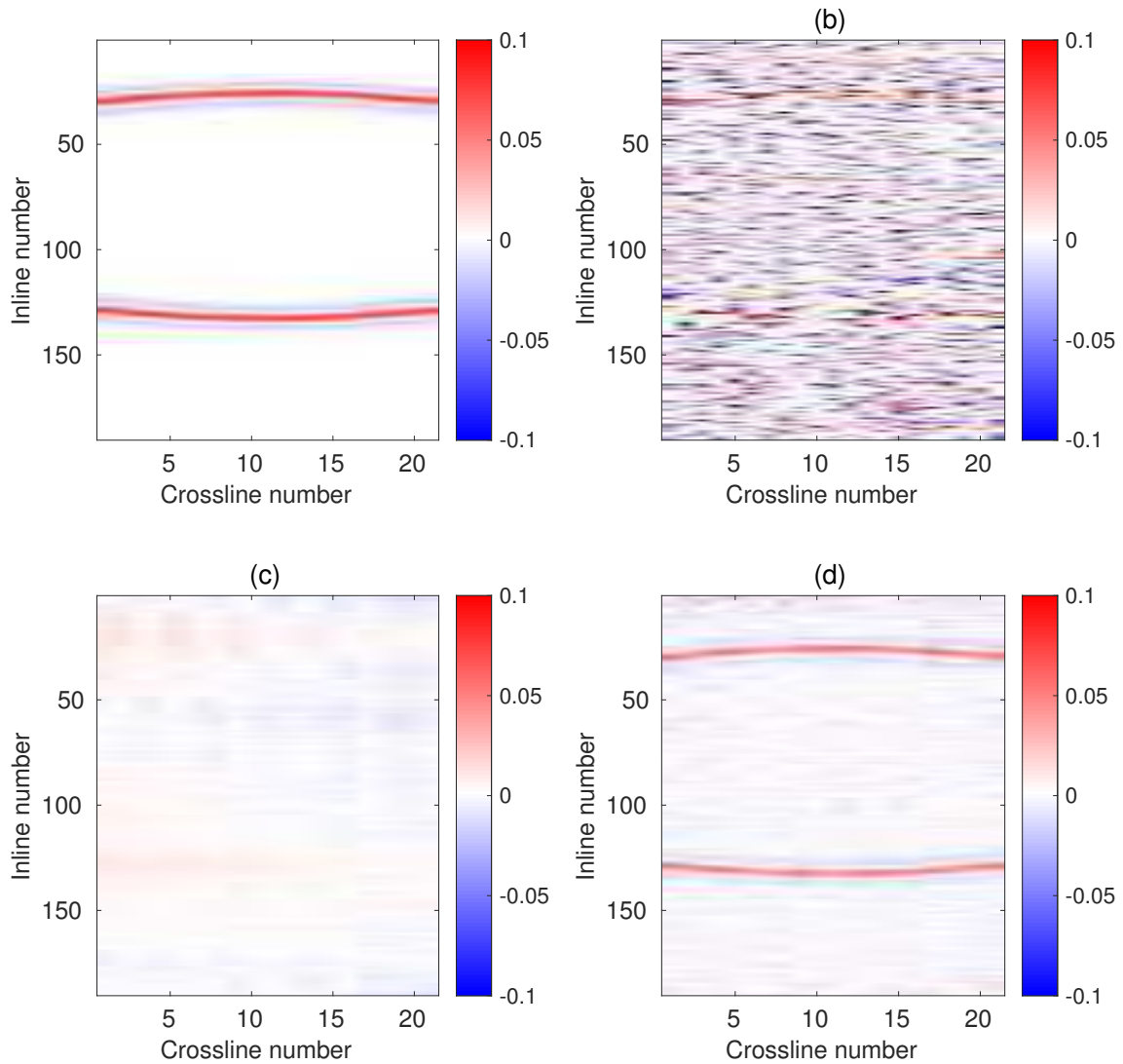


Figure 3.19.: Time slice 2.4 s of the 3-D CO volume ($h_x = 25$ m, $h_y = 0$ m). (a) Original data section. (b) Reduced section after adding 20% random noise and killing 50% traces randomly. (c) Denoising and data reconstruction with the damped rank-reduction method. (d) Denoising and data reconstruction with the 5-D WABI method.

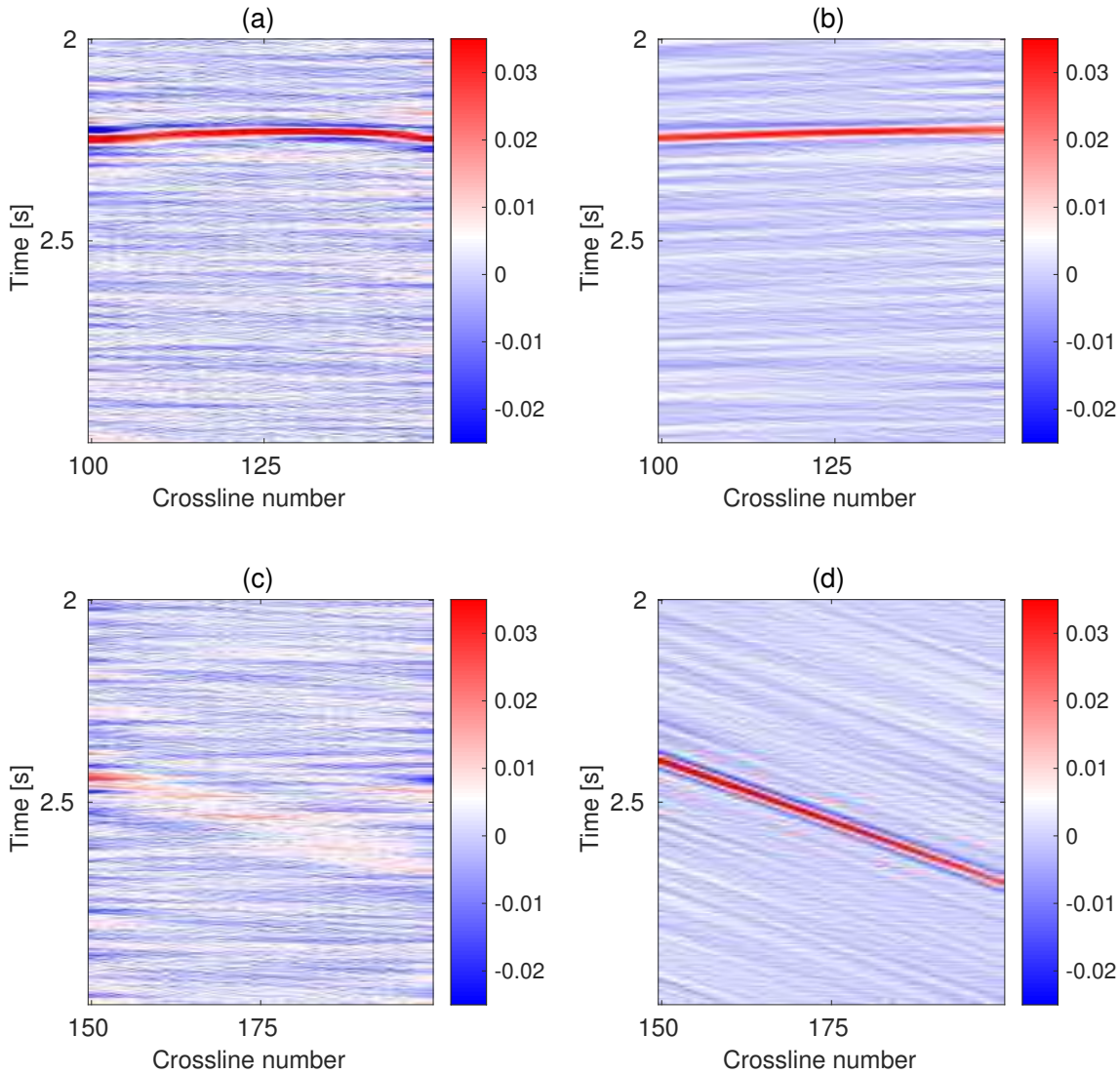


Figure 3.20.: 5-D interpolation results with the diffraction-only data, i.e., the bottom part of the 3-D CO volume ($h_x = 25$ m, $h_y = 0$ m). The top two columns are selected from the central part of the diffraction-only data, where (a) is gotten from the damped rank-reduction method and (b) is obtained from the 5-D WABI method. The bottom two columns selected from the right-hand side of the diffraction-only data, where (c) is gotten from the damped rank-reduction method and (d) is obtained by the 5-D WABI method.

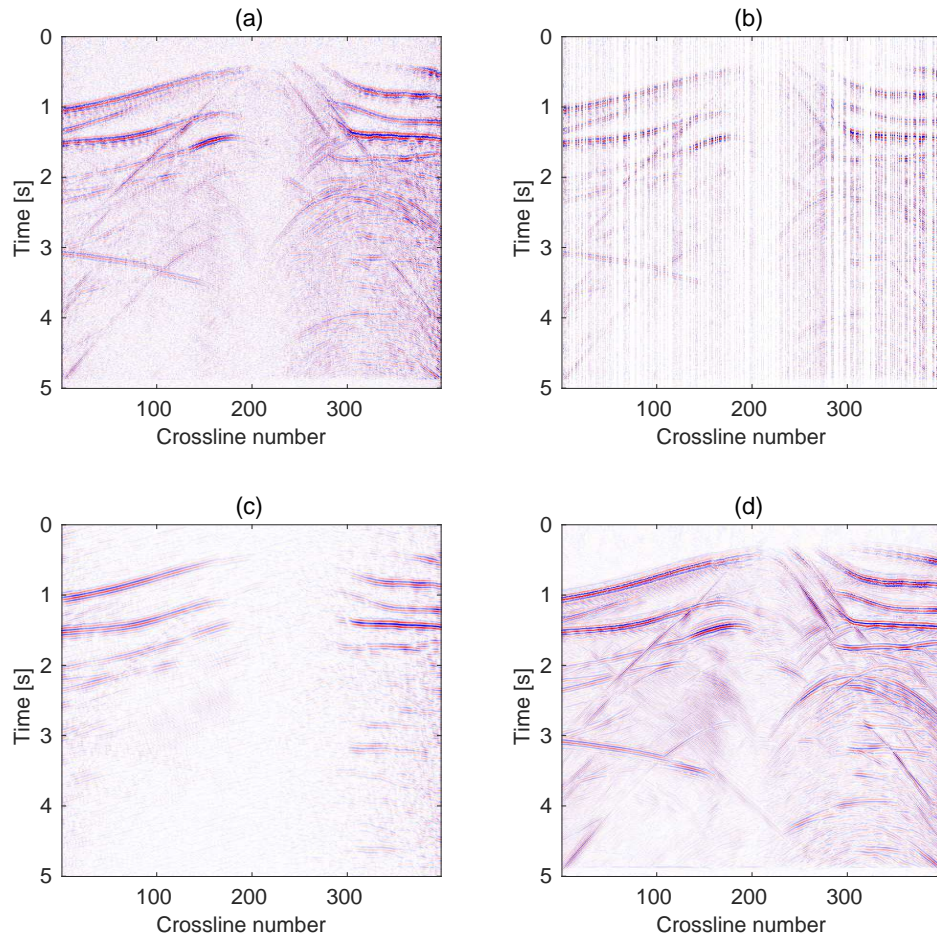


Figure 3.21.: Inline 190 of the 3-D CO volume ($h_x = 0$ m, $h_y = 20$ m). (a) Original data section with 20% random noise. (b) Reduced section with 50% randomly deleted traces. (c) Denoising and data reconstruction with the damped rank-reduction method. (d) Denoising and data reconstruction with the 5-D WABI method. The four subfigures have the same color bar with a minimum (blue) and a maximum (red) amplitude ranged from -0.6 to 0.6.

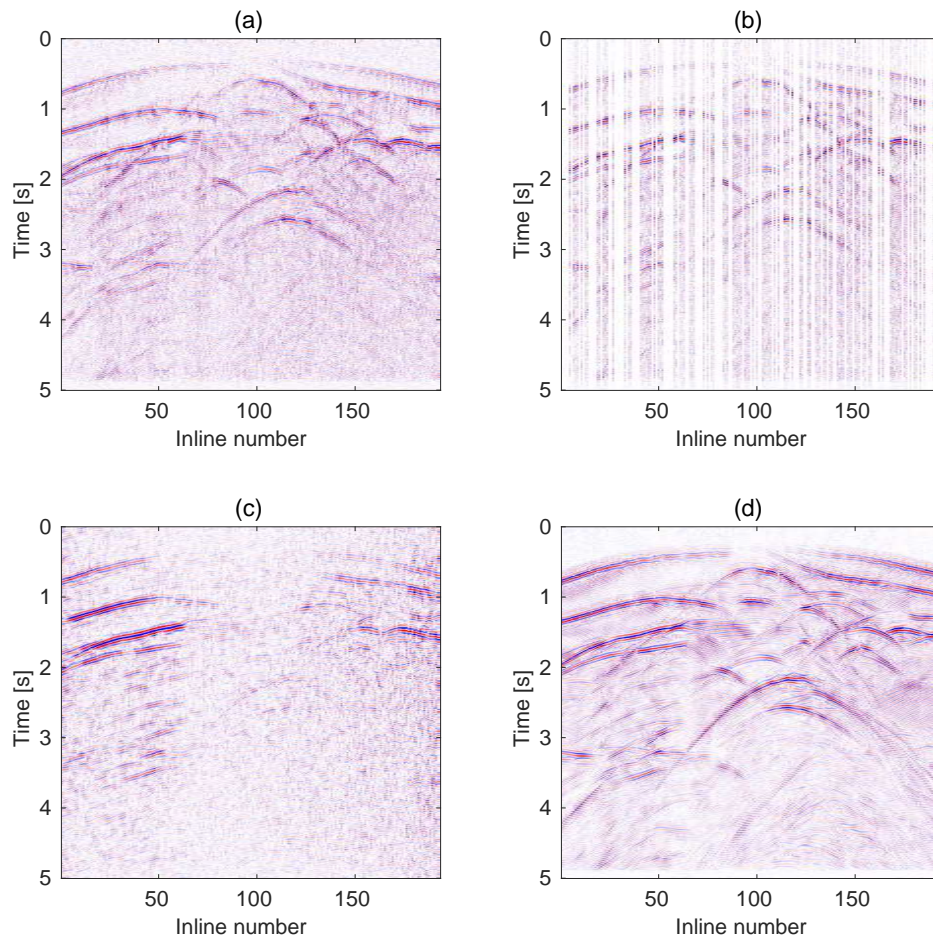


Figure 3.22.: Crossline 300 of the 3-D CO volume ($h_x = 0$ m, $h_y = 20$ m). (a) Original data section with 20% random noise. (b) Reduced section with 50% randomly deleted traces. (c) Denoising and data reconstruction with the damped rank-reduction method. (d) Denoising and data reconstruction with the 5-D WABI method. The four subfigures have the same color bar with a minimum (blue) and a maximum (red) amplitude ranged from -0.6 to 0.6.

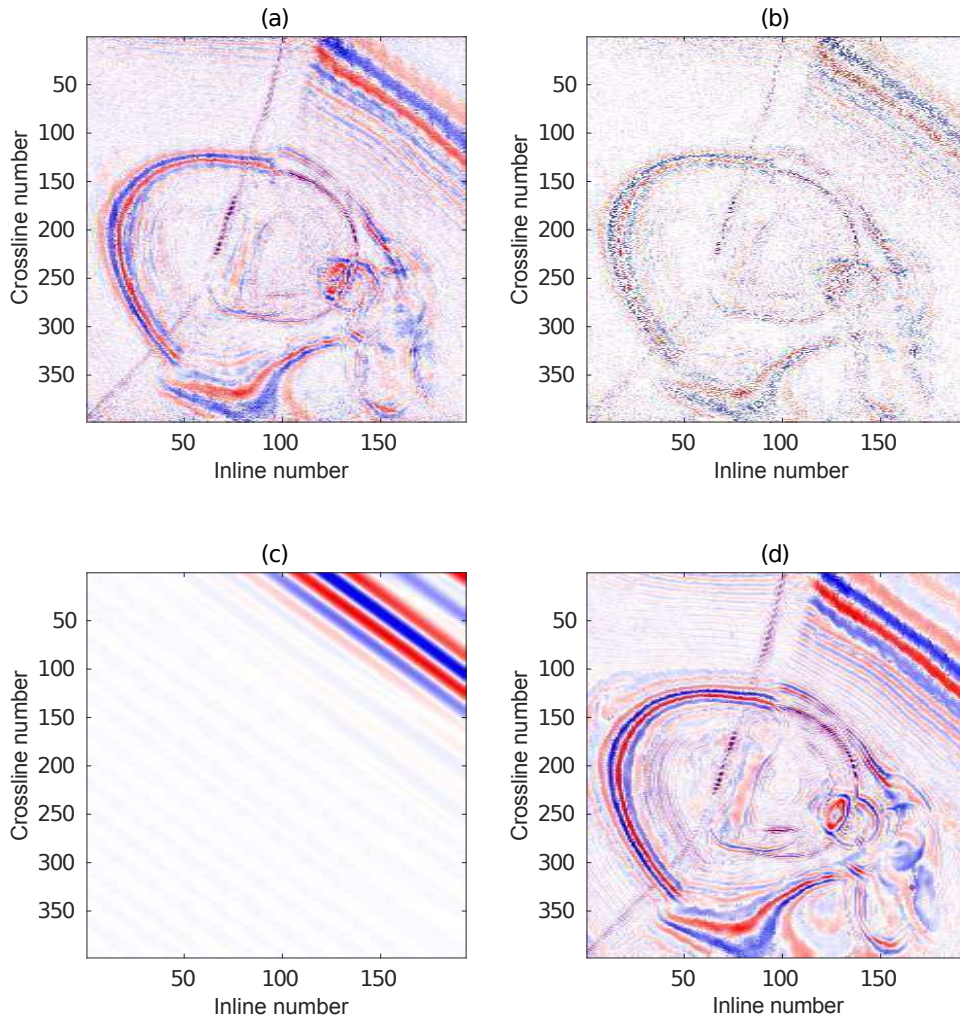


Figure 3.23.: Time slice of 1.2 s of the 3-D CO volume ($h_x = 0$ m, $h_y = 20$ m). (a) Original data section with 20% random noise. (b) Reduced section with 50% randomly deleted traces. (c) Denoising and data reconstruction with the damped rank-reduction method. (d) Denoising and data reconstruction with the 5-D WABI method. The four subfigures have the same color bar with a minimum (blue) and a maximum (red) amplitude ranged from -0.6 to 0.6.

Chapter 4.

Conclusions

Wavefront attributes are useful in seismology and seismic exploration, such as prestack data enhancement, diffraction imaging, and wavefront tomography. In this work, a global determination of the 3-D CRS wavefront attributes is presented, where three global optimization algorithms are introduced for the global search purpose, including the PSO, GA and DE algorithm. By using the open 3-D SEG C3WA data as an example, I found that the semblance and its associated wavefront attributes provided by the GA or by the DE algorithm are better than those semblances and attributes provided by the PSO or by the pragmatic approach. Surprisingly, a global determination of the 3-D CRS wavefront attributes with the GA or the DE algorithm is cheaper than the PSO algorithm and even cheaper than the conventional pragmatic approach, which is challenging my previous understanding that a global search could be computationally expensive. Several parameter tests for the three optimization algorithms showed that, to find the maximum semblance, there are still some challenges to pick suitable parameters for the GA or for the PSO, while for the DE, the optimization process is performed stably and not so sensitive to the parameter setting in the optimization while taking the open 3-D SEG data as an example.

Next to the global optimization, I demonstrate one application with the globally-determined wavefront attributes, which is called 5-D WABI. The 5-D WABI method is an extension of the conventional 3-D partial CRS stacking with the improvement of wavefront attributes and an azimuth-based regularization is applied in each 3-D CMP gather to better account for data with wide-, rich- and full-azimuth acquisition. Results with the open 3-D SEG data indicate that the performance of the 5-D WABI method is better than the conventional 3-D partial CRS stacking. The improvements are particularly visible at far offset traces.

To check the potential usage of the proposed 5-D WABI method, a comparison of the 5-D WABI with the rank-reduction-based 5-D interpolation is given. The comparison indicates that the 5-D WABI method revealed a better performance in the

interpolation process for steeply dipping events like, e.g., diffraction tails. Because of this feature, diffractions are much better preserved by the 5-D WABI than by the rank-reduction-based interpolation. Since diffraction imaging is developing into a powerful add on to plain reflection processing, this feature is substantial for all kind of processing steps utilizing diffractions. Since the wavefront attributes are determined from kinematic properties of the wavefield, namely moveout, aliasing issues are relaxed. The computational effort of the 5-D WABI approach is comparable to the CPU time consumed by the damped rank-reduction method where the comparison includes the CPU time for the determination of wavefront attributes which may be used for several other processing purposes like velocity model building, time and depth migration, diffraction separation and tomography, just to name a few. The 5-D WABI provides a powerful alternative to other 5D interpolation methods with improved handling of diffractions and relaxed aliasing issues. Next to the interpolation capability itself the 5-D WABI process also provides a data enhancement facility.

Chapter 5.

Outlook

For a near 20 years, the 3-D CRS wavefront attributes are generally determined by the conventional pragmatic approach, which works quite well for the classical 3-D CRS stacking. However, today CRS-based works have shifted to the applications with the wavefront attributes, instead of the stacking only. Recent works have reported that lots of processing steps using wavefield attributes benefit of high-quality attributes. Besides, modern computing power allows to determine the wavefront attributes globally in a competitively economic fashion. Both motivate one to globally determine the 3-D CRS wavefront attributes when a 3-D CRS-based work is carried out. Aside from the 5-D interpolation presented in this work, there are still lots of subsequent applications benefit of high-quality wavefront attributes, which will be given in future works. Examples are:

1: 3-D wavefront-based diffraction separation and imaging with global optimization and conflicting dip processing. In previous works, a global determination of the 3-D CRS wavefront attributes and the conflicting dip problem are not considered. With the two considerations together with the 3-D DSR traveltimes operator (e.g., [Abakumov, 2017](#)) or the 3-D non-hyperbolic CRS operator ([Fomel and Kazinnik, 2013](#)), improved diffracted wavefields could be revealed on the stacked volume when compared with the conventional 3-D CRS stacked volume. After subtracting the reflections from the full stacked volume, e.g., by the coherent subtraction method (e.g., [Schwarz and Gajewski, 2017](#)), a diffraction-dominated data can be obtained for the diffraction imaging purpose. The associated results have been reproduced recently, and will be presented soon.

2: 3-D diffraction tomography. With the diffraction-dominated data, e.g., from the above work, together with the 3-D common-diffraction-surface (CDS) operator or the 3-D DSR operator, as well as the kinematic and dynamic ray tracing and the ray perturbation theory, a smooth, laterally inhomogeneous velocity model can be obtained, which would be useful in RTM and FWI, e.g., providing an initial velocity model.

In this work, I only use the 3-D hyperbolic CRS operator to determine the wavefront attributes. Alternative traveltimes operators like the 3-D non-hyperbolic CRS, the 3-D implicit CRS as well as the 3-D DSR traveltimes operators (see [Abakumov, 2017](#)) can be used as well.

Appendices

Appendix A.

Midpoint and offset apertures

3-D CRS midpoint and offset apertures

The midpoint and offset apertures used in the 3-D CRS-based works are crucial for the imaging purpose. In practice, these apertures are often estimated from the data with a data-driven fashion. Figure 3.1a displays the midpoint aperture (red ellipse) used in the interpolation, being initially set to 200 m in both x - and y - direction, i.e., $am_x = am_y = 200$ m. Figure 3.1b shows an offset aperture used in this work. The parameters $h_{x,0}$ and $h_{y,0}$ are the semi-major and semi-minor axes of the top ellipse, where a selection of the location (cutting through a sample) and the size of the top ellipse depends on the data used. In practice, the observed seismic events from the top to the bottom in the offset dimension are initially constrained within the offset aperture, then several candidates for the offset aperture are probed until the one with the best performance is found. The location and size of the bottom ellipse is defined in the same way. In this case, the semi-major and semi-minor axes of an ellipse cutting through a sample on the ZO trace are computed by

$$h_{x,i} = h_{x,0} + i * (h_{x,n} - h_{x,0})/n, \quad (\text{A.1})$$

$$h_{y,i} = h_{y,0} + i * (h_{y,n} - h_{y,0})/n, \quad (\text{A.2})$$

where $h_{x,n}$ and $h_{y,n}$ are the semi-major and semi-minor axes of the bottom ellipse, and n is the maximum number of ZO samples. In the 3-D SEG data, I set $h_{x,0} = 140$ m, $h_{y,0} = 800$ m, $h_{x,n} = 140$ m, $h_{y,n} = 1350$ m. In the simple 3-D data, I use $h_{x,0} = 800$ m, $h_{y,0} = 50$ m, $h_{x,n} = 1000$ m, $h_{y,n} = 50$ m. The 3-D SEG data has a small half offset in the x direction, up to 140 m, and the simple 3-D data has a small half offset in the y direction, up to 50 m.

3-D partial CRS midpoint and offset apertures

The midpoint aperture used in the 3-D partial CRS stack is set as the same as the 3-D CRS stack. The offset aperture used in the 3-D partial CRS stack is determined as:

$$p_{x,i} = b + i * (d - b) / n, \quad (\text{A.3})$$

$$p_{y,i} = a + i * (c - a) / n, \quad (\text{A.4})$$

where a , b , c , and d are estimated by applying several possible apertures and keeping the one with the best image quality. In the 3-D SEG data, I set $a = c = 400$ m, $b = d = 100$ m. So for all samples, I have $p_{x,i} = 100$ m, $p_{y,i} = 400$ m. Similarly, I set $a = c = 50$ m, $b = d = 500$ m for the simple 3-D dataset discussed in the 5-D interpolation part. In this work, I use the same apertures (e.g., midpoint and offset) for both the 3-D partial CRS stack and the 5-D WABI method.

Appendix B.

Pseudocode of several optimization algorithms

Algorithm 1 : Particle Swarm Optimization (PSO) with 3-D CRS approach

- 01: Set the maximum number of *iterations*;
 - 02: Initialize each particle's position (EPP) in the search space;
 - 03: Initialize each particle's best position (EPBP), e.g., EPBP = EPP;
 - 04: Calculate semblance for each particle (a set of wavefront attributes);
 - 05: Calculate the global best position (GBP) based on the best semblance;
 - 06: Update each particle's variation according to Equation (2.14);
 - 07: Update each attribute's position according to Equation (2.15);
 - 08: Update EPBP and GBP if the new position leads to higher semblance;
 - 09: Abort criteria is maximum *iterations* or the semblance tolerance.
-

Algorithm 2 : Genetic Algorithm (GA) with 3-D CRS approach

- 01: set IT , NP , probabilities p_c and p_m for crossover and mutation;
 - 02: initialize each individual \mathbf{P}_i in the user-defined search space;
 - 03: calculate the semblance S_i for each individual \mathbf{P}_i (a set of wavefront attributes);
 - 04: find the global best semblance S_g over each semblance S_i ;
 - 05: store the global best S_g and its coressponding \mathbf{P}_g ; // *i.e.*, keep the best
 - 06: **for** $it = 1$ until IT **do**
 - 07: select new generation based on **Algorithm 3**;
 - 08: call crossover or mutation operator based on p_c and p_m ;
 - 09: calculate new semblance NS_i for each new generated individual \mathbf{X}_i ;
 - 10: find the global best semblance NS_g over each new semblance NS_i ;
 - 11: store the global best semblance NS_g and its coressponding \mathbf{X}_g ;
 - 12: **if** ($NS_g > S_g$) $S_g = NS_g$, $\mathbf{P}_g = \mathbf{X}_g$; // *i.e.*, update the best
 - 13: **end for**
-

Algorithm 3 : Roulette Wheel Selection

```

01: for  $i = 1$  until  $NP$  do
02:   calculate relative fitness:  $RS_i = S_i / (S_1 + S_2 + \dots + S_{NP})$ ;
03:   calculate cumulative fitness:  $CS_i = \sum_{i=1}^{NP} RS_i$ ;
04: end for
05: Randomly generate a real number  $p_s$  between  $[0 \ 1]$ ;
06: for  $i = 1$  until  $NP - 1$  do
07:   if  $(p_s < CS_1)$   $\mathbf{X}_i = \mathbf{X}_1$ ;
08:   if  $(p_s \geq CS_i \ \&\& \ p_s < CS_{i+1})$   $\mathbf{X}_i = \mathbf{X}_{i+1}$ ;
09: end for Note: fitness is the semblance in this work.

```

Algorithm 4 : Differential Evolution (DE) with 3-D CRS approach

```

01: set  $IT$ ,  $NP$ , crossover probability  $CR$  and differential weight  $F$ ;
02: initialize each individual  $\mathbf{P}_i$  in the user-defined search space;
03: calculate the fitness  $S_i$  for each individual  $\mathbf{P}_i$  (a set of wavefront attributes);
04: find the global best fitness  $S_g$  over each fitness  $S_i$ ;
05: store the global best  $S_g$  and its coressponding  $\mathbf{P}_g$ ; // i.e., keep the best
06: for  $it = 1$  until  $IT$  do
07:   for  $i = 1$  until  $NP$  do
08:     pick the three distinct numbers  $r1$ ,  $r2$  and  $r3$ ;
09:     generate an integer  $L$  between  $[1 \ 8]$ ;
10:     for  $j = 1$  until  $8$  do
11:       generate a random value  $p$  between  $[0 \ 1]$ ;
12:       if  $(p < CR$  or  $j = L)$  then
13:          $X_{i,j} = P_{r1,j} + F(P_{r2,j} - P_{r3,j})$ ;
14:       else
15:          $X_{i,j} = P_{i,j}$ ;
16:       end if
17:     end for
18:     calculate new fitness  $NS_i$  for new generated individual  $\mathbf{X}_i$  ( $\mathbf{X}_i = X_{i,j}$ );
19:     if  $(NS_i > S_i)$ 
20:        $S_i = NS_i$ ;
21:        $\mathbf{P}_i = \mathbf{X}_i$ ;
22:     end for
23:   find the global best fitness  $NS_g$  over each new fitness  $NS_i$ ;
24:   store the global best fitness  $NS_g$  and its coressponding  $\mathbf{X}_g$ ;
25:   if  $(NS_g > S_g)$  then // i.e., update the best
26:      $S_g = NS_g$ ;
27:      $\mathbf{P}_g = \mathbf{X}_g$ ;
28:   end if
29: end for

```

Algorithm 5 : Nelder-Mead Simulated Annealing (NMSA) with 3-D CRS approach

01: set nine initial starting vertices ($\mathbf{x}_0, \dots, \mathbf{x}_8$) defining an initial non-degenerated simplex and calculate the semblance values $-f(\mathbf{x}_i)$ of all nine vertices (each vertex vector \mathbf{x}_i corresponding to eight wavefront attributes);

02: set the initial temperature T_0 and a constant temperature steps $tempstep$;

03: set the iteration steps $iter$ at given temperature $T = T_0 - k * (T_0 - 0)/tempstep$, where $k \in \{0, 1, 2, \dots, tempstep\}$;

04: **while** ($k \leq tempstep$) **do**

05: **while** ($j \leq iter$) **do**

06: add a positive and logarithmically distributed random value $T * Random$ to the $-f(\mathbf{x}_i)$, where $i \in \{0, 1, 2, \dots, 8\}$;

07: order according to the semblance values at the vertices: $f(\mathbf{x}_0) \leq f(\mathbf{x}_1) \leq \dots \leq f(\mathbf{x}_8)$;

08: calculate the centroid vector \mathbf{x}_g of all vertices except \mathbf{x}_8 ;

09: calculate *reflected point* $\mathbf{x}_r = \mathbf{x}_g + \alpha(\mathbf{x}_g - \mathbf{x}_8)$, where α being set as 1;

if $f(\mathbf{x}_0) \leq f(\mathbf{x}_r) < f(\mathbf{x}_7)$, reconstruct the simplex by replacing the worst point \mathbf{x}_8 with the reflected point \mathbf{x}_r , and go to step 7;

if $f(\mathbf{x}_r) < f(\mathbf{x}_0)$, expand the *reflected point* to the *expanded point* $\mathbf{x}_e = \mathbf{x}_r + \gamma(\mathbf{x}_r - \mathbf{x}_g)$, where γ being set as 2;

if the $f(\mathbf{x}_e) < f(\mathbf{x}_r)$ reconstruct the simplex by replacing the worst point \mathbf{x}_8 with the expanded point \mathbf{x}_e , and go to step 7;

else $f(\mathbf{x}_e) \geq f(\mathbf{x}_r)$, reconstruct the simplex by replacing the worst point \mathbf{x}_8 with the reflected point \mathbf{x}_r , and go to step 7;

else $f(\mathbf{x}_r) \geq f(\mathbf{x}_7)$, calculate *contracted point* $\mathbf{x}_c = \mathbf{x}_g + \rho(\mathbf{x}_8 - \mathbf{x}_g)$, where $0 < \rho < 0.5$, and being set as 0.5 in this work;

if $f(\mathbf{x}_c) < f(\mathbf{x}_8)$, reconstruct the simplex by replacing the worst point \mathbf{x}_8 with the *contracted point* \mathbf{x}_c , and go to step 7;

else $f(\mathbf{x}_c) \geq f(\mathbf{x}_8)$, replace all vertices except the best by $\mathbf{x}_i = \mathbf{x}_0 + \sigma(\mathbf{x}_i - \mathbf{x}_0)$, where $\sigma = 0.5$, and then go to step 7;

10: compute fractional range tol from the best to the worst point and return if $tol < ftol$, where $ftol$ is defined by the user;

11: save the best point and its corresponding semblance value in this loop;

12: **end while**

13: **end while**

14: save the final best point \mathbf{x}_0 and its corresponding semblance value $-f(\mathbf{x}_0)$ for the given ZO sample;

Note: \mathbf{x}_0 is always the best point, the aim of the above algorithm is to update \mathbf{x}_0 .

Algorithm 6 : Powell Conjugate Direction (PCD) with 3-D CRS approach

```

01: set the maximum number of iterations  $IT$ ;
02: set an initial point and an initial  $8 \times 8$  unit matrix;
03: while  $it \leq IT$  do
04:   while  $i < 8$  do //  $i = 0, 1, 2, \dots, 7$ 
05:     isolate the minimum point of the semblance function in  $i$  direction, and
return its corresponding semblance value;
06:     calculate the largest decreasing direction  $ibig$  during the eight direction;
07:   end while
08:   check the terminal criteria  $it \leq IT$  (or using  $ftol$ );
09:   construct a new direction from the initial point to the minimum point of the
last direction;
10:   calculate an extrapolated point in the new direction, and set the minimum
point of the last direction as the initial point for next  $it$ ;
11:   check the semblance value at the extrapolated point meet the so-called con-
jugate condition (Powell, 1964) or not;
12:   if ( condition is satisfied ) then
13:     set the minimum point of the new direction as the initial point of next  $it$ ;
// i.e., update the initial point at step 9
14:     replace the  $ibig$  direction by the last direction;
15:     set the new direction as the last direction of next  $it$ ; // i.e., introduce a new
direction
16:   else
17:     keep the set of directions for next  $it$ ;
18:   end if
19: end while

```

Appendix C.

Model-driven wavefront attributes

In **Chapter 2** of this work, the wavefront attributes are determined by the 3-D CRS approach with a data-driven fashion. In this section, I will show how to compute the wavefront attributes by kinematic and dynamic ray tracing in the general Cartesian coordinates x_1, x_2, x_3 , where a certain smooth, laterally inhomogeneous background velocity model is needed. Kinematic and dynamic ray tracing are expressed in many forms and in various coordinate systems (see Červený, 2001). Here, a solution to perform the kinematic and dynamic ray tracing in the general Cartesian coordinate system is summarized, where I will explain how the slowness vector and the ray-propagator matrix computed by the kinematic and dynamic ray tracing are connected with the data-driven wavefront attributes.

Kinematic ray tracing is important in forwarding modeling to compute the travel-time, the slowness vector at any point of the reference ray. Generally, the kinematic ray tracing is expressed in the general curvilinear coordinates ξ_1, ξ_2, ξ_3 . However, executing kinematic ray tracing for models in curvilinear coordinates are often complex since the analytical expressions for the scale factors h_1, h_2 , and h_3 in orthogonal coordinates are required. Besides, if the spherical polar coordinates r, θ, ϕ , one of the most used curvilinear coordinates, are given as initial ray coordinates $\gamma_1, \gamma_2, \gamma_3$, the ray tracing may fail in some regions, such as the θ close to 0 or to π (polar regions), or the radius distance r close to 0 (see Červený, 2001). Performing the ray tracing in ray-centered coordinates are common, but parameters used in velocity models are often given in the general Cartesian coordinates and a transformation of them into the ray-centered coordinates or transforming the displacement and slowness of a ray from the ray-centered coordinates to the general Cartesian coordinates is required. As the wavefront attributes determined from, e.g., the 3-D CRS, are derived from the isotropic case. In the follows, I only consider the kinematic and dynamic ray tracing in an inhomogeneous isotropic medium, corresponding relationships for anisotropic media can be found in Červený (2001). In such case, the anisotropic CRS may be required. In the general Cartesian coordinate system for

isotropic medium, the eikonal equation is simplified as

$$\sum_{i=1}^3 (p_i^{(x)})^2 - v^{-2}(x_1, x_2, x_3) = 0, \quad (\text{C.1})$$

where $p_i^{(x)} := \frac{\partial \tau}{\partial x_i}$, $i = 1, 2, 3$, τ is the travelttime along a given ray, and $v(x_1, x_2, x_3)$ is the inhomogeneous background medium velocity. By assuming no turning point with respect to the x_3 direction in the region of interest and eliminating one of the space variables (e.g., x_3) in Equation (C.1), one can get

$$p_3^{(x)} = [v^{-2} - (p_1^{(x)})^2 - (p_2^{(x)})^2]^{1/2} = -\mathcal{H}(x_1, x_2, x_3, p_1^{(x)}, p_2^{(x)}), \quad (\text{C.2})$$

where the function \mathcal{H} is called the reduced Hamiltonian and the associated reduced ray-tracing systems reads as follows:

$$\begin{aligned} \frac{dx_1}{dx_3} &= \frac{\partial \mathcal{H}}{\partial p_1^{(x)}} = \frac{p_1^{(x)}}{p_3^{(x)}}, \\ \frac{dx_2}{dx_3} &= \frac{\partial \mathcal{H}}{\partial p_2^{(x)}} = \frac{p_2^{(x)}}{p_3^{(x)}}, \\ \frac{dp_1^{(x)}}{dx_3} &= -\frac{\partial \mathcal{H}}{\partial x_1} = -\frac{1}{v^3 p_3^{(x)}} \frac{\partial v}{\partial x_1}, \\ \frac{dp_2^{(x)}}{dx_3} &= -\frac{\partial \mathcal{H}}{\partial x_2} = -\frac{1}{v^3 p_3^{(x)}} \frac{\partial v}{\partial x_2}. \end{aligned} \quad (\text{C.3})$$

The travelttime variation along the given ray can be integrated by

$$\frac{d\tau}{dx_3} = \frac{1}{v^2 p_3^{(x)}}. \quad (\text{C.4})$$

In the above, I set $x_i = x_i(u)$ and u is a free monotonic parameter along the ray, not the travelttime or arclength here. If the integration step length dx_3 is set, the dx_1 , dx_2 , $dp_1^{(x)}$, $dp_2^{(x)}$ as well as the $d\tau$ can be computed with the background velocity v . The initial conditions, e.g., the starting location x_i and the slowness vector p_I are taken from results of the 3-D CRS stack. Using the initial conditions with Equation (C.3) and Equation (C.4), the NIP location ($x_i|_{NIP}$) and the two horizontal vectors e_I ($e_I = vp_I$) of the unit vector $\hat{\mathbf{e}}$ defined the up-going normal ray direction can be computed. Again to use Equation (C.3) and (C.4), the travelttime and the slowness vector of the reference ray emerged at the surface can be integrated with the increment of dx_3 , where the slowness vector p_I equals to the vector \mathbf{p} in Equation (2.9). Alternative kinematic ray tracing without reduced Hamiltonian, e.g., considering turning points, is given in (Červený, 2001), where the formulas are different but

the basic ideas are the same, see section 3.3.1 of the seismic ray theory (Červený, 2001). There are several advantages to use reduced Hamiltonian. The first one is that the differential equations used in the kinematic ray tracing are reduced from seven to five. The second is that derivatives of velocity are only required in the x - and y -directions which significantly increases the computational efficiency in the 3-D case. Besides, "turning normal rays rarely occur in practice (in fact, most depth migration algorithms do not handle turning wave energy). If they do occur, they can be easily excluded during the inversion process" (see Duvneck, 2004).

Dynamic ray tracing (expressed in ray coordinate system) also known as paraxial ray tracing (expressed in ray-centered coordinate system) which involves to calculate the 4×4 ray propagator matrix $\mathbf{\Pi}^{(x)}$ or the wavefront curvature matrix ($\mathbf{K}_{CS}^{(x)} = \mathbf{G}\mathbf{K}_{CS}^{(q)}\mathbf{G}^T$) of a ray in the general Cartesian coordinate system, where the subscript CS means common shot. In the follows, the associated reduced Hamiltonian is applied. Performing dynamic ray tracing in the general Cartesian coordinate system without reduced Hamiltonian is given in section 4.7.1 of the seismic ray theory (Červený, 2001). If one notes $\mathbf{w} = (x_1, x_2, p_1^{(x)}, p_2^{(x)})^T$ and $\Delta\mathbf{w} = (\Delta x_1, \Delta x_2, \Delta p_1^{(x)}, \Delta p_2^{(x)})^T$, the dynamic ray tracing system in the general Cartesian coordinate system can be written as

$$\frac{d}{dx_3}\Delta\mathbf{w} = \underline{\mathbf{S}}\Delta\mathbf{w} \quad (\text{C.5})$$

where the $\underline{\mathbf{S}}$ is a 4×4 matrix with

$$\underline{\mathbf{S}} = \begin{pmatrix} \frac{\partial^2 \mathcal{H}}{\partial p_x^{(x)} \partial x} & \frac{\partial^2 \mathcal{H}}{\partial p_x^{(x)} \partial y} & \frac{\partial^2 \mathcal{H}}{\partial p_x^{(x)} \partial p_x^{(x)}} & \frac{\partial^2 \mathcal{H}}{\partial p_x^{(x)} \partial p_y^{(x)}} \\ \frac{\partial^2 \mathcal{H}}{\partial p_y^{(x)} \partial x} & \frac{\partial^2 \mathcal{H}}{\partial p_y^{(x)} \partial y} & \frac{\partial^2 \mathcal{H}}{\partial p_y^{(x)} \partial p_x^{(x)}} & \frac{\partial^2 \mathcal{H}}{\partial p_y^{(x)} \partial p_y^{(x)}} \\ -\frac{\partial^2 \mathcal{H}}{\partial x \partial x} & -\frac{\partial^2 \mathcal{H}}{\partial x \partial y} & -\frac{\partial^2 \mathcal{H}}{\partial x \partial p_x^{(x)}} & -\frac{\partial^2 \mathcal{H}}{\partial x \partial p_y^{(x)}} \\ -\frac{\partial^2 \mathcal{H}}{\partial y \partial x} & -\frac{\partial^2 \mathcal{H}}{\partial y \partial y} & -\frac{\partial^2 \mathcal{H}}{\partial y \partial p_x^{(x)}} & -\frac{\partial^2 \mathcal{H}}{\partial y \partial p_y^{(x)}} \end{pmatrix} \quad (\text{C.6})$$

Each element of $\underline{\mathbf{S}}$ can be calculated as follows by using Equation (C.2).

$$\begin{aligned}
\frac{\partial^2 \mathcal{H}}{\partial p_x^{(x)} \partial x} &= \frac{p_1^{(x)}}{v^3 (p_3^{(x)})^3} \frac{\partial v}{\partial x_1}, & \frac{\partial^2 \mathcal{H}}{\partial p_x \partial y} &= \frac{p_1^{(x)}}{v^3 (p_3^{(x)})^3} \frac{\partial v}{\partial x_2}, \\
\frac{\partial^2 \mathcal{H}}{\partial p_x^{(x)} \partial p_x^{(x)}} &= \frac{(p_1^{(x)})^2}{(p_x^{(x)})^3} + \frac{1}{p_3^{(x)}}, & \frac{\partial^2 \mathcal{H}}{\partial p_x \partial p_y} &= \frac{p_1^{(x)} p_2^{(x)}}{(p_3^{(x)})^3}, \\
\frac{\partial^2 \mathcal{H}}{\partial p_y^{(x)} \partial x} &= \frac{p_2^{(x)}}{v^3 (p_3^{(x)})^3} \frac{\partial v}{\partial x_1}, & \frac{\partial^2 \mathcal{H}}{\partial p_y \partial y} &= \frac{p_2^{(x)}}{v^3 (p_3^{(x)})^3} \frac{\partial v}{\partial x_2}, \\
\frac{\partial^2 \mathcal{H}}{\partial p_y^{(x)} \partial p_x^{(x)}} &= \frac{p_1^{(x)} p_2^{(x)}}{(p_3^{(x)})^3}, & \frac{\partial^2 \mathcal{H}}{\partial p_y \partial p_y} &= \frac{(p_2^{(x)})^2}{(p_x^{(x)})^3} + \frac{1}{p_3^{(x)}}, \\
-\frac{\partial^2 \mathcal{H}}{\partial x \partial x} &= -\frac{1}{v^4 p_3^{(x)}} \left[v \frac{\partial^2 v}{\partial x_1^2} + \left(\frac{1}{v^2 (p_3^{(x)})^2} \right) \left(\frac{\partial v}{\partial x_1} \right)^2 \right], \\
-\frac{\partial^2 \mathcal{H}}{\partial x \partial y} &= -\frac{1}{v^4 p_3^{(x)}} \left[v \frac{\partial^2 v}{\partial x_1 \partial x_2} + \left(\frac{1}{v^2 (p_3^{(x)})^2} \right) \left(\frac{\partial v}{\partial x_1} \right) \left(\frac{\partial v}{\partial x_2} \right) \right], \\
-\frac{\partial^2 \mathcal{H}}{\partial x \partial p_x^{(x)}} &= -\frac{p_1^{(x)}}{v^3 (p_3^{(x)})^3} \frac{\partial v}{\partial x_1}, & -\frac{\partial^2 \mathcal{H}}{\partial x \partial p_y} &= -\frac{p_2^{(x)}}{v^3 (p_3^{(x)})^3} \frac{\partial v}{\partial x_1}, \\
-\frac{\partial^2 \mathcal{H}}{\partial y \partial x} &= -\frac{1}{v^4 p_3^{(x)}} \left[v \frac{\partial^2 v}{\partial x_1 \partial x_2} + \left(\frac{1}{v^2 (p_3^{(x)})^2} \right) \left(\frac{\partial v}{\partial x_1} \right) \left(\frac{\partial v}{\partial x_2} \right) \right], \\
-\frac{\partial^2 \mathcal{H}}{\partial y \partial y} &= -\frac{1}{v^4 p_3^{(x)}} \left[v \frac{\partial^2 v}{\partial x_1^2} + \left(\frac{1}{v^2 (p_3^{(x)})^2} \right) \left(\frac{\partial v}{\partial x_1} \right)^2 \right], \\
-\frac{\partial^2 \mathcal{H}}{\partial y \partial p_x^{(x)}} &= -\frac{p_1^{(x)}}{v^3 (p_3^{(x)})^3} \frac{\partial v}{\partial x_2}, & -\frac{\partial^2 \mathcal{H}}{\partial y \partial p_y} &= -\frac{p_2^{(x)}}{v^3 (p_3^{(x)})^3} \frac{\partial v}{\partial x_2}.
\end{aligned} \tag{C.7}$$

Equation (C.5) means that the $\Delta \mathbf{w}$ can be computed with dx_3 . The associated ray propagator matrix $\underline{\mathbf{\Pi}}^{(x)}$ is satisfied:

$$\frac{d}{dx_3} \underline{\mathbf{\Pi}}^{(x)} = \underline{\mathbf{S}} \underline{\mathbf{\Pi}}^{(x)}. \tag{C.8}$$

The matrix $\underline{\mathbf{\Pi}}^{(x)}$ is defined as

$$\underline{\mathbf{\Pi}}^{(x)} = \begin{pmatrix} \mathbf{Q}_1^{(x)} & \mathbf{Q}_2^{(x)} \\ \mathbf{P}_1^{(x)} & \mathbf{P}_2^{(x)} \end{pmatrix}. \tag{C.9}$$

The 2×2 matrices $\mathbf{Q}_1^{(x)}$ and $\mathbf{P}_1^{(x)}$ are generally explained as a solution of Equation (C.5) for initial condition of a line source. While $\mathbf{Q}_2^{(x)}$ and $\mathbf{P}_2^{(x)}$ are explained as a solution of Equation (C.5) for initial condition of a point source (see Červený, 2001). Using Equation (C.5) through Equation (C.9), the four matrices $\mathbf{Q}_1^{(x)}$, $\mathbf{Q}_2^{(x)}$,

$\mathbf{P}_2^{(x)}$ and $\mathbf{P}_2^{(x)}$ along the reference ray can be integrated with the increment of dx_3 starting from a shot to a receiver. However, in order to find a connection between $\underline{\mathbf{\Pi}}^{(x)}$ with the wavefront attributes, the relationship between $\underline{\mathbf{\Pi}}^{(x)}$ and $\underline{\mathbf{T}}$ is needed since the submatrices \mathbf{A} , \mathbf{B} , \mathbf{C} , and \mathbf{D} of $\underline{\mathbf{T}}$ are related to the wavefront attributes (see Equation (2.7) and Equation (2.9)). Generally, the $\underline{\mathbf{T}}$ is expressed in a local Cartesian coordinates z_1, z_2, z_3 . It could be referred to as $\underline{\mathbf{T}}^{(z)}$. However, in marine data acquisition, the local Cartesian coordinates system coincides with the general Cartesian coordinate system, and a transformation between them does not need anymore. Hence I set $\underline{\mathbf{T}} = \underline{\mathbf{T}}^{(z)}$, and the $\underline{\mathbf{T}}$ is often used in the seismic systems (e.g., Bortfeld, 1989; Hubral et al., 1992). A relationship between $\underline{\mathbf{\Pi}}^{(q)}$ expressed in ray-centered coordinate system and $\underline{\mathbf{T}}^{(z)}$ is given in Section 4.4.7 of the seismic ray theory (Červený, 2001), where I note $\underline{\mathbf{\Pi}}^{(x)} = \underline{\mathbf{T}}^{(z)} = \underline{\mathbf{T}}$ only if the dynamic ray tracing is performed in the general Cartesian coordinate system and the data is acquired, e.g., from marine environment, in which the shots and receivers are situated near the sea level. One should note that, generally, $\underline{\mathbf{\Pi}}^{(x)} \neq \underline{\mathbf{\Pi}}^{(q)}$, $\underline{\mathbf{\Pi}}^{(q)} \neq \underline{\mathbf{T}}^{(z)}$, and $\underline{\mathbf{T}}^{(z)} \neq \underline{\mathbf{T}}$. Transformation matrices, interface matrices and the velocity distribution around shots and receivers are required. The $\underline{\mathbf{\Pi}}^{(x)} = \underline{\mathbf{T}}$ I use here because: 1) the dynamic ray tracing is performed in the general Cartesian coordinates, no transformation required; 2) the matrix described the inhomogeneity of the medium near the shot and receiver locations vanishes in a constant velocity medium; 3) the interface curvature matrix around the sources and receivers equals to zero. In the case of the normal ray tracks along a ray from the surface $\hat{\mathbf{s}}$ to the underground NIP, one can define the down-going propagator matrix $\underline{\mathbf{T}}_0$ and the up-going propagator matrix $\underline{\mathbf{T}}_0^*$ as:

$$\underline{\mathbf{T}}_0 = \begin{pmatrix} \mathbf{A}_0 & \mathbf{B}_0 \\ \mathbf{C}_0 & \mathbf{D}_0 \end{pmatrix}, \underline{\mathbf{T}}_0^* = \begin{pmatrix} \mathbf{D}_0^T & \mathbf{B}_0^T \\ \mathbf{C}_0^T & \mathbf{A}_0^T \end{pmatrix}. \quad (\text{C.10})$$

Using dynamic ray tracing starting from the NIP up-going to the receivers, each element of the up-going propagator matrix $\underline{\mathbf{T}}_0^*$ of a ray can be obtained. According to the chain rule described a central ray traveling from $\hat{\mathbf{s}}$ to NIP and back to the receiver $\hat{\mathbf{g}}$, one can get

$$\begin{aligned} \mathbf{D}\mathbf{B}^{-1} - \mathbf{B}^{-1} &= \mathbf{D}_0^{-1}\mathbf{C}_0, \\ \mathbf{D}\mathbf{B}^{-1} + \mathbf{B}^{-1} &= \mathbf{B}_0^{-1}\mathbf{A}_0. \end{aligned} \quad (\text{C.11})$$

Hence, with Equation (2.7), following equations can be obtained:

$$\begin{aligned} \mathbf{M}_{mm}^{zo} &= \mathbf{D}_0^{-1}\mathbf{C}_0, \\ \mathbf{M}_{hh}^{zo} &= \mathbf{B}_0^{-1}\mathbf{A}_0. \end{aligned} \quad (\text{C.12})$$

In case of the dynamic ray tracing starting from the NIP up-going to the receivers, with the right part of Equation (C.10), the following equations are derived:

$$\mathbf{A}_0^T(\mathbf{B}_0^T)^{-1} = \mathbf{B}_0^{-1}\mathbf{A}_0 = \mathbf{M}_{CS}^{(x)} = \frac{1}{v}\mathbf{K}_{CS}^{(x)}. \quad (\text{C.13})$$

It is often used in the NIP-wave tomography (e.g., [Duvaneck, 2004](#)), where $\mathbf{M}_{hh}^{zo} = \mathbf{M}_{mm}^{zo} = \mathbf{M}_{CS}^{(x)}$ for the NIP case. The slowness vector p_I related to first derivatives of the traveltime is computed with Equation (C.3) in the kinematic ray tracing system. While the \mathbf{T}_0^* related to second derivatives of the traveltime is calculated in the dynamic ray tracing system, where the relationship between submatrices of \mathbf{T}_0^* and the curvature matrices \mathbf{M}_{hh}^{zo} and \mathbf{M}_{mm}^{zo} is given in Equation (C.12). So far, the relationship between the data-driven wavefront attributes and model-driven wavefront attributes is derived to the normal ray case. A derivation for the non-normal ray case (e.g., the 3-D FO CRS) is similar since we have the wavefront attributes determined by Equation (2.4), and the associated model-driven (forwarded) wavefront attributes can be computed by the two ray tracing systems discussed above.

Appendix D.

Data-driven wavefront attributes

With the open 3-D SEG C3WA data as an example, the eight wavefront attributes can be determined by the 3-D CRS approach with a data-driven fashion. In this section, I only provide the wavefront attributes searched by the pragmatic approach and the DE global optimization, where three sections of the resulted volume are shown. The reader if interesting can ask the **3-D CRS with global optimization** software from the WIT website or from the WIKI pages (applied seismics, Hamburg) to reproduce all of them to see other parts of the attribute volume or try to pick the GA and PSO algorithm to see the differences between them.

The image quality of M_{00} is low (see Figure D.1). This is because the 3D SEG C3WA data has a small half offset (up to 140 m) in the x direction. I do not observe big differences between the pragmatic approach and the DE algorithm in terms of the azimuth and dip sections except the inline 190, where the azimuth and dip attributes provided by the DE algorithm can provide clearer and distinguished events. The **N** wavefront attributes show different color values, where I use 300 m midpoint aperture for both methods in this comparison. In practice for the 3D SEG data, one can use a smaller midpoint aperture, e.g 100 m or 200 m. I suggest to use the DE algorithm for the determination of 3-D wavefront attributes. The GA and PSO algorithm can be used as well, but you may bear more effort to find suitable parameters for the GA or PSO when different datasets are used.

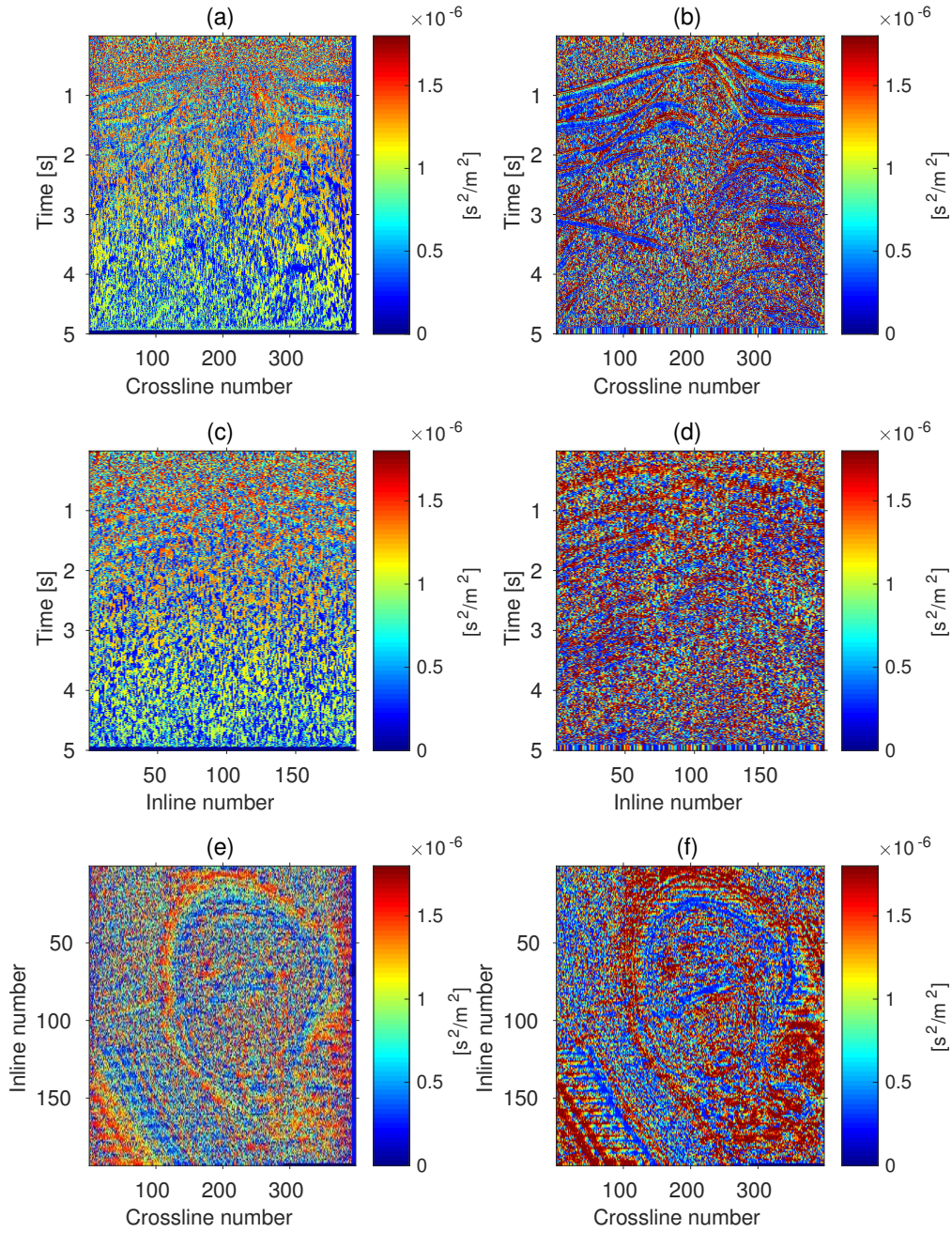


Figure D.1.: M_{00} wavefront attribute. (a) Inline 190 with pragmatic approach. (b) Inline 190 with DE. (c) Crossline 300 with pragmatic approach. (d) Crossline 300 with DE. (e) Time slice 1.2 s with pragmatic approach. (f) Time slice 1.2 s with DE.

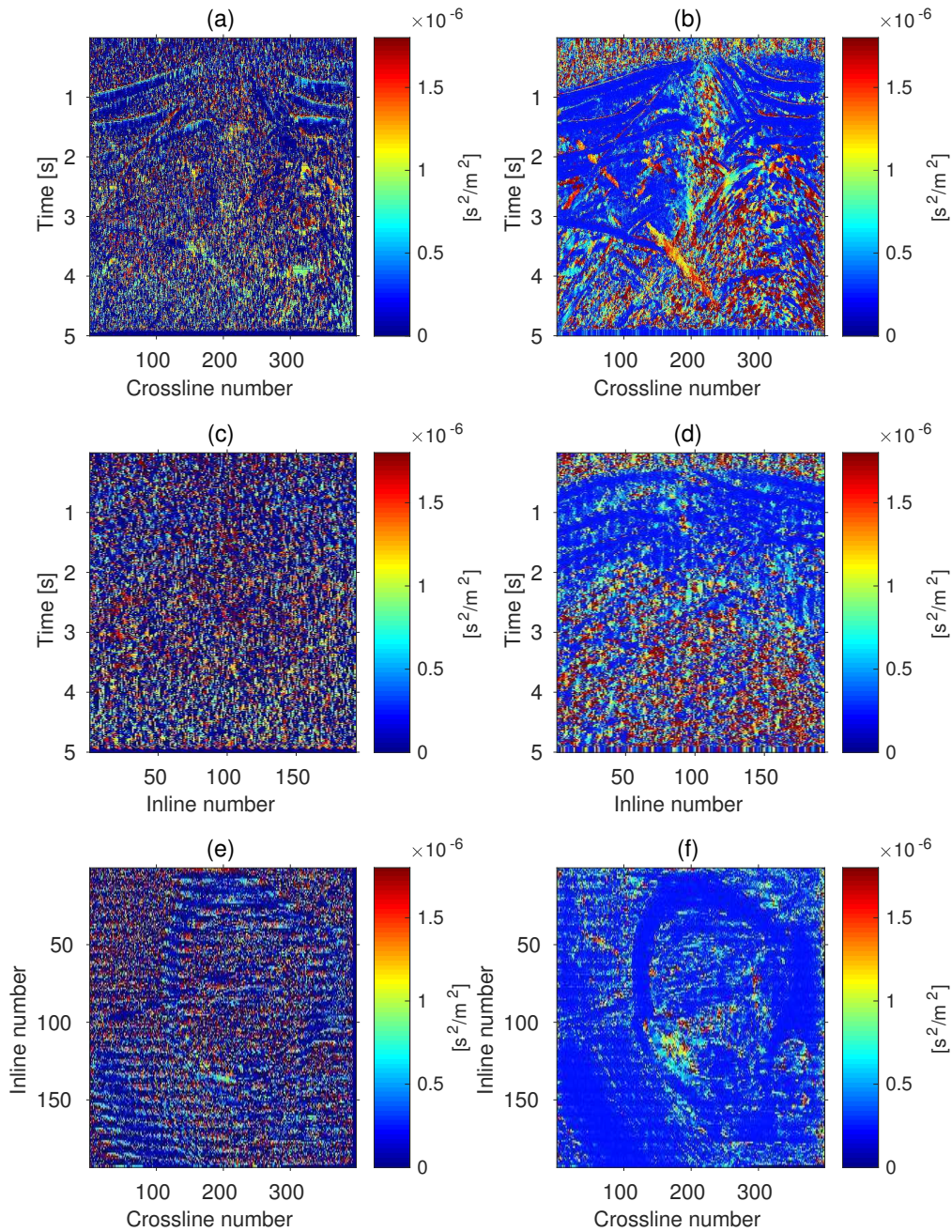


Figure D.2.: M_{10} wavefront attribute. (a) Inline 190 with pragmatic approach. (b) Inline 190 with DE. (c) Crossline 300 with pragmatic approach. (d) Crossline 300 with DE. (e) Time slice 1.2 s with pragmatic approach. (f) Time slice 1.2 s with DE.

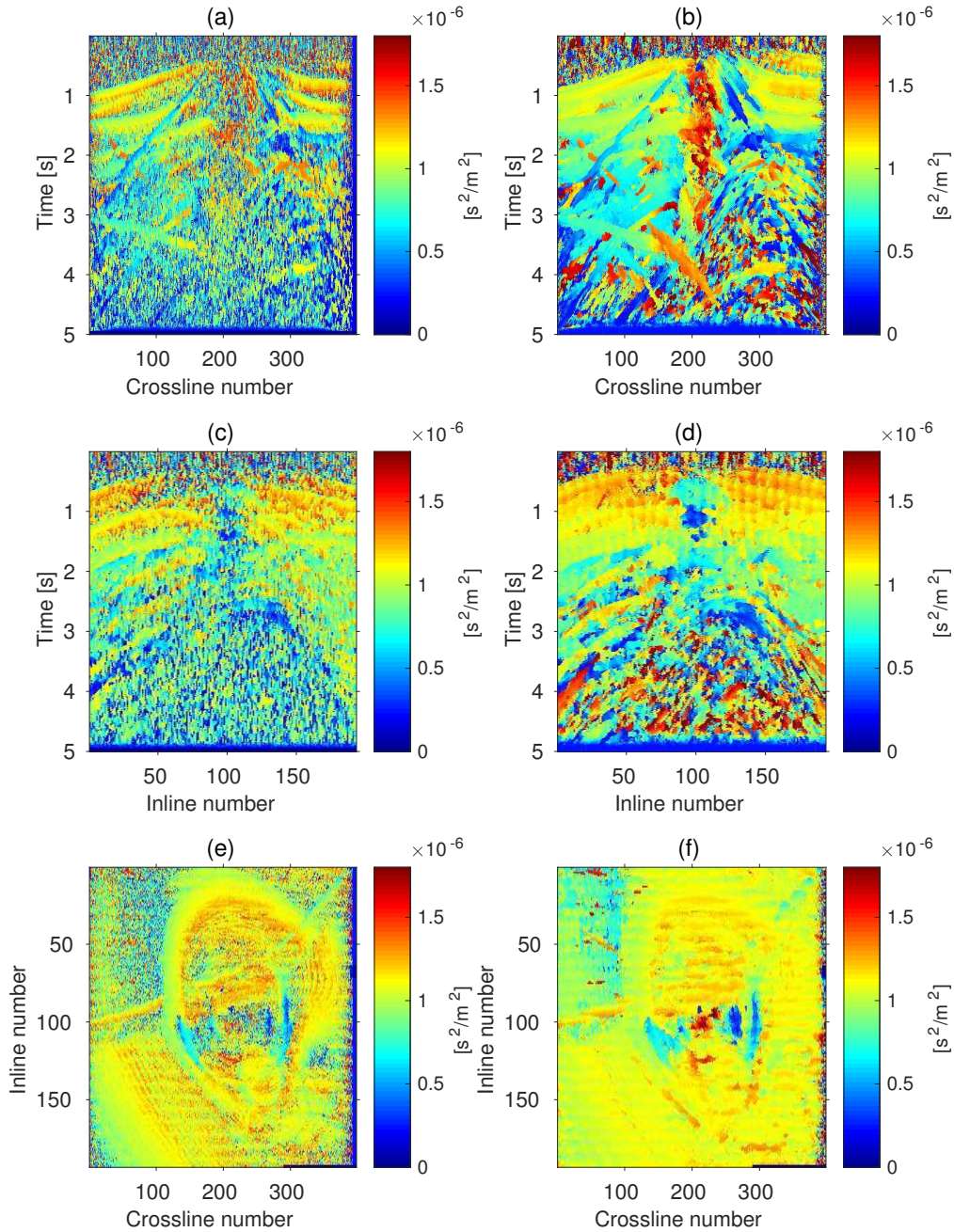


Figure D.3.: M_{11} wavefront attribute. (a) Inline 190 with pragmatic approach. (b) Inline 190 with DE. (c) Crossline 300 with pragmatic approach. (d) Crossline 300 with DE. (e) Time slice 1.2 s with pragmatic approach. (f) Time slice 1.2 s with DE.

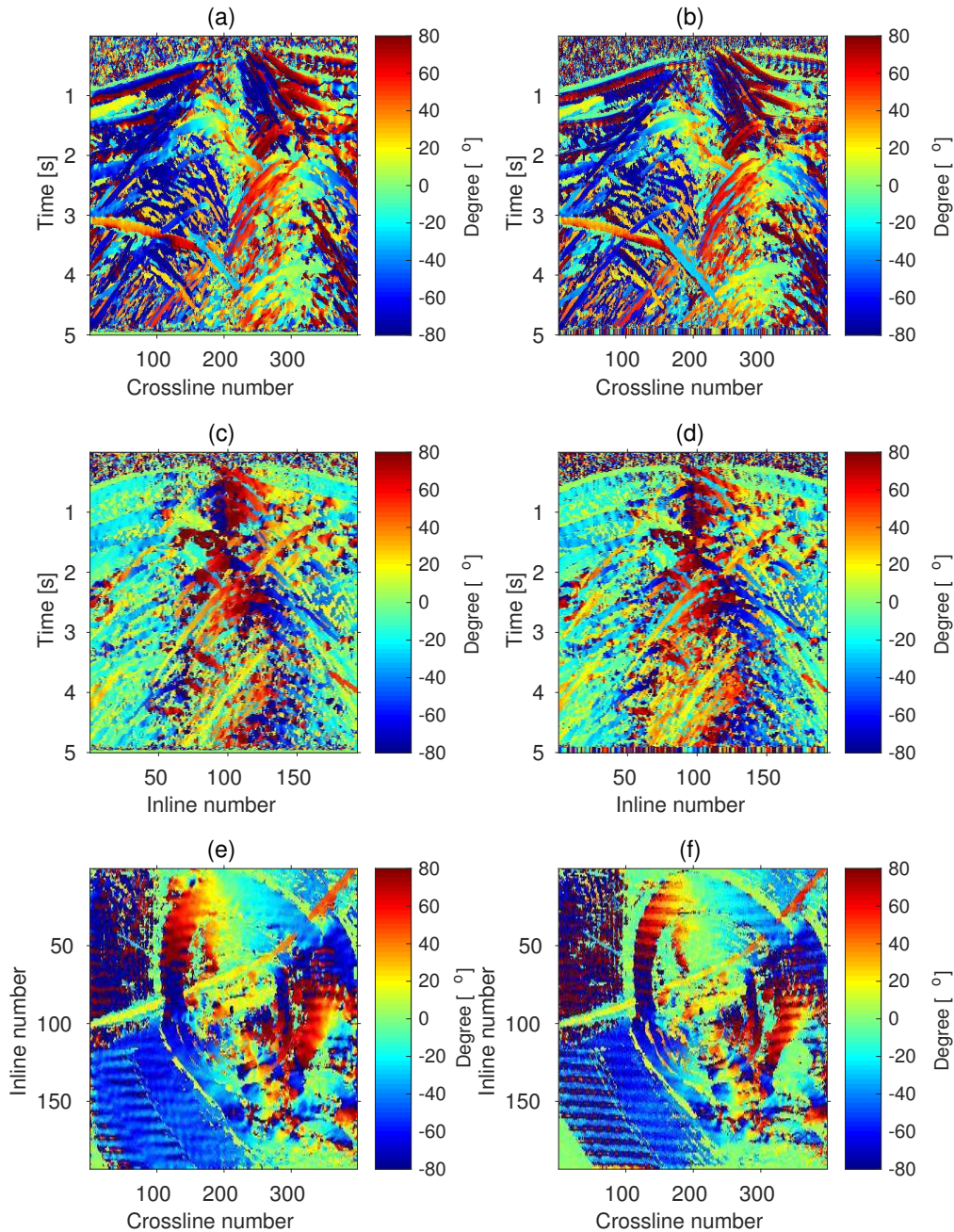


Figure D.4.: Azimuth wavefront attribute. (a) Inline 190 with pragmatic approach. (b) Inline 190 with DE. (c) Crossline 300 with pragmatic approach. (d) Crossline 300 with DE. (e) Time slice 1.2 s with pragmatic approach. (f) Time slice 1.2 s with DE. In this test, I constrain the azimuth search range between $[-80^\circ$ to $80^\circ]$. However, to better use the 3-D SEG C3WA data, one would be better to set the azimuth range between $[-180^\circ$ $0^\circ]$ or $[180^\circ$ $360^\circ]$. Even more, the semblance would be kept almost the same when setting the azimuth to $\pi/2$, $-\pi/2$, or $3\pi/2$, seeing the data acquisition geometry.

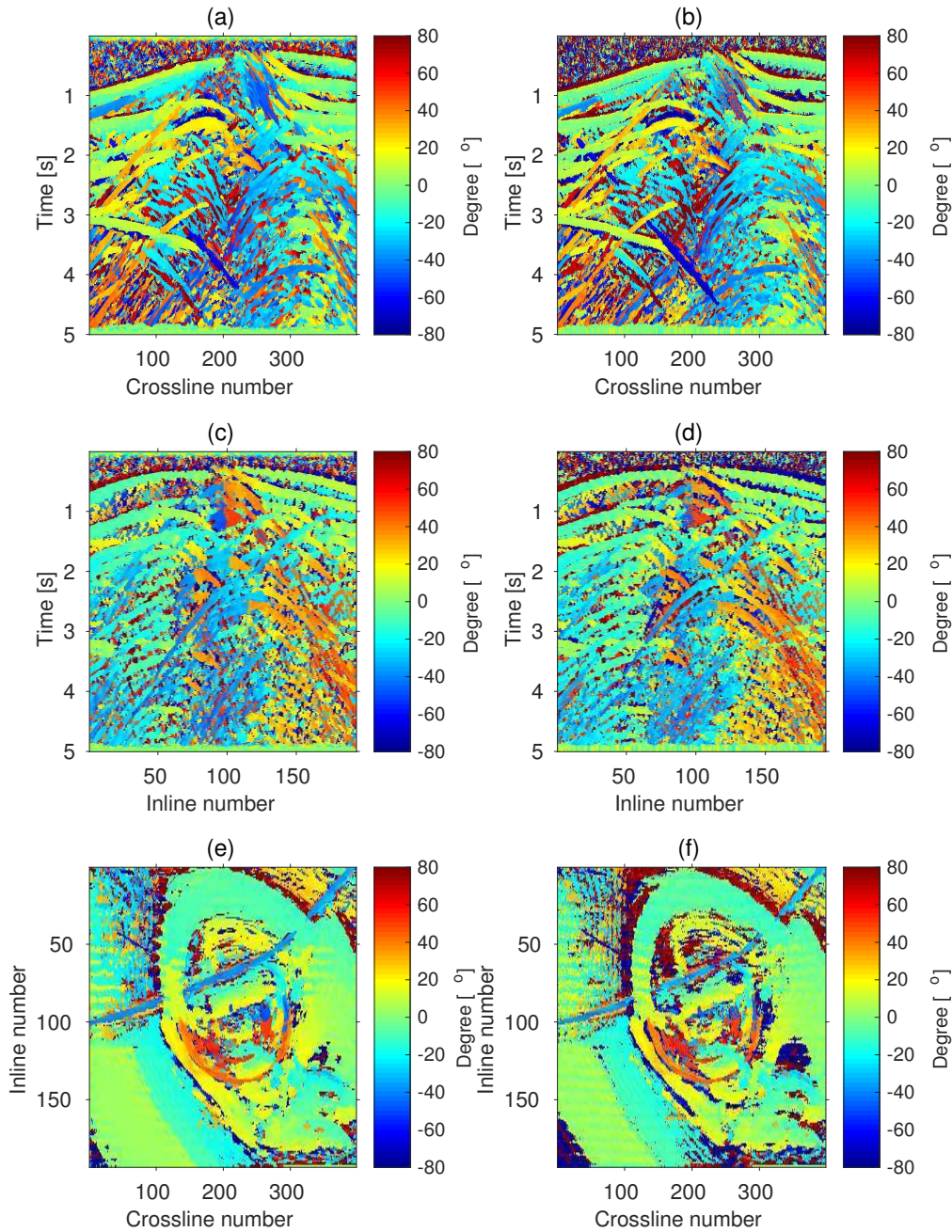


Figure D.5.: Dip wavefront attribute. (a) Inline 190 with pragmatic approach. (b) Inline 190 with DE. (c) Crossline 300 with pragmatic approach. (d) Crossline 300 with DE. (e) Time slice 1.2 s with pragmatic approach. (f) Time slice 1.2 s with DE. In this test, I constrain the dip search range between $[-80^\circ$ to $80^\circ]$.

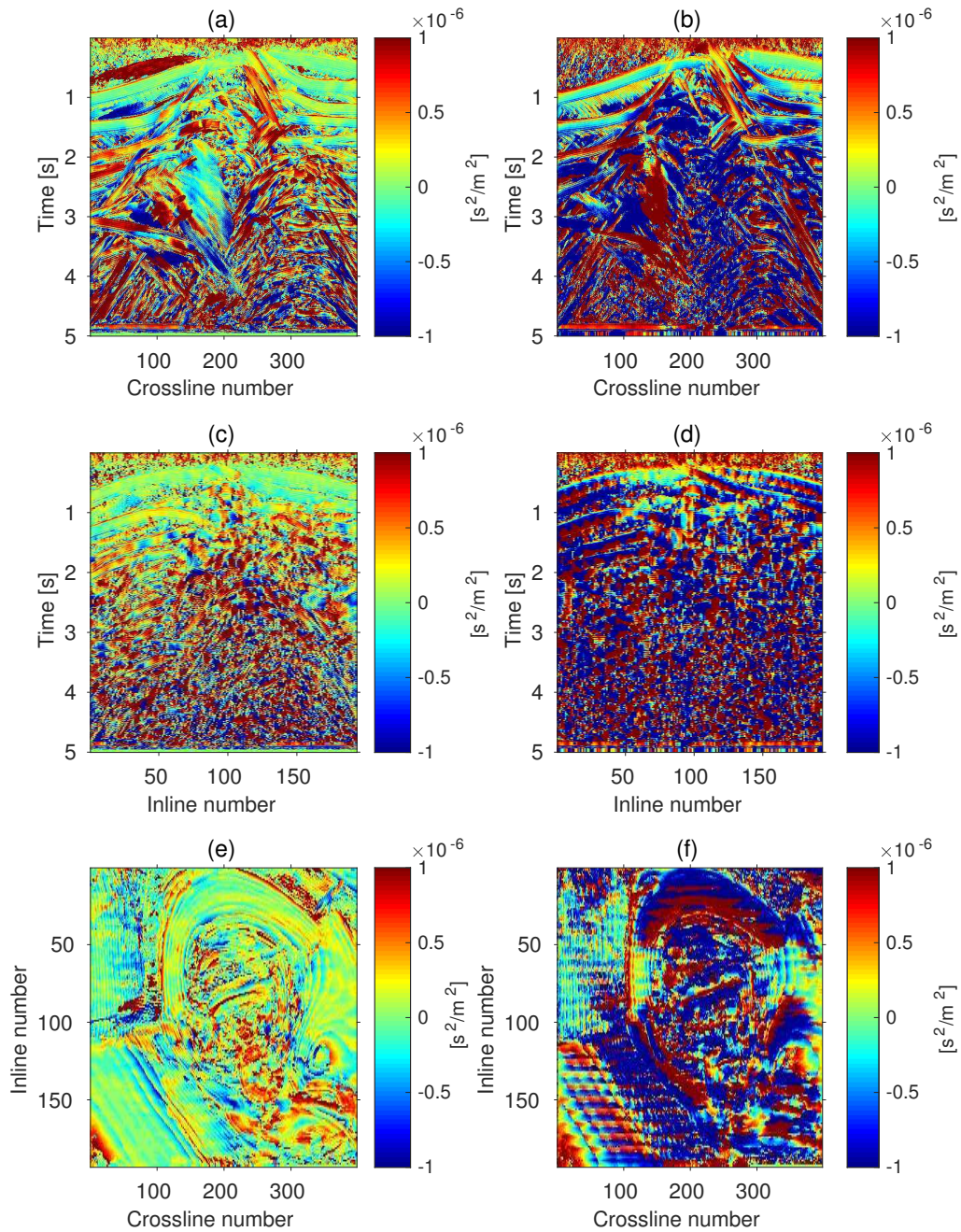


Figure D.6.: N_{00} wavefront attribute. (a) Inline 190 with pragmatic approach. (b) Inline 190 with DE. (c) Crossline 300 with pragmatic approach. (d) Crossline 300 with DE. (e) Time slice 1.2 s with pragmatic approach. (f) Time slice 1.2 s with DE.

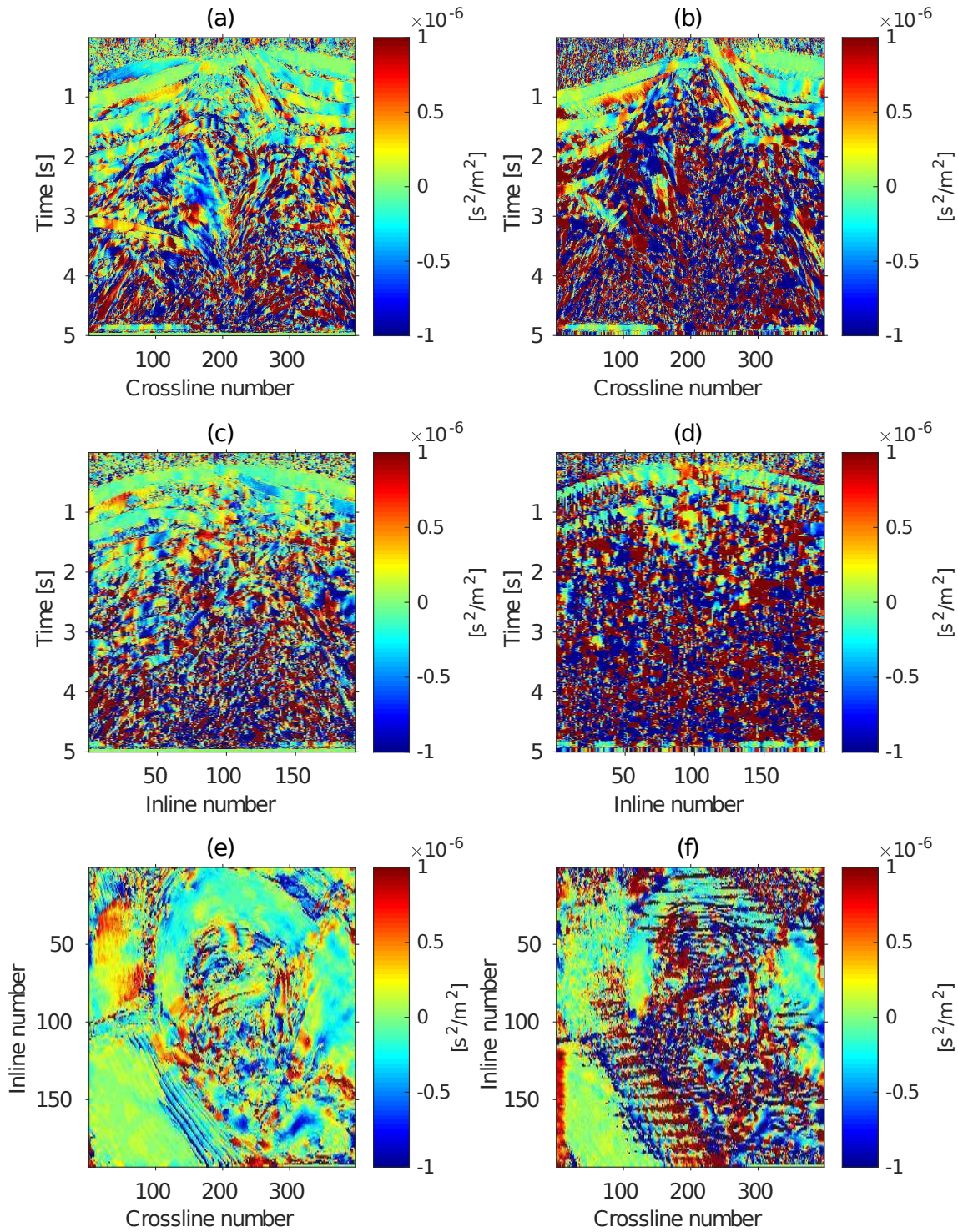


Figure D.7.: N_{10} wavefront attribute. (a) Inline 190 with pragmatic approach. (b) Inline 190 with DE. (c) Crossline 300 with pragmatic approach. (d) Crossline 300 with DE. (e) Time slice 1.2 s with pragmatic approach. (f) Time slice 1.2 s with DE.

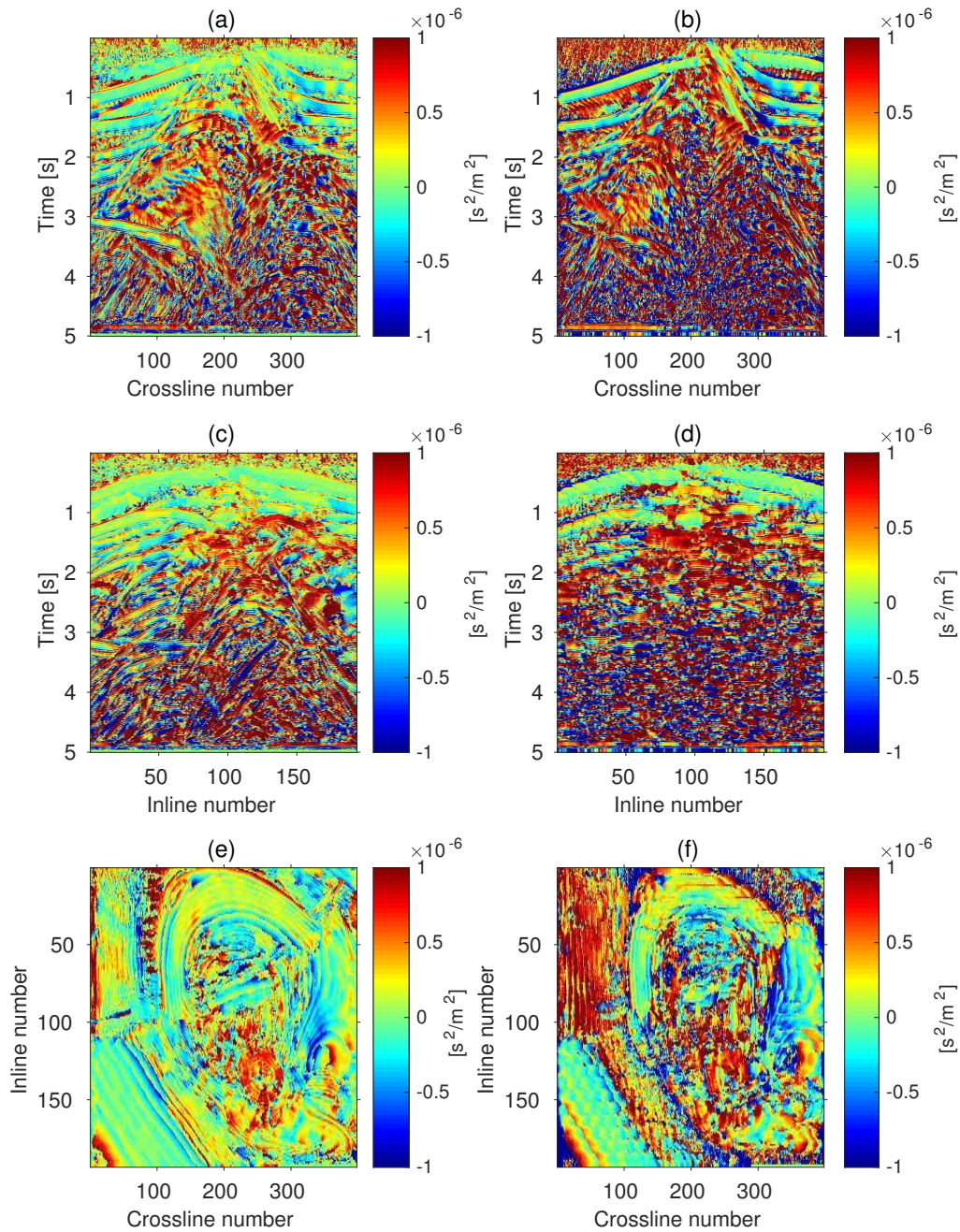


Figure D.8.: N_{11} wavefront attribute. (a) Inline 190 with pragmatic approach. (b) Inline 190 with DE. (c) Crossline 300 with pragmatic approach. (d) Crossline 300 with DE. (e) Time slice 1.2 s with pragmatic approach. (f) Time slice 1.2 s with DE.

Appendix E.

Software developed in this work

I used a Unix operating system (Debian OS) with the typesetting software \LaTeX to write the thesis. The software listed below was executed on the Thunder8 operated by the Central IT Services (CIS). Examples shown in the thesis were drawn and visualized by Inkscape, Matlab, and Seismic Unix package made available by the Center for Wave Phenomena (CWP) at the Colorado School of Mines. For this work, five software packages are developed:

1: 3-D CRS with global optimization. It is a global search software written in OpenMPI/C++ by Yujiang Xie in order to simultaneously determine the 3-D CRS wavefront attributes, where several optimization algorithms are introduced. Examples are the particle swarm optimization (PSO) ([Kennedy and Eberhart, 1995](#); [Shi and Eberhart, 1998](#)), genetic algorithm (GA) ([Holland, 1975](#)), differential evolution (DE) ([Storn and Price, 1997](#)), simulated annealing (SA) (see e.g., [Kirkpatrick et al., 1983](#)), Nelder-Mead (NA) method ([Nelder and Mead, 1965](#)), as well as the Powell conjugate direction (PCD) algorithm ([Powell, 1964](#)). In this software, the 3-D non-hyperbolic CRS ([Fomel and Kazinnik, 2013](#)) is also taken into account (results are not shown in this work). The C++ source files to read and write SU files are originally written by German Höcht and Alexander Müller. The raw version of the software can be downloaded from the WIT website, and an updated version can be gotten from the WIKI pages, applied seismics, Hamburg.

2: 3-D kinematic and dynamic ray tracing. I developed this software written in OpenMPI/C++ in order to compute the traveltimes, slowness vector, and the ray propagator matrix of a ray from a given smooth velocity model. The slowness vector and the ray propagator matrix are related to the 3-D CRS wavefront attributes (see [Appendix C and D](#)). In this software, only the isotropic case is implemented and the reduced Hamiltonian is considered, e.g., without turning points. This software is an extension of Duvencek's NIP-wave tomography package ([Duvencek, 2004](#)). Results with the 3-D kinematic and dynamic ray tracing to compute the 3-D CRS wavefront attributes from a given smooth velocity model will be investigated later.

3: 5-D interpolation with wavefront attributes. It is a 5-D seismic interpolation software written in OpenMPI/C++ by Yujiang Xie based on the 3-D wavefront attributes determined above. To regularize the seismic traces in each 3-D CMP gather, I use an azimuth-based regularization strategy, e.g., all traces are situated along different azimuth directions with increasing offsets. This software has two packages, the first package called *3D partial CRS stack* is an extension of Baykulov's partial CRS package (Baykulov and Gajewski, 2009, 2010), where different azimuthal directions are considered. The second package is called *3-D finite-offset CRS stack* (not showing in this work).

4: Rank-reduction-based 5-D interpolation. This software is an extension of the open-source Matlab code package (Chen et al., 2016a). The current version is very computational expensive since it involves several very larger matrices (more than 30 GB while dealing with a 3 GB data) in the Matlab environment.

5: 3-D CRS with pragmatic approach, which is originally written by Müller (2003), where I developed the matrix \mathbf{N} search step since the old 3-D CRS version downloaded from the WIT website seems missing the \mathbf{N} search step.

Appendix F.

Publications

Publications derived from the dissertation.

Journal papers:

Y. Xie & D. Gajewski, 2017. 3-D wavefront attributes and conflicting dips, *Geophysics*, submitted.

Y. Xie & D. Gajewski, 2017. 5-D interpolation with wavefront attributes, *Geophysical Journal International*, 211, 897-919.

Conference abstracts:

Y. Xie, 2017. 3D Prestack Data Enhancement with a Simplified CO CRS Operator, *79th EAGE Conference and Exhibition 2017*.

Y. Xie & D. Gajewski, 2016. Interpolation and regularization with the 3D CRS operator, *SEG Technical Program Expanded Abstracts 2016*.

Y. Xie & D. Gajewski, 2016. Simultaneous estimation of the 3D CRS attributes by an evolutionary-based Nelder Mead algorithm, *SEG Technical Program Expanded Abstracts 2016*.

Y. Xie & D. Gajewski, 2016. Automatic Estimation of the 3D CRS Attributes by a Metaheuristic-based Optimization, *78th EAGE Conference and Exhibition 2016*.

Appendix G.

Acknowledgments

In my years of study in Germany, there are a lot of people I want to thank. Without their companionship and help, I can not finish my doctoral research. First of all, I would like to thank my supervisor **Prof. Dr. Dirk Gajewski**. With his supervision, I grew up and went through a lot, such as taking part in the weekly group seminars, joining and enjoying the annual WIT meeting, as well as participating in annual SEG/EAGE conferences. Importantly, through his influence, I have the idea of opening up my personal research fields.

This work could not be completed without many great people help. I am deeply grateful to:

- **Claudia Vanelle** who helped me to improve my presentation style in particular in motivation, figures, and font size as well as to guide me in the right direction, such as focusing on the physical meaning of my work, not just only the computer science. She also helped me to draw the CRS figures for my SEG presentation 2016. Importantly, she always gives some constructive and valuable suggestions during each possible presentation in our group which helps me a lot.
- **Ekkehart Teßmer** who helped me with technical support as well as given me valuable comments during my presentation.
- **Ransheng Chen** for detailed discussions of the genetic algorithm (GA) and the differential evolution (DE) algorithm in actual implementation.
- **Jan Walda** for constructive discussions of several global optimization algorithms and the conflicting dip problem of the CRS method.
- **Yan Yang** for interesting discussions of the big differences between the 3-D CSP and the 3-D partial CRS, which helps me a lot.

- **Parsa Bakhtiari Rad** shared me his experience of determining the 3-D CRS wavefront attributes with the pragmatic approach.
- **Ivan Abakumov** for initially suggested the 3-D SEG data, and provide his Matlab scripts, e.g., for the 3D SEG data preprocessing and visualization.
- **Lei Li** for many interesting discussions of the finite-difference (FD) modeling, such as how to choose different modeling parameters.
- **Sergius Dell, Benjamin Schwarz, Khawar Ashfaq Ahmed, Manizheh Vefagh** shared their very important presentations in our group, which involves constructive and helpful discussions related to diffraction imaging, passive seismics, 3-D CRS application as well as the multiple attenuation. I also appreciate **Alexander Bauer, Martina Glöckner** for continuous discussions of diffraction tomography and time-migration velocity estimation.

Besides, I would like to thank:

- **My family** for all the support during my studies.
- **Society of Exploration Geophysicists (SEG)** for providing the salt velocity model and the data.
- **China Scholarship Council (CSC)** for partial funding of my Ph.D. studies.

Bibliography

- Abakumov, I. (2017). *Systematic analysis of double-square-root-based stacking operators*. PhD thesis, University of Hamburg, Germany.
- Ahmed, K., Schwarz, B., and Gajewski, D. (2015). Application of the 3D common-reflection-surface stack workflow in a crystalline rock environment. *Geophysical Prospecting*, 63:990–998.
- Aminzadeh, F., Brac, J., and Kunz, T. (1997). 3D Salt and Overthrust models. In *SEG/EAGE Modeling Series, No. 1: Distribution CD of Salt and Overthrust models, SEG Book Series Tulsa, Oklahoma*.
- Barros, T., Ferrari, R., Krummenauer, R., and Lopes, R. (2015). Differential evolution-based optimization procedure for automatic estimation of the common-reflection surface traveltimes parameters. *Geophysics*, 80:WD189–WD200.
- Bauer, A., Schwarz, B., and Gajewski, D. (2016). Improving the resolution of wavefront tomography by utilizing diffractions. In *SEG Technical Program Expanded Abstracts 2016*.
- Baykulov, M. and Gajewski, D. (2009). Prestack seismic data enhancement with partial common-reflection-surface (CRS) stack. *Geophysics*, 74:V49–V58.
- Baykulov, M. and Gajewski, D. (2010). Partial 3D CRS Stack. In *72nd EAGE Conference and Exhibition incorporating SPE EUROPEC 2010*.
- Bergler, S. (2004). *On The Determination and Use of Kinematic Wavefield Attributes for 3D Seismic Imaging*. PhD thesis, Logos Verlag, Berlin.
- Bonomi, E., Cristini, A., Theis, D., and Marchetti, P. (2009). 3D CRS analysis: a data-driven optimization for the simultaneous estimate of the eight parameters. In *SEG Technical Program Expanded Abstracts*.
- Bortfeld, R. (1989). Geometrical ray theory: rays and traveltimes in seismic systems (second-order approximation of the traveltimes). *Geophysics*, 54:342–349.
- Buchdahl, H. (1970). An Introduction to Hamiltonian Optics. In *Cambridge Univ. Press*.

- Cardone, G., Christini, A., Bonomi, E., Marchetti, P., Zambonini, R., Hubral, P., and Mann, J. (2003). 3D Zero-Offset CRS Stack for Narrow-Azimuth Data - Formulation and Examples. In *EAGE SEG Summer Research Workshop*.
- Chen, Y., Huang, W., Zhang, D., and Chen, W. (2016a). An open-source matlab code package for improved rank-reduction 3D seismic data denoising and reconstruction. *Comput. Geosci.*, 95:59–66.
- Chen, Y., Zhang, D., Jin, Z., Chen, X., Zu, S., Huang, W., and Gan, S. (2016b). Simultaneous denoising and reconstruction of 5-D seismic data via damped rank-reduction method. *Geophys. J. Int.*, 206:1695–1717.
- Chopra, S. and Marfurt, K. (2013). Preconditioning seismic data with 5D interpolation for computing geometric attributes. *The Leading Edge*, 32:1456–1460.
- Coimbra, T., Faccipieri, J., Rueda, D., and Tygel, M. (2016). Common-reflection-point time migration. *Studia Geophysica et Geodaetica*, 60:500–530.
- Corana, A., Marchesi, M., Martini, C., and Ridela, S. (1987). Minimizing multimodal functions of continuous variables with "simulated annealing" algorithm. *ACM Transactions on Mathematical Software*, 13:262–280.
- Curry, W. (2010). Interpolation with Fourier-radial adaptive thresholding. *Geophysics*, 75:WB95–WB102.
- Dell, S. and Gajewski, D. (2011a). 3D CRS-attributes Based Diffraction Imaging. In *73rd EAGE Conference and Exhibition incorporating SPE EUROPEC 2011*.
- Dell, S. and Gajewski, D. (2011b). Common-reflection-surface-based workflow for diffraction imaging. *Geophysics*, 76:S187–S195.
- Duveneck, E. (2004). Velocity model estimation with data-derived wavefront attributes. *Geophysics*, 69:265–274.
- Ely, G., Aeron, S., Hao, N., and Kilmer, M. (2015). 5D seismic data completion and denoising using a novel class of tensor decompositions. *Geophysics*, 80:V83–V95.
- Fomel, S. (2003). Seismic reflection data interpolation with differential offset and shot continuation. *Geophysics*, 68:733–744.
- Fomel, S. and Kazinnik, R. (2013). Non-hyperbolic common reflection surface. *Geophysics*, 61:21–27.
- Gajewski, D. and Pšenčík, I. (1987). Computation of high-frequency seismic wavefields in 3-D laterally inhomogeneous anisotropic media. *Geophys. J. Int.*, 91:383–411.

- Gajewski, D. and Pšenčík, I. (1990). Vertical seismic profile synthetics by dynamic ray tracing in laterally varying layered anisotropic structures. *J. Geophys. Res.*, 95:11301–11315.
- Gao, J., Stanton, A., and Sacchi, M. (2015). Parallel matrix factorization algorithm and its application to 5D seismic reconstruction and denoising. *Geophysics*, 80:V173–V187.
- Garabito, G., Stoffa, P., Lucena, L., and Cruz, J. (2012). Part I – CRS stack: Global optimization of the 2D CRS-attributes. *J.appl.Geophys*, 85:92–101.
- Gelchinsky, B., Berkovitch, A., and Keydar, S. (1999). Multifocusing homeomorphic imaging: Part 1. Basic concepts and formulas. *Journal of Applied Geophysics*, 42:229–242.
- Gelius, L. and Tygel, M. (2015). Migration-velocity building in time and depth from 3D (2D) Common-Reflection-Surface (CRS) stacking - theoretical framework. *Studia Geophysica et Geodaetica*, 59:253–282.
- Höcht, G. (2002). *Traveltime approximations for 2D and 3D media and kinematic wavefield attributes*. PhD thesis, University of Karlsruhe, Germany.
- Höcht, G., Ricarte, P., Bergler, S., and Landa, E. (2009). Operator oriented CRS interpolation. *Geophysical Prospecting*, 57:957–979.
- Holland, J. (1975). Adaptation in natural and artificial systems. In *University of Michigan Press, Ann Arbor*.
- Huang, W., Wang, R., Zhang, M., Chen, Y., and Yu, J. (2015). Random noise attenuation for 3D seismic data by modified multichannel singular spectrum analysis. In *77th Annual International Conference and Exhibition, EAGE Extended Abstracts*.
- Hubral, P., Schleicher, J., and Tygel, M. (1992). Three-dimensional paraxial ray properties. Part I. Basic relations. *J.seism.Explor.*, 1:265–279 [Part II. Applications, 347–362].
- Hubral, P., Schleicher, J., and Tygel, M. (1993a). Determination of Fresnel zones from traveltime measurements. *Geophysics*, 58:703–712.
- Hubral, P., Schleicher, J., and Tygel, M. (1993b). Three-dimensional primary zero offset reflections. *Geophysics*, 58:692–702.
- Ingber, L. (1989). Very fast simulated re-annealing. *Mathematical and Computer Modelling*, 12:967–973.
- Jäger, R. (1999). *The Common Reflection Surface Stack-Introduction and Application*. PhD thesis, Diploma thesis, Karlsruhe University, Germany.

- Jäger, R., Mann, J., Höcht, G., and Hubral, P. (2001). Common-reflection-surface stack: Image and attributes. *Geophysics*, 66:97–109.
- Kabir, M. and Verschuur, D. (1995). Restoration of missing offsets by parabolic Radon transform. *Geophysical Prospecting*, 43:347–368.
- Kaplan, S., Naghizadeh, M., and Sacchi, M. (2010). Data reconstruction with shot-prole least-squares migration. *Geophysics*, 75:WB121–WB136.
- Kennedy, J. and Eberhart, R. (1995). Particle Swarm Optimization. In *Proceedings of IEEE International Conference on Neural Networks*, pages 1942–1948.
- Kirkpatrick, S., Gelatt, C., and Vecchi, M. (1983). Optimization by simulated annealing. *Science*, 220:671–680.
- Kreimer, N., Stanton, A., and Sacchi, M. (2013). Tensor completion based on nuclear norm minimization for 5D seismic data reconstruction. *Geophysics*, 78:V273–V284.
- Liu, B. and Sacchi, M. (2004). Minimum weighted norm interpolation of seismic records. *Geophysics*, 69:1560–1568.
- Liu, Y. and Fomel, S. (2011). Seismic data interpolation beyond aliasing using regularized nonstationary autoregression. *Geophysics*, 76:V69–V77.
- Mandal, B., Sen, M., Vaidya, V., and Mann, J. (2013). Deep seismic image enhancement with the common reflection surface (CRS) stack method: evidence from the Aravalli-Delhi fold belt of northwestern India. *Geophys. J. Int.*, 196:902–917.
- Mann, J. (2002). *Extensions and Applications of the Common-Reflection-Surface Stack Method*. PhD thesis, University of Karlsruhe, Germany.
- Mann, J., Jager, R., Muller, T., Hocht, G., and Hubral, P. (1999). Common-reflection-surface stack - a real data example. *J. Appl. Geoph.*, 42:301–318.
- Menyoli, E., Gajewski, D., and Hübscher, C. (2004). Imaging of complex basin structures with the common reflection surface (CRS) stack method. *Geophys. J. Int.*, 157:1206–1216.
- Moser, T. and Červený, V. (2007). Paraxial ray methods for anisotropic inhomogeneous media. *Geophys. Prospect.*, 55:21–37.
- Müller, N. (2003). The 3D Common-Reflection-Surface Stack - Theory and Application. In *Diploma thesis, University of Karlsruhe*.
- Müller, N. (2007). *Determination of interval velocities by inversion of kinematic 3D wavefield attributes*. PhD thesis, University of Karlsruhe.

- Naghizadeh, M. and Innanen, K. (2011). Seismic data interpolation using a fast generalized Fourier transform. *Geophysics*, 76:V1–V10.
- Naghizadeh, M. and Sacchi, M. (2009). f-x adaptive seismic-trace interpolation. *Geophysics*, 74:V9–V16.
- Naghizadeh, M. and Sacchi, M. (2010). Beyond alias hierarchical scale curvelet interpolation of regularly and irregularly sampled seismic data. *Geophysics*, 75:WB189–WB202.
- Neidell, N. and Taner, M. (1971). Semblance and other coherency measures for multichannel data. *Geophysics*, 36:482–497.
- Nelder, J. and Mead, R. (1965). A simplex method for function minimization. *The Computer Journal*, 7:308–313.
- Oropeza, V. E. and Sacchi, M. (2011). Simultaneous seismic data de-noising and reconstruction via multichannel singular spectrum analysis. *Geophysics*, 76:V25–V32.
- Pedersen, M. (2010). Good Parameters for Differential Evolution. In *Hvass Laboratories Technical Report HL1002*.
- Powell, M. (1964). An efficient method for finding the minimum of a function of several variables without calculating derivatives. *The Computer Journal*, 7:155–162.
- Rad, P., Vanelle, C., and Gajewski, D. (2015). 3D CRS-based Prestack Diffraction Separation and Imaging. In *77th EAGE Conference and Exhibition*.
- Ronen, J. (1987). Wave-equation trace interpolation. *Geophysics*, 52:973–984.
- Schleicher, J., Tygel, M., and Hubral, P. (1993a). 3D true-amplitude finite offset migration. *Geophysics*, 58:1112–1126.
- Schleicher, J., Tygel, M., and Hubral, P. (1993b). Parabolic and hyperbolic paraxial two-point traveltimes in 3D media. *Geophysical Prospecting*, 41:495–513.
- Schwarz, B., Bauer, A., and Gajewski, D. (2016). Passive seismic source localization via common-reflection-surface attributes. *Studia Geophysica et Geodaetica*, 60:531–546.
- Schwarz, B. and Gajewski, D. (2017). Accessing the diffracted wavefield by coherent subtraction. *Geophys. J. Int.*, page doi.org/10.1093/gji/ggx291.
- Schwarz, B., V. C. G. D. and Kashtan, B. (2014). Curvatures and inhomogeneities: An improved common-reflection approach. *Geophysics*, 79:S231–S240.

- Shi, Y. and Eberhart, R. (1998). A modified particle swarm optimizer. In *Proceedings of IEEE International Conference on Evolutionary Computation*, pages 69–73.
- Shuey, R. (1985). A simplification of the Zoeppritz equations. *Geophysics*, 50:609–614.
- Spitz, S. (1991). Seismic trace interpolation in the f-x domain. *Geophysics*, 56:785–794.
- Stolt, R. (2002). Seismic data mapping and reconstruction. *Geophysics*, 67:973–984.
- Storn, R. and Price, K. (1997). Differential evolution - a simple and efficient heuristic for global optimization over continuous spaces. *Journal of Global Optimization*, 11:341–359.
- Trad, D. (2009). Five-dimensional interpolation: Recovering from acquisition constraints. *Geophysics*, 74:V123–V132.
- Trad, D. (2014). Five-dimensional interpolation: New directions and challenges. In *CSEG Recorder*, pages 40–46.
- Trad, D., Ulrych, T., and Sacchi, M. (2002). Accurate interpolation with high-resolution time-variant Radon transforms. *Geophysics*, 67:644–656.
- Trickett, S. (2008). F-xy cadzow noise suppression. In *CSPG CSEG CWLS Convention*, pages 303–306.
- Trickett, S., Burroughs, L., Milton, A., Walton, L., and Dack, R. (2010). Rank-reduction-based trace interpolation. In *SEG Technical Program Expanded Abstracts*, volume 29, pages 3829–3833.
- Ursin, B. (1982). Quadratic wavefront and traveltime approximations in inhomogeneous layered media with curved interfaces. *Geophysics*, 47:1012–1021.
- Červený, V. (1972). Seismic rays and ray intensities in inhomogeneous anisotropic media. *Geophys. J.R. astr. Soc.*, 29:1–13.
- Červený, V. (2001). Seismic Ray Theory. In *Cambridge University Press, Cambridge*.
- Červený, V., Iversen, E., and Pšenčík, I. (2012). Two-point paraxial traveltimes in an inhomogeneous anisotropic medium. *Geophys. J. Int.*, 189:1597–1610.
- Červený, V. and Moser, T. (2007). Ray propagator matrices in three-dimensional anisotropic inhomogeneous layered media. *Geophys. J. Int.*, 168:593–604.
- Walda, J. and Gajewski, D. (2017). Determination of wavefront attributes by differential evolution in the presence of conflicting dips. *Geophysics*, 82:V229–V239.

- Xie, Y. (2017). 3D Prestack Data Enhancement with a Simplified CO CRS Operator. In *79th Annual International Conference and Exhibition*.
- Xie, Y. and Gajewski, D. (2016a). Automatic Estimation of the 3D CRS Attributes by a Metaheuristic-based Optimization. In *78th Annual International Conference and Exhibition, EAGE Extended Abstracts*.
- Xie, Y. and Gajewski, D. (2016b). Interpolation and regularization with the 3D CRS operator. In *SEG Technical Program Expanded Abstracts 2016*, pages 4092–4096.
- Xie, Y. and Gajewski, D. (2016c). Simultaneous estimation of the 3D CRS attributes by an evolutionary-based Nelder-Mead algorithm. In *SEG Technical Program Expanded Abstracts 2016*, pages 4326–4330.
- Xie, Y. and Gajewski, D. (2017). Five-dimensional interpolation with wavefront attributes. *Geophys. J. Int.*, 211:897–919.
- Xu, S., Lambare, G., and Calandra, H. (2004). Fast migration/inversion with multivalued ray fields: Part 2 - Applications to the 3D SEG/EAGE salt model. *Geophysics*, 69:1320–1328.
- Zhang, Y. and Lu, W. (2014). 2D and 3D prestack seismic data regularization using an accelerated sparse time-invariant Radon transform. *Geophysics*, 79:V165–V177.
- Zwartjes, P. and Sacchi, M. (2007). Fourier reconstruction of nonuniformly sampled, aliased seismic data. *Geophysics*, 72:V21–V32.

Eidesstattliche Versicherung

Hiermit erkläre ich an Eides statt, dass ich die vorliegende Dissertationsschrift selbst verfasst und keine anderen als die angegebenen Quellen und Hilfsmittel benutzt habe.

Hamburg, den

Unterschrift